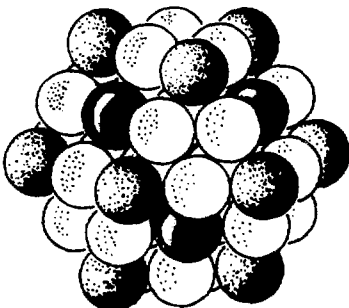
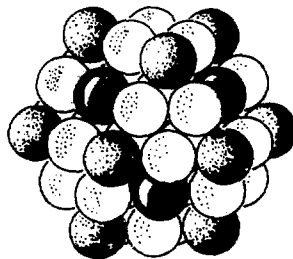
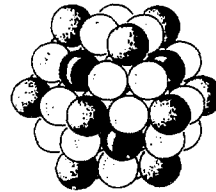


*Ne 88c 1000*

INIS-mf--11388

# Mössbauer Studies of Non-linear Excitations and Gold Cluster Compounds



**H.H.A. Smit**

# **Mössbauer Studies of Non-linear Excitations and Gold Cluster Compounds**

**An Experimental Investigation of Non-linear Excitations in  
Ising-like Antiferromagnetic Chain Systems and of  
Metal Core Atoms in Polynuclear Gold Cluster Compounds**

**Cover Design: ASF**

# **Mössbauer Studies of Non-linear Excitations and Gold Cluster Compounds**

**An Experimental Investigation of Non-linear Excitations in  
Ising-like Antiferromagnetic Chain Systems and of  
Metal Core Atoms in Polynuclear Gold Cluster Compounds**

**Proefschrift**

ter verkrijging van de graad van Doctor  
aan de Rijksuniversiteit te Leiden,  
op gezag van de Rector Magnificus  
Dr. J.J.M. Beenakker,  
hoogleraar in de faculteit  
der Wiskunde en Natuurwetenschappen,  
volgens besluit van het College van Dekanen  
te verdedigen op woensdag 15 juni 1988  
te klokke 14.15 uur

door

**Hubert Herman Antonius Smit**

geboren te Wassenaar in 1960

## **Promotiecommissie**

Promotor: Prof. Dr. L.J. de Jongh  
Co-promotor: Dr. R.C. Thiel  
Referent: Dr. Ir. A.M. van der Kraan (T.U. Delft)  
Overige leden: Prof. Dr. W.J. Huiskamp  
Prof. Dr. G. Schmid (Universität Essen)  
Prof. Dr. G. Frossati

Het in dit proefschrift beschreven onderzoek werd uitgevoerd als onderdeel van het onderzoeksprogramma van de Stichting voor Fundamenteel Onderzoek der Materie (FOM) en is mogelijk gemaakt door financiële steun van de Nederlandse Organisatie voor Zuiver-Wetenschappelijk Onderzoek (ZWO).

Aan mijn ouders.  
Aan Annet en  
Josijn.

# Contents

<b>1</b>	<b>Introduction</b>	<b>9</b>
1.1	Mössbauer Effect Spectroscopy . . . . .	9
1.2	Non-linear Excitations in Magnetic Systems . . . . .	10
1.3	Gold Cluster Compounds as Model Systems for Small Metal Particles	11
<b>2</b>	<b>Mössbauer Effect Spectroscopy</b>	<b>15</b>
2.1	Introduction . . . . .	15
2.2	Mössbauer Effect Spectroscopy . . . . .	15
2.3	Nuclear Level Splitting . . . . .	16
2.3.1	Isomer Shift . . . . .	18
2.3.2	Magnetic Hyperfine Interaction . . . . .	20
2.3.3	Quadrupole Splitting . . . . .	22
2.3.4	Combined Quadrupole and Magnetic Hyperfine Interactions .	26
2.4	Relative Intensities . . . . .	27
2.5	Debye-Waller Factor . . . . .	29
2.6	Spectral Line Shape . . . . .	31
2.6.1	Static Hyperfine Parameters . . . . .	31
2.6.2	Fluctuating Hyperfine Field . . . . .	34
<b>3</b>	<b>Experimental Arrangements</b>	<b>39</b>
3.1	Introduction . . . . .	39
3.2	Cryostat . . . . .	39
3.3	Mössbauer Spectrometer . . . . .	47
3.4	Source and Absorber Preparation . . . . .	49
3.5	Absolute Debye-Waller Factor Determination . . . . .	51
<b>4</b>	<b>Non-linear Excitations in Ising-like Quasi One-dimensional Magnetic Systems</b>	<b>53</b>
4.1	Introduction . . . . .	53
4.2	Properties of the Investigated Compounds . . . . .	55
4.3	Mössbauer Spectra and Analyses . . . . .	58
4.3.1	Excess Linewidth . . . . .	58
4.3.2	Powder Data and the Blume and Tjon Model . . . . .	60
4.3.3	Single Crystal Results in an Applied Field . . . . .	64
4.4	Ideal Kink Gas . . . . .	66
4.5	Phenomenological Model . . . . .	69
4.6	Discussion . . . . .	72
4.7	Conclusion . . . . .	73

<b>5 Mössbauer and Specific Heat Studies of the Vibrations of Metal Core atoms in Polynuclear Gold Cluster Compounds</b>	<b>77</b>
5.1 Introduction . . . . .	77
5.2 Cluster Vibrations . . . . .	78
5.3 Metal Cluster Compounds . . . . .	81
5.4 Mössbauer Results . . . . .	82
5.5 Isomer Shift and Quadrupole Splitting . . . . .	85
5.6 Debye-Waller Factors . . . . .	90
5.7 Specific Heat . . . . .	92
5.8 Discussion . . . . .	96
5.9 Conclusion . . . . .	100
<b>Samenvatting</b>	<b>105</b>
<b>Curriculum Vitae</b>	<b>109</b>
<b>Published Work</b>	<b>110</b>
<b>Nawoord</b>	<b>111</b>



# 1 Introduction

## 1.1 Mössbauer Effect Spectroscopy

This thesis describes an experimental study of two selected problems in solid state physics in which Mössbauer effect spectroscopy (M.E.S.) is employed. M.E.S., discovered by R. Mössbauer in 1958 [1], is an experimental technique based on the resonant absorption of  $\gamma$ -rays, originating from the radioactive decay of unstable nuclei. Resonant absorption occurs if the  $\gamma$ -rays are emitted and absorbed without loss of energy due to e.g. the creation of a phonon. If source and absorber are made out of the same material, the emission line of the source and the absorption line of the absorber fully overlap. In general, however, the hyperfine interactions between the nucleus and its surroundings are dissimilar in source and absorber. In the transmission experiment that is employed in the present investigation, a standard source is used and the energy of its  $\gamma$ -rays is modulated by means of the Doppler effect. The resulting Mössbauer spectrum displays the resonant absorption as a function of energy.

The Mössbauer isotope at inequivalent sites will experience different hyperfine interactions, resulting in different hyperfine splittings in the Mössbauer spectrum. Usually the hyperfine interaction is described as a multipole expansion, of which the first three terms are of interest. These are the isomer shift (I.S.), which is a measure for the electron density at the nucleus, the magnetic hyperfine field ( $H_{hf}$ ), and the quadrupole splitting (Q.S.), resulting from the electric field gradient at the nucleus. These quantities are determined by the chemical environment of the Mössbauer isotope. Therefore, M.E.S. is an accurate microscopic probe which is of interest to both chemists and physicists.

In the work described in this thesis, we have used the Mössbauer effect to explore two physical problems which are of great current interest. The first concerns the dynamics of the electronic spins in magnetic chain systems. In particular the influence of non-linear (solitonic) excitations is investigated. The electronic spins on the chains exert a magnetic hyperfine field on the nucleus. Therefore, the dynamic behaviour of the spins on the chains causes fluctuations in the hyperfine field. More accurately, from the Mössbauer spectrum quantitative information on the autocorrelation function,  $\langle S^*(t)S^*(0) \rangle$ , can be obtained. In this way, M.E.S. provides information from which interesting conclusions about the non-linear excitations can be drawn. The second physical problem addressed to in this thesis concerns the thermal vibrations of the metal core atoms in gold cluster compounds. Since the gold atoms in the metal core are bonded to different ligands and/or a different number of gold neighbours, they are characterized by different M.E.S. parameters (i.e. I.S. and Q.S.). Inequivalent gold sites give therefore rise to distinguishable subspectra. The Mössbauer fraction, i.e. the fraction of  $\gamma$ -ray absorptions which occurs recoil-free, can be directly related to the area of these subspectra, and is determined by the bonding strength of the individual sites. In this way, M.E.S. is a unique microscopic technique which reveals information on the local vibrational

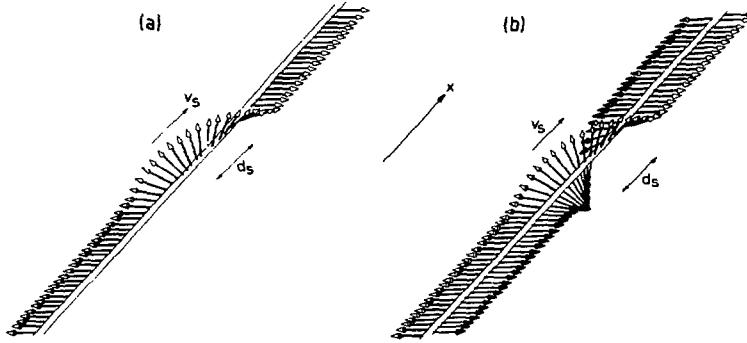


Figure 1.1: Illustration of a  $\pi$ -soliton in a ferro- and an antiferromagnet.

density of states, of the metal cores, which can be viewed as a collection of ultra small identical metal particles embedded in a dielectric solid.

In section 1.2 and 1.3 we will present a brief introduction to these two topics. The thesis is further arranged as follows. In chapter 2, the quantities of the Mössbauer theory will be reviewed which are relevant for the present thesis. Chapter 3 describes the experimental arrangements that have been made to perform the necessary Mössbauer measurements. Non-linear excitations in antiferromagnetic chain systems is the subject that will be dealt with in chapter 4. The  $^{197}\text{Au}$  measurements on the polynuclear gold compounds can be found in chapter 5.

## 1.2 Non-linear Excitations in Magnetic Systems

About twenty years ago, solutions of non-linear differential equations were applied for the first time in describing experimental observations [2]. In the seventies, non-linear physics became of interest for solid state physicists [3,4]. The subject has experienced an exponential growth during the last decade, because of its wide applicability to a variety of different physical systems. Quite interestingly, one-dimensional magnetism appeared to provide a number of archetypical model systems for investigating these non-linear excitations [5]. In anisotropic or Ising-like chain systems, linear physics involving magnons or spin waves appears to be insufficient to describe their physical quantities, and non-linear physics becomes of dominant importance for the interpretation. Non-linear excitations are solutions of non-linear differential equations (e.g. the sine-Gordon equation), and are commonly referred to as solitons. They are local excitations that connect degenerate ground states. In a ferromagnet a  $\pi$ -soliton separates a spin up and a spin down region, as depicted in fig. 1.1a. In fig. 1.1b its counterpart for an antiferromagnetic chain system is shown. These excitations can be seen as relativistic quasi particles with a mass, a (rest) energy, and a velocity which depends on the initial conditions. Since the soliton energy is translational invariant, its velocity is preserved during the propagation. In the ideal gas approximation, the solitons suffer only a phase shift

when colliding with each other or with an impurity [6]. Indeed the first neutron diffraction and N.M.R. measurements on the planar antiferromagnetic chain system TMMC ( $(\text{CH}_3)_4\text{NMnCl}_3$ ) could be well explained in terms of propagating solitons [7]. For an Ising-like system the soliton width,  $d_s$ , decreases to zero, and a quantum mechanical description given by Villain [8] becomes more appropriate. In these systems the non-linear excitations (narrow solitons or kinks) exhibit characteristics comparable with those of the solitons, and can be assumed to be likewise described by an ideal gas approximation. Neutron diffraction experiments on the Ising-like chain system  $\text{CsCoCl}_3$  confirmed the existence and propagation of the kinks [9].

However, in more recent N.M.R. studies of both planar (TMMC) and Ising-like ( $\text{RbFeCl}_3 \cdot 2\text{H}_2\text{O}$ ) chain systems, deviations from the ideal gas description were found [10,11]. Later on they were also found in low energy neutron scattering and neutron spin echo experiments [12-14]. The Mössbauer effect measurements form a welcome complementary experimental technique, since the characteristic Mössbauer frequency window ( $10^5$  to  $10^9$  Hz) is well below the frequencies available for neutron diffraction measurements. Moreover, in comparison with N.M.R. experiments, M.E.S. has the advantage that no magnetic field has to be applied.

About seven years ago, our group started a systematic research of non-linear excitations in low-dimensional magnetic systems by means of M.E.S. The present work is an addition to several articles [15-18] and two previous theses [19,20], of which very short reviews can be found in section 4.1. Two Ising-like antiferromagnetic chain systems,  $\text{FeC}_2\text{O}_4 \cdot 2\text{H}_2\text{O}$  and  $\text{RbFeCl}_3 \cdot 2\text{H}_2\text{O}$ , are the subject of the present study. The first exhibits a large hyperfine field which enhances the experimental resolution. This enables a study of the propagation mechanism of the kinks. The second compound has the advantage of the availability of large single crystals. This provides the possibility of a magnetic field-dependent Mössbauer study, in which interesting information is revealed on both the propagation of the kinks and the impact of the three-dimensional magnetic ordering on their dynamics.

### 1.3 Gold Cluster Compounds as Model Systems for Small Metal Particles

Polynuclear metal cluster compounds are chemically synthesized solids the molecules of which are built up from identical metal cores, surrounded by ligand shells. The ligand shells prevent the metal cores from coalescing. Recently, chemists have succeeded in synthesizing cluster compounds with nuclearities up to 55 metal atoms [21,22]. Even a Pd cluster with a metal core composed of about 560 Pd atoms has been reported [23].

In the last decades physicists have shown a growing interest in small metal particles. On the one hand, this interest is centered on the large fraction of atoms that are located at the surface. Therefore experiments on very small particles provide crucial information on surface effects. On the other hand, theorists were attracted by the expected occurrence of quantum size effects, which arise from the simple fact that the thermodynamic limit is not fulfilled in small particles [24].

Experimental studies to test the proposed models, however, have always suffered from the difficulty of dealing with distributions of particle sizes and shapes. This disadvantage is absent in the polynuclear metal cluster compounds, since these are composed of completely identical clusters, of which in some cases even the structures can be solved. Moreover, one has the opportunity to study physical quantities as a function of nuclearity number, i.e. of particle size.

In the present thesis, we have applied M.E.S. to the study of three polynuclear gold cluster compounds,  $[\text{Au}_9(\text{PPh}_3)_9](\text{NO}_3)_3$ ,  $\text{Au}_{11}(\text{PPh}_3)_7(\text{SCN})_3$ , and  $\text{Au}_{55}(\text{PPh}_3)_{12}\text{Cl}_6$ . The resulting information on the local vibrational density of states will be compared to several models which take the finite size of the particles into consideration. In particular, a comparison between the present results and the prediction of different Debye-Waller factors for inner-core atoms and surface atoms [25] yields interesting results. The vibrations of the centre of mass of the clusters, as predicted by van Wieringen [26], will appear to be of importance. Specific heat measurements, performed on  $\text{Au}_{11}(\text{PPh}_3)_7(\text{SCN})_3$  and  $\text{Au}_{55}(\text{PPh}_3)_{12}\text{Cl}_6$ , will be compared to the specific heat of the metal core, as calculated from the Mössbauer results.

## References

- [1] R.L. Mössbauer, *Z. Physik* 151 (1958) 124 & *Z. Naturforsch.* 14 (1959) 211.
- [2] J.K. Perring and T.H.R. Skyrme, *Nucl. Phys.* 31 (1962) 550.
- [3] A.R. Bishop, J.A. Krumhansl, and S.E. Trullinger, *Physica* 1D (1980) 1.
- [4] "Proceedings of the Soviet-American Symposium on Soliton Theory", Kiev, 1979, *Physica* 3D (1981) 1.
- [5] L.J. de Jongh, *J. Appl. Phys.* 53 (1982) 8018.
- [6] M.B. Fogel, S.E. Trullinger, A.R. Bishop, and J.A. Krumhansl, *Phys. Rev. Lett.* 39 (1977) 1578.
- [7] J.P. Boucher and J.P. Renard, *Phys. Rev. Lett.* 45 (1980) 486.
- [8] J. Villain, *Physica* 79B (1975) 1.
- [9] S.E. Nagler, W.J.L. Buyers, R.L. Armstrong, and B. Briat, *Phys. Rev. Lett.* 49 (1982) 590.
- [10] J.P. Boucher, H. Benner, F. Devreux, L.P. Regnault, J. Rossat-Mignod, C. Dupas, J.P. Renard, J. Bouillot, and W.G. Stirling, *Phys. Rev. Lett.* 48 (1982) 431.
- [11] A.M.C. Tinus, C.J.M. Denissen, H. Nishihara, and W.J.M. de Jonge, *J. Phys. C, Sol. St. Phys.* 15 (1982) L791.
- [12] J.P. Boucher, F. Mesei, L.P. Regnault, and J.P. Renard, *Phys. Rev. Lett.* 55 (1985) 1778.
- [13] J.P. Boucher, L.P. Regnault, R. Pynn, J. Bouillot, and J.P. Renard, *Eur. Phys. Lett.* 1 (1986) 415.
- [14] W.J.L. Buyers, M.J. Hogan, R.L. Armstrong, and B. Briat, *Phys. Rev. Lett.* 57 (1986) 1727.
- [15] R.C. Thiel, H. de Graaf, and L.J. de Jongh, *Phys. Rev. Lett.* 47 (1981) 1415.
- [16] H.J.M. de Groot, L.J. de Jongh, R.C. Thiel, and J. Reedijk, *Phys. Rev. Lett.* 53 (1984) 4041.
- [17] M. ElMassalami, H.H.A. Smit, H.J.M. de Groot, R.C. Thiel, and L.J. de Jongh, in *Proc. in Phys.* 23, "Magnetic Excitations and Fluctuations II", eds. U. Balucani, S.W. Lovesey, M.G. Rasetti, and V. Tognetti, p. 176, Springer-Verlag, Berlin (1987).
- [18] H.H.A. Smit, H.J.M. de Groot, R.C. Thiel, L.J. de Jongh, C.E. Johnson, and M.F. Thomas, *Sol. St. Commun.* 53 (1985) 573.
- [19] H.J.M. de Groot, PhD. Thesis, Rijksuniversiteit te Leiden (1987).
- [20] M. ElMassalami, PhD. Thesis, Rijksuniversiteit te Leiden (1987).
- [21] G. Schmid, R. Pfeil, R. Boese, F. Bandermann, S. Meyer, G.H.M. Calis, and J.W.A. van der Velden, *Chem. Ber.* 114 (1981) 3634.
- [22] G. Schmid and W. Huster, *Z. Naturforsch.* 41B (1986) 1628.
- [23] M.N. Vargaftic, V.P. Zagorodnikov, I.P. Stolyarov, I.I. Moiseev, V.A. Likholobov, D.I. Kochubey, A.L. Chuvilin, V.I. Zaikovskiy, K.I. Zamaraev, and G.I. Timofeeva, *J.C.S. Chem. Comm.*, (1985) 937.
- [24] W.P. Halperin, *Rev. Mod. Phys.* 58 (1986) 533.
- [25] S. Akseleod, M. Pasternak, and S. Bukshpan, *Phys. Rev. Lett.* 37 (1975) 1040.
- [26] J.S. van Wieringen, *Phys. Lett.* 26A (1968) 370.

## 2 Mössbauer Effect Spectroscopy

### 2.1 Introduction

In the pre-Mössbauer era, i.e. before 1958, nuclear resonant fluorescence of  $\gamma$ -rays was already known as an analogue of atomic resonant fluorescence. The conservation of momentum implies that free atoms which emit or absorb a photon suffer a recoil of energy  $E_R = E_\gamma^2/2mc^2$ , where  $E_\gamma$  is the  $\gamma$ -ray energy,  $m$  the atomic mass, and  $c$  the velocity of light in vacuum. For atomic resonant fluorescence, this recoil energy is much smaller than the broadening of the resonance energies due to thermal motions and consequent Doppler shifts. Emission and absorption energies will nearly completely overlap, resulting in a large resonant absorption cross section. For nuclear resonant fluorescence, on the other hand, the recoil energy is so large that the overlap of the emission and absorption energies is very small indeed. To increase this overlap slightly, one can raise the temperature, which enhances the Doppler broadening. However, experiments are very difficult to perform using this technique.

Mössbauer was the first to recognize that another kind of resonance is effective in atoms that are chemically bonded in crystals or molecules [1]. The recoil energy must then be transferred to the system (lattice), of which the resonant atom is a part, and create a phonon. The intriguing difference with free atoms now is that the lattice can be excited with discrete energy quanta only, that in general will not match the recoil energy to be transferred. This results in a fraction of recoil-free events, which means that the  $\gamma$ -ray energy that is emitted or absorbed is exactly equal to the energy difference between excited and ground state. Lipkin [2] has shown that if a large number of events is considered, the average amount of energy transferred to the lattice is exactly equal to the recoil energy. The recoil-free resonance of  $\gamma$ -rays has become an important spectroscopic technique and is referred to as the Mössbauer effect spectroscopy (M.E.S.). It has been applied in many diverse fields as chemistry, physics, biology, geology etc. Numerous review articles and books dealing with M.E.S. can be found [3-7], and therefore no attempt will be made to give a complete overview of the technique. Only those aspects of the M.E.S. that are of relevance to the experiments described in this thesis will be briefly discussed in this chapter.

### 2.2 Mössbauer Effect Spectroscopy

Since the M.E.S. deals with the recoil-free emission and absorption of  $\gamma$ -rays, the  $\gamma$ -ray energy,  $E_\gamma$ , is exactly equal to the difference in energy between excited and ground state of the nucleus

$$E_\gamma = E_{ex} - E_{gr} . \quad (2.1)$$

For the approximately 110 Mössbauer isotopes that are known, these energies are typically between the 6 and 150 keV. In contrast to the emission of  $\gamma$ -rays by free

atoms at finite temperature, the  $\gamma$ -ray energies originating from atoms that are part of a lattice does not show any Doppler broadening due to thermal motions. The vibrations that are present even at zero temperature have frequencies in the order of  $10^{11}$  to  $10^{13}$  Hz, which is a characteristic frequency range for phonons. The period corresponding to this frequency is much shorter than the lifetime of the excited level. Consequently the Doppler shift will be averaged to zero. In view of the Heisenberg uncertainty principle, the energy of the ground state can be precisely determined, because of its infinite lifetime. The energy of the excited state, however, has a certain broadening,  $\Gamma_0$ , due to its finite mean lifetime,  $\tau$ ,

$$\Gamma_0 = \hbar/\tau, \quad (2.2)$$

where  $\hbar$  is Planck's constant divided by  $2\pi$ . The mean lifetimes of the excited states of the Mössbauer isotopes are in the range  $10^{-7}$  to  $10^{-9}$  s. The corresponding uncertainties of the energy are between  $10^{-8}$  and  $10^{-6}$  eV. It is fascinating to notice the twelve orders of magnitude between the experimental resolution and the energy of the nuclear transition used.

The energy distribution  $I(\omega)$  of the  $\gamma$ -ray is assumed to have the form

$$I(\omega) \propto \frac{\Gamma_0/2\pi}{(\omega - E_\gamma)^2 + (\Gamma_0/2)^2}. \quad (2.3)$$

The shape of the energy distribution is Lorentzian, with a width at half maximum of  $\Gamma_0$ , which corresponds to the uncertainty in energy of the excited nuclear level (eq. 2.2).

Due to hyperfine interactions of the nucleus with its environment (i.e. with electrons, the lattice, and external fields), the degeneracy of the nuclear excited and ground state can be lifted and/or the levels can be shifted. In order to investigate these hyperfine interactions, a very precise determination of the relative energies is necessary. For that purpose M.E.S. experiments always make use of both a source and an absorber. The source is given an Doppler shift relative to the absorber. The  $\gamma$ -rays energy,  $E_\gamma(v)$ , as experienced by the absorber can be given by

$$E_\gamma(v) = (1 + v/c)E_\gamma, \quad (2.4)$$

where  $v$  is the Doppler velocity, positive when the source to absorber distance decreases. We will employ Mössbauer experiments in transmission geometry. The transmitted fraction of  $\gamma$ -rays will be minimal when the energy of the  $\gamma$ -rays exactly matches the energy of a transition between a ground and excited state level in the absorber. The transmitted fraction versus energy will be referred to as Mössbauer spectrum and contains all the physical information.

## 2.3 Nuclear Level Splitting

The Hamiltonian for the nucleus of a Mössbauer isotope in a solid can be written as

$$\mathcal{H} = \mathcal{H}_N + \mathcal{H}_{HFS}. \quad (2.5)$$

Table 2.1: Characteristic Mössbauer quantities for  $^{107}\text{Au}$  and  $^{57}\text{Fe}$ . (\*For  $^{107}\text{Au}$ , the Sternheimer shieldings factor,  $1 - R$ , is included in the nuclear quadrupole moment.)

quantity	unit	$^{107}\text{Au}$	$^{57}\text{Fe}$
$\gamma$ -ray energy	(keV)	77.34	14.41
linewidth	( $10^{-9}$ eV)	240.1	4.65
internal conversion coefficient		4.30	8.17
resonant absorption cross section	( $10^{-20}$ cm $^2$ )	3.86	257
nuclear quadrupole moment ( $I = \frac{3}{2}$ )	(barn)	0.594	0.20
ground state magnetic moment	( $\mu_N$ )	0.144865	0.0902
excited state magnetic moment	( $\mu_N$ )	0.417	-0.1547
nuclear spin quantum number, $I_{gr}, I_{ex}$		$\frac{3}{2}, \frac{1}{2}$	$\frac{1}{2}, \frac{3}{2}$
recoil energy	( $10^{-2}$ eV)	1.63	0.195
natural isotope abundance	(%)	100	2.17
energy equivalent of 1 mm/s	( $10^{-8}$ eV)	25.8	4.80
	(MHz)	62.39	11.6
Sternheimer shielding factor, $1 - R$		1*	0.68
Sternheimer anti-shielding factor, $1 - y_\infty$		66.58	10.1
$\langle r_Q^{-3} \rangle$ for Au-5d and Fe-3d	(a.u.)	12.3	4.93
$\langle r_Q^{-3} \rangle$ for Au-6p	(a.u.)	14.6	
$\langle r_M^{-3} \rangle$ for Fe-3d	(a.u.)		4.57

The intra-nuclear forces described by  $\mathcal{H}_N$  give rise to different nuclear states, that are characterized by their spin quantum number  $I$ . The Mössbauer effect will generally make use of the lowest excited state, since it ensures the highest recoil-free fraction. For  $^{57}\text{Fe}$  and  $^{107}\text{Au}$ , the two Mössbauer isotopes that will be used in this work, these excited states have an energy of 14.41 and 77.34 keV respectively. These and other characteristic Mössbauer quantities can be found in table 2.1. The recoil-free emitted  $\gamma$ -rays have a very narrow energy distribution, enabling the observation of the hyperfine splittings and shifts contained in the second term in eq. 2.5. This term can be expressed in a multipole expansion

$$\mathcal{H}_{HFS} = \mathcal{H}_{E_0} + \mathcal{H}_{M_1} + \mathcal{H}_{E_2}. \quad (2.6)$$

Only the three lowest order terms are given, since the higher order terms are usually negligible. The electric monopole interaction,  $E_0$ , is referred to as isomer shift (I.S.) or sometimes chemical shift, and shifts the energy levels of both the ground and the excited state. It originates from the coulomb interaction of the nucleus with the electrons, that have a finite density at the nucleus. The magnetic dipole ( $M_1$ ) interaction removes the degeneracy of the nuclear levels if the nuclear spin quantum number is non-zero. It is commonly known as the magnetic hyperfine interaction and describes the influence of a magnetic field upon the nuclear spin.  $E_2$ , the third term in eq. 2.6, is the electric quadrupole interaction. It splits the nuclear energy levels if the nucleus possesses a quadrupole moment and an electric field gradient



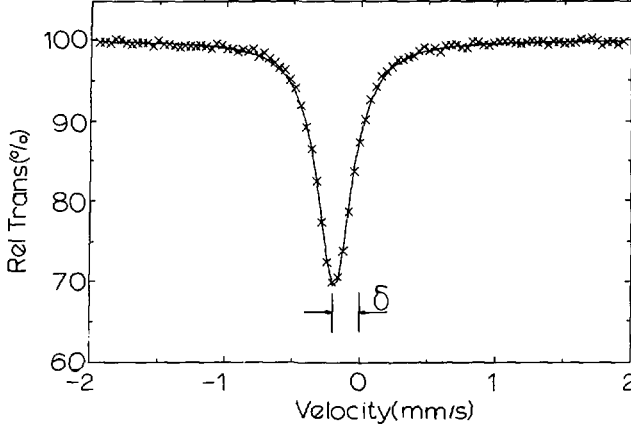


Figure 2.1:  $^{57}\text{Fe}$  Mössbauer spectrum of  $\text{K}_4\text{Fe}(\text{CN})_6 \cdot 3\text{H}_2\text{O}$  at 4.2 K, which illustrates the isomer shift denoted by  $\delta$ .

is present at the nucleus. It is usually referred to as quadrupole splitting (Q.S.). In the following we will discuss the three hyperfine interactions separately.

### 2.3.1 Isomer Shift

The electric monopole energy of a uniform spherical nucleus with radius  $R$  and charge  $Ze$  in a constant electron charge density  $-e|\Phi(0)|^2$  can be given by

$$\mathcal{H}_{E_0} = \frac{2}{5} \pi Z e^2 |\Phi(0)|^2 R^2. \quad (2.7)$$

In standard Mössbauer experiments it is legitimate to assume that the electronic state of the atom, and consequently  $|\Phi(0)|^2$ , does not change during the Mössbauer event. In general the nuclear radii of the ground and excited state differ by a relatively small amount  $\delta R$ . As a result, the nucleus gains or loses coulomb energy when it emits a  $\gamma$ -ray. This energy is transferred to the  $\gamma$ -ray and therefore produces a shift. In the absorber the inverse process i.e. resonant absorption takes place, and the same explanation can be given for the energy shift. The total I.S.,  $\delta$ , is given by

$$\delta = \frac{4}{5} \pi Z e^2 R^2 \delta R / R \{ |\Phi_a(0)|^2 - |\Phi_s(0)|^2 \}, \quad (2.8)$$

where the subscripts  $a$  and  $s$  refer to the absorber and source respectively. A Mössbauer spectrum that illustrates a shifted resonance line is given in fig. 2.1. Since in M.E.S. experiments both a source and absorber are used, only relative shifts can be determined. It is common practice to relate the I.S. to a standard material, for which  $\alpha$ -Fe and Au in Pt have been chosen for the two Mössbauer isotopes used in this thesis.

With the I.S. we have a spectroscopic quantity that can sample minute changes in the electronic density at the nucleus. Since only the  $s$ -electrons have a finite

density at the nucleus, they are responsible for the main contribution to the I.S. The chemical environment of the Mössbauer atom does not have an influence on the inner *s*-electrons. Their density at the nucleus and contribution to  $|\Phi(0)|^2$  will be equal in source and absorber. The occupation of the outer *s*-electron shell, on the other hand, can vary drastically and will have a large influence on the I.S. Non-relativistic calculations show a zero electron density at the nucleus for *p*-, *d*-, and *f*-electrons. The valence *p*-, *d*-, or *f*-electrons have therefore only an indirect influence on the I.S. by their shielding effect on the outer *s*-electron shells. For Mössbauer isotopes with a high atomic number like gold, relativistic calculations have shown that as a result of the large nuclear charge, the electrons at the nucleus have such a large kinetic energy, that time dilatation becomes important. The I.S. as predicted by eq. 2.8, may then be slightly enhanced [8]. Moreover, relativistic calculations show that the density of the *p*-electrons at the nucleus is non-zero for isotopes with high atomic number. This means that *p*-electrons can also have a small direct effect on the I.S., especially when they form a part of the valence orbitals [9].

Another relativistic effect, commonly referred to as second order Doppler shift, also contributes to the I.S. The emitting nucleus vibrates with a frequency of  $10^{12}$  Hz. This is much faster than the Mössbauer time scale, resulting in a zero first order Doppler shift. However, from a relativistic viewpoint the nucleus suffers time dilatation with respect to the laboratory coordinate system. In this coordinate system, the  $\gamma$ -ray frequency ( $\omega$ ) is lower than that corresponding to the energy difference between excited and ground state ( $\omega_0$ ), and can be given by

$$\omega = \omega_0 \sqrt{1 - \langle v^2 \rangle / c^2} \approx \omega_0 (1 - \langle v^2 \rangle / 2c^2). \quad (2.9)$$

The thermal average of the velocity squared,  $\langle v^2 \rangle$ , can quite easily be calculated in the Debye approximation. For the second order Doppler shift,  $\delta_{SOD}$ , at temperature  $T$  one obtains [4]

$$\delta_{SOD} = \frac{1}{2mc} \left\{ \frac{9}{8} k_B \theta_D + 9 k_B \frac{T^4}{\theta_D^3} \int_0^{\theta_D/T} \frac{x^3 dx}{\exp(x) - 1} \right\}, \quad (2.10)$$

where  $m$  is the mass of the Mössbauer nucleus,  $\theta_D$  the Debye temperature, and  $k_B$  the Boltzmann's constant.

The gold Mössbauer experiments described in this thesis have been performed at temperatures up to 42 K. Assuming a Debye temperature of 168 K, which is appropriate for metallic gold, one obtains a second order Doppler shift of 0.0015 mm/s between 4.2 and 42 K. Since the experimental resolution is determined by the linewidth, which equals to  $\sim 1.9$  mm/s, the second order Doppler shift will be negligible in the present gold measurements.

$^{57}\text{Fe}$  M.E.S. measurements have been performed between 0.6 and 293 K. The second order Doppler shift due to this temperature difference for a salt with a Debye temperature of 200 K is 0.168 mm/s. For the  $^{57}\text{Co}:\text{Rh}$  source, having a Debye temperature of roughly 400 K,  $\delta_{SOD}$  is calculated to be 0.128 mm/s between liquid

helium and room temperature and 0.121 mm/s between liquid nitrogen and room temperature. Since the experimental linewidth for iron is equal to  $\sim 0.25$  mm/s, the second order Doppler shift becomes noticeable over temperature differences of tens of degrees Kelvin.

### 2.3.2 Magnetic Hyperfine Interaction

In the discussion of the magnetic hyperfine interaction, we will focus on the  $^{57}\text{Fe}$  isotope, since the Au samples described in this thesis did not show any magnetic hyperfine interaction. The magnetic hyperfine interaction will be treated in the effective field approximation, which is valid as long as the electronic levels of the Mössbauer atom are not affected by the hyperfine interaction. In general, this is the case, since the electronic splitting is orders of magnitude larger than the nuclear level splitting. A counter example is a Kramers ion with an  $S_x = \pm \frac{1}{2}$  degenerate ground state. In such a case, a Hamiltonian describing both the electronic and the nuclear states simultaneously should be solved [10].

The nuclear Hamiltonian describing the magnetic hyperfine interaction in the effective field approximation can be given by

$$\mathcal{H}_{M_I} = -\vec{\mu} \cdot \vec{H}_{eff} = -g\mu_N \vec{I} \cdot \vec{H}_{eff}, \quad (2.11)$$

where  $\vec{H}_{eff}$  is the effective magnetic field at the nucleus and  $\vec{\mu}$  is the nuclear moment.  $g$ ,  $\mu_N$ , and  $\vec{I}$  are the nuclear g-factor, nuclear magneton, and nuclear spin operator respectively. The degenerate sublevels of the nuclear ground and excited state are split by this nuclear Zeeman interaction into  $2I + 1$  equidistant sublevels. Their energy shift  $E_i$  due to the effective field can be given by

$$E_i = -g\mu_N H_{eff} m_I, \quad m_I = -I, -I + 1, \dots, I, \quad (2.12)$$

where  $m_I$  is the nuclear magnetic spin quantum number. Since the Mössbauer transition in  $^{57}\text{Fe}$  is of the magnetic dipole type ( $M_1$ ), only nuclear sublevels with  $\Delta m_I = 0, \pm 1$  are coupled by the  $\gamma$ -rays. This selection rule permits only six transitions between the two ground state sublevels ( $I_0 = \frac{1}{2}$ ) and the four excited state sublevels ( $I_1 = \frac{3}{2}$ ). A spectrum illustrating such a sextet due to magnetic hyperfine interaction is shown in fig. 2.2.

The effective magnetic hyperfine field that the nucleus experiences can find its origin in the ion itself,  $\vec{H}_{ion}$ , can be generated by the ions of the lattice,  $\vec{H}_{lat}$ , or can be due to an applied magnetic field,  $\vec{H}_{app}$ .

$$\vec{H}_{eff} = \vec{H}_{ion} + \vec{H}_{lat} + \vec{H}_{app}. \quad (2.13)$$

The field induced by the moments of the surrounding ions,  $\vec{H}_{lat}$ , originates from the dipolar interaction. Since the compounds described in this thesis are insulators, there are no conduction electrons present to give rise to a transferred hyperfine field.  $\vec{H}_{lat}$  contains both the demagnetizing field and the Lorentz field, and can be

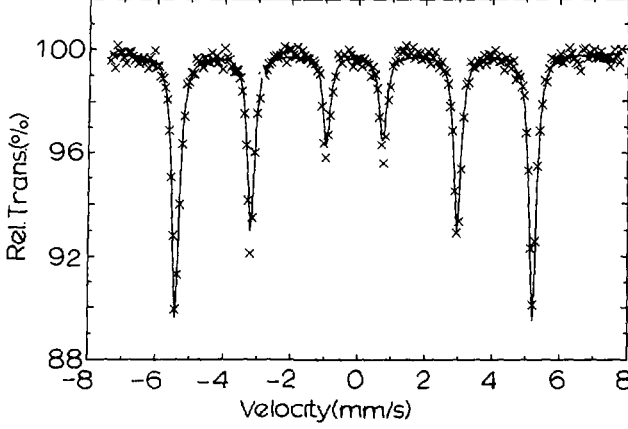


Figure 2.2:  $^{57}\text{Fe}$  Mössbauer spectrum of  $\alpha\text{-Fe}$ , which illustrates a sextet that results from the nuclear Zeeman interaction.

calculated at site  $i$  by summing the contribution of the individual ionic spins,  $\vec{S}_j$ , on sites  $j$

$$\vec{H}_{\text{lat}} = g\mu_B \sum_j \left\{ \frac{\vec{S}_j}{|\vec{r}_{ij}|^3} - \frac{3\vec{r}_{ij}(\vec{S}_j \cdot \vec{r}_{ij})}{|\vec{r}_{ij}|^5} \right\}, \quad (2.14)$$

where  $g$  and  $\mu_B$  are the electronic  $g$ -factor and the Bohr magneton respectively, and  $\vec{r}_{ij}$  is difference vector between lattice site  $i$  and  $j$ .

For the first term in eq. 2.13, three contributions can be distinguished [11]

$$\vec{H}_{\text{ion}} = \vec{H}_{fc} + \vec{H}_{\text{dip}} + \vec{H}_{\text{orb}}. \quad (2.15)$$

The first term expresses the Fermi contact field. In the classical description, the contribution due to each electron, with spin  $\vec{S}$  and electron density  $|\Phi_e(0)|^2$  at the nucleus, can be given by

$$\vec{H}_{fc} = -\frac{16}{3} \mu_B \vec{S} |\Phi_e(0)|^2. \quad (2.16)$$

Evidently, only  $s$ -electrons contribute to the Fermi contact field. Generally, a field generated by a spin up is nearly completely compensated by that generated by a spin down. In the case of iron, an isolated atom will align the moments of the unpaired 3d electrons along an applied magnetic field. Their spins are anti-parallel to their moments. The direct exchange yields an attraction between 3d electrons and  $s$ -electrons with parallel spin, enhancing the opposite spin density at the nucleus. The direction of the Fermi contact field is anti-parallel to this spin. Consequently, the Fermi contact field is negative by definition, which means anti-parallel to the magnetic moments of the 3d electrons.

The second term in eq. 2.15,  $\vec{H}_{\text{dip}}$ , is the dipolar field which for electrons with spin  $\vec{S}_j$  at position  $\vec{r}_{ij}$  relative to the nucleus at site  $i$  will be given by eq. 2.14. The

last term in eq. 2.15,  $\vec{H}_{orb}$ , represents the orbital contribution to the effective field, which for a single electron with orbital momentum  $\vec{L}$  at position  $\vec{r}$  in the classical description can be written as

$$\vec{H}_{orb} = -2\mu_B \frac{\vec{L}}{|\vec{r}|^3}. \quad (2.17)$$

Since the spin orbit coupling aligns the electronic spin parallel to the orbital momentum, the field is positive, i.e. parallel to the magnetic moment of the 3d electrons.

For high spin ferric compounds, with an electron configuration ( $3d^5, ^6S$ ), the dipolar field due to its own electrons and the contribution to the effective field of the orbital momentum are zero. The Fermi contact term, that can be estimated to be  $-11$  T per saturated 3d electron, dominates the contributions to the effective field of the neighbouring dipoles and the applied field. In high spin ferrous compounds, on the other hand, a negative Fermi contact term is opposed by a positive orbital contribution of the same order of magnitude. The positive dipolar contribution is generally quite small. It is therefore impossible to say beforehand whether the internal hyperfine field,  $H_{ion}$ , is positive or negative. In practice, one may apply an external field that aligns the 3d moments. This results at the nucleus in a vector sum of the applied and internal field, making it possible to determine the sign of the latter.

### 2.3.3 Quadrupole Splitting

Nuclei with a spin quantum number  $I > \frac{1}{2}$  may have a non-spherical charge distribution. Their nuclear quadrupole moment  $Q$  can be calculated by the spacial integral

$$eQ = \int dv \sigma r^2 (3\cos^2\theta - 1), \quad (2.18)$$

where  $e$  is the proton charge and  $\sigma$  is the charge density at spherical coordinates  $r$  and  $\theta$ . The sign of the nuclear quadrupole moment is positive if the shape of the charge distribution is elongated, and negative if it is flattened.

Often the charge distribution of the electrons and/or of the neighbouring ions around the nucleus is not spherical, resulting in a non-zero electric field gradient (E.F.G.). The E.F.G. can be given by the symmetrical electric field gradient tensor, of which the elements are given by the second derivative of the potential  $V$ ,

$$V_{ij} = \frac{\partial^2 V}{\partial i \partial j}, \quad (i, j = x, y, z). \quad (2.19)$$

The Laplace equation requires the tensor to be traceless,

$$V_{xx} + V_{yy} + V_{zz} = 0. \quad (2.20)$$

Furthermore, it is possible to define a principle coordinate system along the main axes of the E.F.G., transforming the tensor into a diagonal one. In this coordinate

system, the E.F.G. is described by two independent parameters, generally taken to be  $V_{zz}$  and  $\eta$ . The asymmetry parameter  $\eta$  is defined as

$$\eta = \frac{V_{xx} - V_{yy}}{V_{zz}}, \quad (2.21)$$

where it is common practice to chose  $|V_{xx}| > |V_{yy}| \geq |V_{zz}|$ , and consequently  $0 \leq \eta \leq 1$ . If one deals with axial symmetry,  $\eta$  is zero. This occurs when the site symmetry at the Mössbauer nucleus contains a three- or higher-fold rotation axis, coinciding with the  $V_{zz}$  direction. The E.F.G. vanishes completely if two three- or higher-fold rotation axes are mutually perpendicular (e.g. in cubic symmetry).

The quadrupole splitting arises from the interaction between the nuclear quadrupole moment and the non-zero E.F.G., and is described by the Hamiltonian

$$\mathcal{H}_{E_2} = \frac{eQV_{zz}}{4I(2I-1)} \left\{ 3\hat{I}_x^2 - I(I+1) + \frac{\eta}{2} (\hat{I}_+^2 + \hat{I}_-^2) \right\}, \quad (2.22)$$

where  $\hat{I}_x$  and  $I$  are the nuclear spin operator and nuclear spin quantum number respectively.  $\hat{I}_+$  and  $\hat{I}_-$  are the raising and lowering operators. The nuclear sub-states  $|I, m_I\rangle$ , where  $m_I$  is the nuclear magnetic spin quantum number, suffer an energy shift due to the quadrupole splitting that is given by

$$E_Q = \frac{eQV_{zz}}{4I(2I-1)} \left\{ 3m_I^2 - I(I+1) \right\} \left( 1 + \frac{\eta^2}{3} \right)^{\frac{1}{2}}. \quad (2.23)$$

If magnetic interaction is absent, the quadrupole interaction gives rise to a doublet for both gold and iron. For the splitting one obtains

$$\epsilon = \frac{1}{2} eQV_{zz} \left( 1 + \frac{\eta^2}{3} \right)^{\frac{1}{2}}. \quad (2.24)$$

An illustration of a quadrupole split spectrum is shown in fig. 2.3.

By means of the quadrupole splitting, the M.E.S. becomes an accurate probe for the chemical environment that determines the E.F.G. at the nucleus of the Mössbauer atom. The E.F.G. is composed of two contributions. The first is the lattice contribution arising from the non-spherical charge distribution of the surrounding ions. The second, referred to as valence contribution, originates from the non-spherical charge distribution of the electrons in the partly filled valence orbitals of the Mössbauer atom itself.

$$\begin{aligned} V_{zz} &= (1 - y_{\infty})V_{zz}^{lat} + (1 - R)V_{zz}^{val} \\ \eta V_{zz} &= (1 - y_{\infty})\eta^{lat}V_{zz}^{lat} + (1 - R)\eta^{val}V_{zz}^{val}, \end{aligned} \quad (2.25)$$

where *lat* and *val* indicate the lattice and valence contribution.  $y_{\infty}$  is called the Sternheimer anti-shielding factor. It represents the polarization of the inner-core electrons, and in most M.E.S. isotopes enhances the lattice contribution. The Sternheimer shielding factor,  $R$ , has a value between 0 and 1, indicating that the E.F.G. due to the valence electrons is reduced by the inner-core electrons.

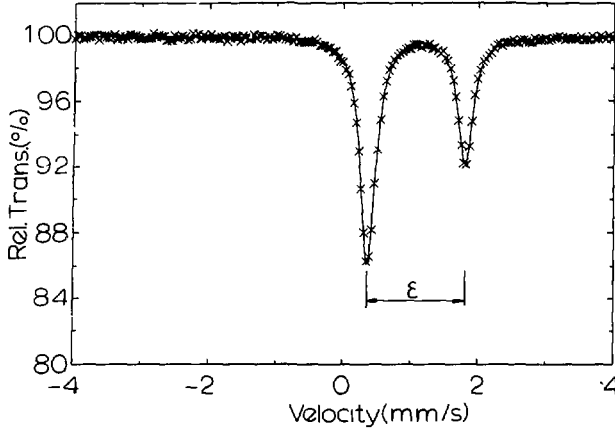


Figure 2.3:  $^{57}\text{Fe}$  Mössbauer spectrum of  $\text{RbFeCl}_3 \cdot 2\text{H}_2\text{O}$  at 40 K, illustrating a quadrupole doublet with an energy splitting  $\epsilon$ .

The lattice contribution can be estimated by a point charge lattice sum

$$\begin{aligned} V_{ss}^{\text{lat}} &= \sum_j Z_j \frac{3 \cos^2 \theta_j - 1}{r_j^3}, \\ \eta^{\text{lat}} V_{ss}^{\text{lat}} &= \sum_j Z_j \frac{3 \sin^2 \theta_j \cos 2\phi_j}{r_j^3}, \end{aligned} \quad (2.26)$$

where  $Z_j$  is the charge of an ion with spherical coordinates  $r_j$ ,  $\theta_j$ , and  $\phi_j$ . The sum runs in principle over the entire lattice, but in general very good convergence is found already within a sphere with a diameter of several nm. In practice, reasonable agreement between lattice sum and experimentally observed E.F.G. is obtained for ionic salts. In the case of covalently bonded compounds, an empirically found effective charge is often assigned to the different ions. This must account for the incomplete charge transfer, the finite size and the polarizability of the surrounding atoms. S-state Mössbauer ions, like high spin  $\text{Fe}^{3+}$ , have a spherical valence electron distribution. Therefore only the lattice contributes then to the E.F.G.

The valence electrons in the 3d atomic orbital, and the 5d and 6p atomic orbitals are the main contributors to the E.F.G. in high spin ferrous and gold compounds, respectively. The principal component and asymmetry parameter due to an unpaired electron with wave function  $|\Phi\rangle$  can be given by

$$\begin{aligned} V_{ss}^{\text{val}} &= -e \langle \Phi | (3 \cos^2 \theta - 1) r^{-3} | \Phi \rangle, \\ \eta^{\text{val}} V_{ss}^{\text{val}} &= -e \langle \Phi | (3 \sin^2 \theta \cos 2\phi) r^{-3} | \Phi \rangle, \end{aligned} \quad (2.27)$$

where  $-e$  is the electronic charge and  $r$ ,  $\theta$ , and  $\phi$  are the spherical coordinates of the electron. Since the wave function can be split into a radial,  $R(r)$ , and an angular

Table 2.2: Values of  $\langle Y(\theta, \phi) | 3 \cos^2 \theta - 1 | Y(\theta, \phi) \rangle$  and  $\eta$  for p- and d-orbitals.

orbital	$\langle Y f(\theta) Y \rangle$	$\eta$	orbital	$\langle Y f(\theta) Y \rangle$	$\eta$
$p_x$	$+\frac{2}{5}$	-3	$d_{x^2}$	$-\frac{4}{7}$	0
$p_y$	$+\frac{2}{5}$	+3	$d_{x^2-y^2}$	$+\frac{4}{7}$	0
$p_z$	$-\frac{4}{5}$	0	$d_{xy}$	$+\frac{4}{7}$	0
			$d_{yz}$	$-\frac{2}{7}$	-3
			$d_{zx}$	$-\frac{2}{7}$	+3

part,  $Y(\theta, \phi)$ , eq. 2.27 reduces to

$$\begin{aligned} V_{zz}^{val} &= -e \langle r_Q^{-3} \rangle \langle Y(\theta, \phi) | 3 \cos^2 \theta - 1 | Y(\theta, \phi) \rangle, \\ \eta^{val} V_{zz}^{val} &= -e \langle r_Q^{-3} \rangle \langle Y(\theta, \phi) | 3 \sin^2 \theta \cos 2\phi | Y(\theta, \phi) \rangle, \end{aligned} \quad (2.28)$$

where  $\langle r_Q^{-3} \rangle$  is the expectation value of  $r^{-3}$  and is given in table 2.1. The last factors in eqs. 2.28 are zero for the s-electrons, and are given in table 2.2 for p- and d-electrons.

The electronic configuration of the gold compounds investigated in this thesis are best described in terms of molecular orbitals. The 5d and 6p atomic orbitals, that form part of the basis of the molecular orbital, will to some extent be depopulated and populated respectively. The quadrupole splitting depends on the difference in population of the 5d<sub>i</sub> and 6p<sub>i</sub> orbitals.

We will also deal with some high spin ferrous compounds. The electronic configuration of the 3d shell is known to be (3d<sup>6</sup>, <sup>5</sup>D). The partly filled 3d orbital gives rise to a valence contribution to the E.F.G., that generally dominates the E.F.G. due to the lattice. Since covalency effects can be neglected and the contribution to the E.F.G. of each orbital wave function is known, the quadrupole splitting and the asymmetry parameter can be calculated when the crystal field levels are known.

Crystal field theory describes the interaction of a single electron in a electric field due to the surrounding ligands. The crystal field Hamiltonian can be written as

$$\mathcal{H}_c = \sum_{nm} B_n^m \hat{O}_n^m, \quad (2.29)$$

where  $B_n^m = A_n^m \langle r^n \rangle \theta_n$ .  $\hat{O}_n^m$  are the Stevens operator equivalents [12], of which the matrix elements with respect to the basis  $|LL_xSS_x \rangle$  can be found in [13]. The numerical constants,  $\theta_n$ , can be found in the same reference.  $\langle r^n \rangle$  is the expectation value of  $r^n$ , where  $r$  is the distance of the electron to the origin.  $A_n^m$  can be calculated by assuming the ligands to be point charges and describing the potential in terms of spherical harmonics. Since the potential function reflects the point symmetry of the lattice site, only terms corresponding to a specific distortion remain. Instead of calculating  $B_n^m$  in eq. 2.29, it is more useful to treat them as empirical parameters. For d-electrons, terms with  $n$  up to 4 should be considered. Terms with odd  $n$  vanish because of inversion symmetry. In the case



of orthorhombic distortions, the Hamiltonian including spin-orbit coupling, can be given by [14]

$$H = \frac{Dq}{12}(\hat{O}_4^0 + 5\hat{O}_4^4) + \frac{Ds}{3}\hat{O}_2^0 - \frac{Dt}{12}\hat{O}_4^0 + \frac{Dr}{3}\hat{O}_2^2 - \frac{Dv}{12}\hat{O}_4^2 + \lambda \hat{L} \cdot \hat{S}, \quad (2.30)$$

where  $Dq$  is the cubic crystal field.  $Ds$  and  $Dt$  represent the tetragonal, and  $Ds$  and  $Dt$  the orthorhombic distortions. The relationship

$$\frac{Dr}{Dv} = -\frac{3Ds}{5Dt} \quad (2.31)$$

can be introduced if the distance to the surrounding atoms are equal and the charges on the atoms nearly equal, or vice versa [14]. Diagonalization of eq. 2.30 yields 25 eigenvalues,  $E_i$ , and eigenvectors,  $|\Phi_i\rangle = \sum_{LSS_x} a_i^{LSS_x} |LL_xSS_x\rangle$ . For each state, the valence contribution to the E.F.G. can be given by [15]

$$\begin{aligned} \langle V_{xx}^i \rangle &= \frac{2e}{21} \langle r_M^{-3} \rangle \langle \Phi_i | \hat{O}_2^0 | \Phi_i \rangle, \\ \langle \eta^i V_{xx}^i \rangle &= \frac{2e}{7} \langle r_M^{-3} \rangle \langle \Phi_i | \hat{O}_2^2 | \Phi_i \rangle. \end{aligned} \quad (2.32)$$

Generally, the transitions between the electronic states are much faster than the quadrupole precession time, which for iron is typically  $10^{-8}$  s. The observed quadrupole splitting is then the thermal average of eq. 2.32

$$\begin{aligned} \langle V_{xx} \rangle_T &= \frac{\sum_i \langle V_{xx}^i \rangle f_i}{\sum_i f_i}, \\ \langle \eta V_{xx} \rangle_T &= \frac{\sum_i \langle \eta_i V_{xx}^i \rangle f_i}{\sum_i f_i}, \end{aligned} \quad (2.33)$$

where  $f_i = \exp(-E_i/k_B T)$ . The empirical parameters of eq. 2.30 can now be refined, such that  $V_{xx}$  and  $\eta$  are predicted correctly between e.g. helium and room temperature. Extra information about the crystal field levels can be obtained from standard infrared absorption data. The energy levels of the lowest quintuplet can be used to determine an effective spin Hamiltonian [16].

### 2.3.4 Combined Quadrupole and Magnetic Hyperfine Interactions

When a quadrupole and a magnetic hyperfine interaction are simultaneously present, the Hamiltonians given in equations 2.11 and 2.22 are no longer valid. This will be the case at low temperatures in the ferrous compounds studied in this thesis. The combined Hamiltonian can then be chosen to be

$$\mathcal{H} = \frac{eQV_{xx}}{4I(2I-1)} \{3\hat{I}_x^2 - I(I+1) + \frac{\eta}{2}(\hat{I}_+^2 + \hat{I}_-^2)\} - g\mu_N \vec{H}_{eff} \cdot \vec{I}. \quad (2.34)$$

In general no analytic expression can be given. The Hamiltonian, of which the matrix elements with respect to the basis  $|I, m_I\rangle$  can be found in ref. [17], has to

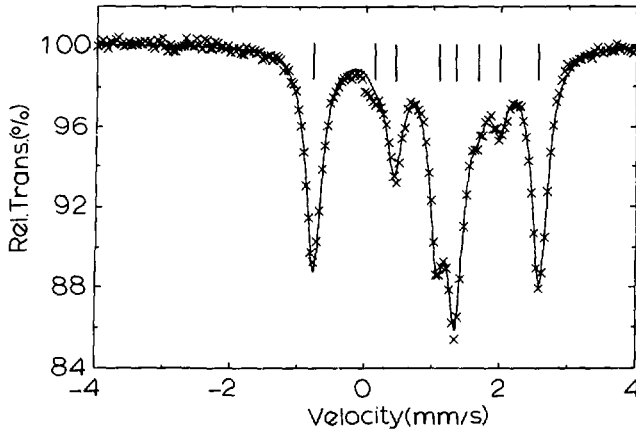


Figure 2.4:  $\text{RbFeCl}_3 \cdot 2\text{H}_2\text{O}$  at 4.2 K shows the eight nuclear transitions, each of which has a finite probability.

be diagonalized numerically. The resulting eigenvalues,  $E_i$ , determine the transition energies between substates of the ground and excited level. The substates can be given by a linear combination of the basis states

$$|a\rangle = \sum_{m_0} C_{m_0} |I_0, m_0\rangle, \quad |b\rangle = \sum_{m_1} C_{m_1} |I_1, m_1\rangle, \quad (2.35)$$

where the constants  $C_{m_0}$  and  $C_{m_1}$  form the eigenvectors corresponding to the Hamiltonian of eq. 2.34. Due to the mixing of the basis states  $|I, m_I\rangle$ , an eight line Mössbauer spectrum results, see fig. 2.4. A systematic way of extracting the Mössbauer parameters from an eight line spectrum is to fit it using four pairs of Lorentzians with equal splitting. The five position parameters represent the four levels of the  $I_1 = \frac{3}{2}$  state and the splitting of the  $I_0 = \frac{1}{2}$  state. In the case of a powder absorber and pure magnetic dipolar radiation ( $M_1$ ), the intensity of the four doublets can be constrained to be equal [18]. From the five position parameters the I.S.,  $H_{eff}$ , and the Q.S. can be calculated. For a positive as well as a negative Q.S., a range of possible values for  $\eta$ ,  $\theta$ , and  $\phi$  can be given [19].

## 2.4 Relative Intensities

The  $\gamma$ -ray can be described by a plane wave, for which the vector potential,  $\vec{A}(\vec{r})$ , can be expanded in multipoles. The vector potential,  $\vec{A}(\vec{r})$ , has an interaction with a particle with spin  $\vec{S}$  and momentum  $\vec{p}$ . The probability amplitude for a transition from a state  $|I_1 m_1\rangle$  to state  $|I_0 m_0\rangle$ , with emission of a circularly polarized photon along direction  $\vec{k}$ , is proportional to the matrix element of the interaction

Table 2.3: Clebsch-Gordan coefficients  $\langle \frac{5}{2}m_1 | \frac{1}{2}m_2 Lm \rangle$  for  $M_1$  and  $E_2$  radiation [37].

$m_1$	$m_2$	$m$	$L = 1$	$L = 2$
$\frac{5}{2}$	$-\frac{1}{2}$	-2	0	$\sqrt{\frac{4}{10}}$
$\frac{3}{2}$	$-\frac{1}{2}$	-1	$\sqrt{\frac{1}{6}}$	$-\sqrt{\frac{8}{10}}$
$-\frac{1}{2}$	$-\frac{1}{2}$	0	$-\sqrt{\frac{2}{6}}$	$\sqrt{\frac{2}{10}}$
$-\frac{3}{2}$	$-\frac{1}{2}$	1	$\sqrt{\frac{3}{6}}$	$-\sqrt{\frac{1}{10}}$
$-\frac{5}{2}$	$-\frac{1}{2}$	-1	$\sqrt{\frac{3}{6}}$	$\sqrt{\frac{1}{10}}$
$-\frac{3}{2}$	$\frac{1}{2}$	0	$-\sqrt{\frac{2}{6}}$	$-\sqrt{\frac{2}{10}}$
$-\frac{1}{2}$	$\frac{1}{2}$	1	$\sqrt{\frac{1}{6}}$	$\sqrt{\frac{3}{10}}$
$\frac{1}{2}$	$\frac{1}{2}$	2	0	$-\sqrt{\frac{4}{10}}$

[20]

$$A_{m_1 m_0}^q(\vec{k}) = \sum_L \sqrt{2L+1} q^{L-1} D_{m_0}^L(\alpha, \beta, \gamma) \langle I_1 m_1 | I_0 m_0 L m \rangle \langle I_1 || \alpha_L^q T_L^* || I_0 \rangle, \quad (2.36)$$

where  $q$  is  $+1$  and  $-1$  for right and left circular polarization and  $m = m_2 - m_1$ . The sum extends over the multipole order  $L$ , with  $\pi = e$  for electric and  $\pi = m$  for magnetic multipole radiation, if  $L$  is even and odd respectively. The last two factors are the Clebsch-Gordan coefficients and the reduced matrix elements of the multipole radiation of order  $L$ , which are obtained by the application of the Wigner-Eckart theorem [20]. In the case of the 14.41 keV transition of  $^{57}\text{Fe}$ , the only non-zero reduced matrix element is that of the magnetic dipole ( $M_1$ ) radiation ( $L = 1$ ). For the  $^{197}\text{Au}$  Mössbauer transition, mixed  $M_1$  and  $E_2$  (electric quadrupole,  $L = 2$ ) radiation is observed. The relative magnitude of their intensities is expressed in the mixing parameter,  $\delta$ , which is the ratio of the reduced matrix elements of  $E_2$  and  $M_1$  radiation. Experimental determination by Prosser et al. [21] gave  $\delta = -0.354(\pm 0.005)$ , where the sign corresponds to the relative phase. The Clebsch-Gordan coefficients of the two relevant multipole transitions are given in table 2.3. The matrix elements,  $D_{m_0}^L(\alpha, \beta, \gamma)$  in eq. 2.36, rotate the nuclear quantization axes over the Euler angles  $\alpha, \beta, \gamma$  into a coordinate system with the  $z$  axis along the  $\gamma$ -ray direction. They are given by

$$D_{m_0}^L(\alpha, \beta, \gamma) = e^{-i m_0 \alpha} d_{m_0}^L(\beta) e^{-i q \gamma}, \quad (2.37)$$

where the reduced matrix elements  $d_{m_0}^L(\beta)$  can e.g. be found in ref. [20]. Generally the two states,  $|a\rangle$  and  $|b\rangle$ , between which the transition takes place are linear combinations of the basis states,  $|I, m_I\rangle$  (see eq. 2.35). This yields for the matrix elements of eq. 2.36

$$A_{ab}^q(\vec{k}) = \sum_L \sum_{m_0} \sum_{m_1} C_{m_0}^{I_0} C_{m_1}^{I_1} \sqrt{2L+1} q^{L-1} D_{m_0}^L(\alpha, \beta, \gamma) \langle I_1 m_1 | I_0 m_0 L m \rangle \langle I_1 || \alpha_L^q T_L^* || I_0 \rangle. \quad (2.38)$$

Since the performed measurements are polarization insensitive, the probability,  $P_{ab}(\vec{k})$ , that a transition takes place is the incoherent sum over the polarization index  $q$

$$P_{ab}(\vec{k}) = \sum_{q=\pm 1} |A_{ab}^q(\vec{k})|^2. \quad (2.39)$$

Consequently, the factor containing  $\gamma$  in eq. 2.37 drops out, and  $\alpha$  and  $\beta$  can be replaced by  $\phi$  and  $\theta$  respectively. These denote the azimuthal and polar angle of the  $\gamma$ -ray direction with respect to the quantization axes which define the states  $|I, m_I\rangle$ . The resulting probability for a transition from  $|a\rangle$  to  $|b\rangle$  to occur can be written as

$$P_{ab}(\vec{k}) \propto \sum_L \sum_{L'} \sum_{m_0} \sum_{m_1} \sum_{m'_0} \sum_{m'_1} C_{m_0}^{I_0^*} C_{m_1}^{I_1} C_{m'_0}^{I_0} C_{m'_1}^{I_1^*} \delta^{L+L'-2} \\ < I_1 m_1 | I_0 m_0 L m \rangle \langle I_1 m'_1 | I_0 m'_0 L' m' \rangle F_{Lm}^{L'm'}(\theta, \phi), \quad (2.40)$$

where  $\delta$  is the  $E_2/M_1$  mixing ratio. For  $^{197}\text{Au}$ , the sum over  $L$  and  $L'$  runs over 1 and 2, corresponding to  $M_1$  and  $E_2$  radiation. In the case of iron,  $L$  and  $L'$  are equal to one.  $F_{Lm}^{L'm'}(\theta, \phi)$  contains the angular information and is given by

$$F_{Lm}^{L'm'}(\theta, \phi) = \sqrt{(2L+1)(2L'+1)} e^{-i\theta(m-m')} \sum_q d_{mq}^L(\theta) d_{m'q}^{L'}(\theta), \quad (2.41)$$

Equation 2.40 will be used to calculate the relative transition intensities when the absorber is a single crystal.

In the case of a randomly oriented powder, eq. 2.41 should be integrated over the angles  $\theta$  and  $\phi$ . As a result of the fact that rotation matrices are orthogonal [20], this results in  $8\pi^2 \delta_{LL'}$ . The probability for a transition from  $|a\rangle$  to  $|b\rangle$  to occur in a randomly oriented powder is then given by

$$P_{ab}(\vec{k}) \propto \sum_L \sum_{m_0} \sum_{m_1} \sum_{m'_0} \sum_{m'_1} C_{m_0}^{I_0^*} C_{m_1}^{I_1} C_{m'_0}^{I_0} C_{m'_1}^{I_1^*} \\ \delta^{2L-2} \langle I_1 m_1 | I_0 m_0 L m \rangle \langle I_1 m'_1 | I_0 m'_0 L m' \rangle. \quad (2.42)$$

Eq. 2.42 will be used to calculate the transition probabilities for randomly oriented samples.

## 2.5 Debye-Waller Factor

The Debye-Waller factor is the fraction of  $\gamma$ -ray absorptions or emissions that occur elastically, i.e. without loss of energy. The Debye-Waller factor is also referred to as the recoil-free fraction, Mössbauer fraction, or  $f$ -factor. It can be written as the thermal averaged probability that the state of the lattice,  $|L\rangle$ , is unchanged when a momentum transfer to an atom at position  $\vec{r}_j(t)$  takes place [4]

$$f = | \langle L | \exp(-i\vec{k} \cdot \vec{r}_j(t)) | L \rangle_T |^2, \quad (2.43)$$

where  $\vec{k}$  is the wave vector of the  $\gamma$ -ray. If we only consider the harmonic term of the potential to which the atoms of the lattice are subject, their displacement,  $\vec{x}_i(t)$ , from equilibrium position,  $\vec{r}_i$ , can be given by a linear combination of  $3N$  normal modes of vibration

$$\vec{x}_j(t) = \sum_{s=1}^{3N} A_s \vec{u}_s \exp(i\vec{q}_s \cdot \vec{r}_j - i\Omega_s t) + \sum_{s=1}^{3N} B_s \vec{u}_s \exp(i\vec{q}_s \cdot \vec{r}_j + i\Omega_s t), \quad (2.44)$$

where  $N$  is the number of atoms, and  $A_s$  and  $B_s$  are constants that depend on the initial conditions.  $\vec{u}_s$  and  $\Omega_s$  are the normalized polarization vector and energy of the normal modes of the lattice vibrations with wave vector  $\vec{q}_s$ . Time dependent quantities,  $a_s$ , and their complex conjugates,  $a_s^*$ , may be introduced, such that the energy of the lattice is given by

$$E_L = \sum_{s=1}^{3N} (a_s^* a_s + \frac{1}{2}) \hbar \Omega_s, \quad (2.45)$$

The atomic displacements are then given by

$$\vec{x}_j(t) = \sum_{s=1}^{3N} \frac{\hbar \vec{u}_s}{\sqrt{2mN\hbar\Omega_s}} \{a_s \exp(i\vec{q}_s \cdot \vec{r}_j) + a_s^* \exp(-i\vec{q}_s \cdot \vec{r}_j)\}, \quad (2.46)$$

where  $m$  is the mass of the atom.

Transforming eq. 2.45 and 2.46 into the quantum mechanical description,  $a_s^*$  and  $a_s$  are the raising and lowering operators of normal mode  $s$ . The state of the lattice is given by

$$|L\rangle = \prod_{s=1}^{3N} |n_s\rangle, \quad (2.47)$$

where  $|n_s\rangle$  are the orthonormalized wave functions of normal mode  $s$ , with occupation number  $n_s$ . If eq. 2.46 and 2.47 are substituted into eq. 2.43, the equilibrium position  $\vec{r}_i$  is chosen to be zero, and Planck's distribution function for the thermal average of the occupation number,  $n_s$ , is used, we obtain for the Debye-Waller factor [4]

$$f = \exp\left\{-\frac{1}{2mN} \sum_{s=1}^{3N} \frac{\hbar(\vec{k} \cdot \vec{u}_s)^2}{\Omega_s} \left(\frac{2}{\exp(\hbar\Omega_s/k_B T) - 1} + 1\right)\right\}. \quad (2.48)$$

Generally, the normal modes of vibration are unknown, and it is more convenient to describe the vibrations in terms of a phonon density,  $g(\Omega)$ . The summation in eq. 2.48 may then be replaced by an integral. If the vibrations are isotropic, the scalar product in eq. 2.48 between the wave vector and the normalized polarization vector of a phonon can be replaced by  $\frac{1}{3}\vec{k}^2$ , yielding

$$f = \exp\left\{-\frac{\hbar\vec{k}^2}{6mN} \int \frac{d\Omega g(\Omega)}{\Omega} \left(\frac{2}{\exp(\hbar\Omega/k_B T) - 1} + 1\right)\right\}, \quad (2.49)$$

where

$$\int_0^\infty g(\Omega) d\Omega = 3N. \quad (2.50)$$

In practice  $g(\Omega)$  can have a complicated form, and may be approximated by one of the following models. In the Einstein model, all atoms are assumed to vibrate with one characteristic frequency,  $\Omega_E$ . The phonon density is then given by

$$g_E(\Omega) = 3N\delta(\Omega - \Omega_E), \quad (2.51)$$

where  $\delta(x)$  is the Dirac  $\delta$ -function. For the Debye-Waller factor, one obtains

$$f_E = \exp\left\{-\frac{E_\gamma^2}{2mc^2} \frac{1}{\hbar\Omega_E} \left(\frac{2}{\exp(\hbar\Omega_E/k_B T)} + 1\right)\right\}, \quad (2.52)$$

where  $E_\gamma$  is the  $\gamma$ -ray energy. In the Debye model, the density of phonon states is quadratic in the energy up to a characteristic cut-off frequency  $\Omega_D$ ,

$$g_D(\Omega) = 9N \Omega^2 / \Omega_D^3, \quad 0 \leq \Omega \leq \Omega_D. \quad (2.53)$$

For frequencies higher than  $\Omega_D$ ,  $g_D(\Omega)$  is zero. The Debye-Waller factor is then given by

$$f_D = \exp\left\{-\frac{E_\gamma^2}{2mc^2} \frac{3}{2\hbar\Omega_D} \left(1 + \frac{4k_B^2 T^2}{\hbar^2 \Omega_D^2} \int_0^{\hbar\Omega_D/k_B T} \frac{x dx}{\exp(x) - 1}\right)\right\}. \quad (2.54)$$

## 2.6 Spectral Line Shape

When the energies and the relative intensities of the Mössbauer transitions are determined (see section 2.3 and 2.4 respectively), the spectral line shape can be evaluated. In section 2.6.1, we will describe the spectral line shape under the assumption that all hyperfine parameters are static. Subsequently, in section 2.6.2 the spectral line shape will be given for Mössbauer nuclei that are subject to a fluctuating hyperfine field.

### 2.6.1 Static Hyperfine Parameters

In the experiments described in this thesis, a transmission geometry is employed. Neglecting the resonant self-absorption in the source and assuming that only  $\gamma$ -rays of the Mössbauer transition are detected, the normalized transmission is given by [4]

$$F(v) = (1 - f_s) \exp(-n_t \bar{\sigma}) + f_s \int_{-\infty}^{\infty} I(v, \omega) D(\omega) d\omega, \quad (2.55)$$

where  $v$  and  $f_s$  are the Doppler velocity and the Debye-Waller factor of the source respectively. The first term of eq. 2.55 expresses the non-resonant (i.e. velocity independent) absorption of the off-resonant fraction of the  $\gamma$ -rays ( $1 - f_s$ ).  $n_t$  and  $\bar{\sigma}$  are the total number of atoms of the absorber per square cm and their average non-resonant cross section respectively. The second term describes the absorption of the resonant fraction of the  $\gamma$ -rays ( $f_s$ ). Since the detector does not discriminate the energy of the  $\gamma$ -rays, the absorption is integrated over the energy  $\omega$ . This integral is referred to as the transmission integral. The source part  $I(v, \omega)$  describes

energy distribution of the  $\gamma$ -rays. Assuming this to be Lorentzian (see eq. 2.3), the normalized intensity for a single line source can be given by

$$I(v, \omega) = \frac{\Gamma_s/2\pi}{(\omega - \omega_s + v)^2 + \Gamma_s^2/4}, \quad (2.56)$$

where  $\omega_s$  and  $\Gamma_s$  are the transition energy and linewidth at half maximum of the source respectively. The absorption part  $D(\omega)$  of the transmission integral (eq. 2.55) can be given by

$$D(\omega) = \exp\{-n_t \bar{\sigma} - n_r \sigma_r(\omega)\}, \quad (2.57)$$

where  $n_r$  is the number of atoms of the Mössbauer element per square cm and  $\sigma_r(\omega)$  is the resonant absorption cross section, which under the assumption of a Lorentzian absorption energy distribution is given by

$$\sigma_r(\omega) = \beta f_a \sigma_0 \frac{\Gamma_a^2/4}{(\omega - \omega_a)^2 + \Gamma_a^2/4}. \quad (2.58)$$

Here  $\beta$  is the abundance of the Mössbauer isotope,  $\sigma_0$  the maximal resonant absorption cross section (see table 2.1), and  $f_a$  is the Debye-Waller factor of the absorber.  $\omega_a$  and  $\Gamma_a$  are the absorption energy and linewidth at half maximum respectively.

When one inspects a spectrum, it is common practice to compare resonant absorption with the absorption at energies far from resonance  $F_\infty = \exp(-n_t \bar{\sigma})$ . Neglecting dispersion due to interference of  $E_2$  and  $M_1$  radiation, the relative transmission for a Mössbauer spectrum obtained with a single line source and a split absorber can be given by [22]

$$\frac{F(v)}{F_\infty} = 1 - f_s + f_s \int_{-\infty}^{\infty} d\omega \frac{\Gamma_s/2\pi}{(\omega - \omega_s + v)^2 + \Gamma_s^2/4} \sum_i W_i \exp\left\{-n_r \beta f_a \sigma_0 \frac{\Gamma_a^2/4}{(\omega - \omega_a^i)^2 + \Gamma_a^2/4}\right\}. \quad (2.59)$$

The summation extends over the absorption transitions  $i$ .  $W_i$  denotes the relative intensity of a transition with energy  $\omega_a^i$ , and is normalized,  $\sum_i W_i = 1$ .

In general, the transmission integral cannot be solved analytically. Therefore, in practice the integration is split up into three parts, I:  $-\infty < \omega < v_-$ , II:  $v_- < \omega < v_+$ , and III:  $v_+ < \omega < \infty$  [23]. Note that for convenience we define  $\omega = \omega - \omega_s$ . The energies  $v_-$  and  $v_+$  are chosen well below and above the absorption velocities  $v_a^i = (\omega_a^i - \omega_s)c/E_\gamma$ . Hence, on integrating parts I and III, the exponent in eq. 2.59 may be approximated by 1. The integrals for these parts become then solvable and one obtains

$$\int_{-\infty}^{v_-} d\omega I(\omega, v) = \frac{1}{2} + \frac{1}{\pi} \arctan \frac{2(v_- + v)}{\Gamma_s}. \quad (2.60)$$

A similar contribution is obtained from the integration of interval III. The integration over interval II is performed numerically, using the trapezium rule. The here sketched evaluation of the transmission integral was implemented in the program of Rübénbauer and Birchall [24], with which the spectra were analysed.

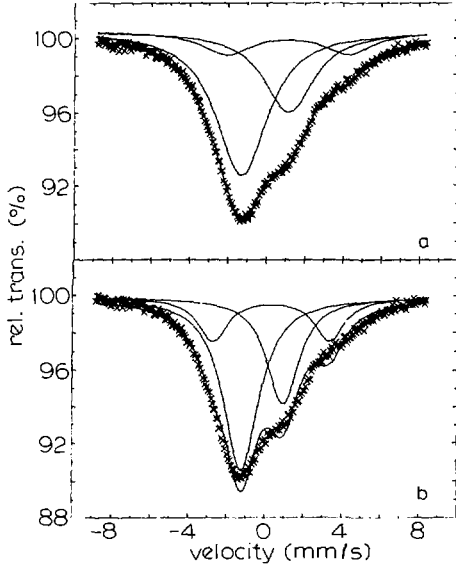


Figure 2.5: A fit of the  $^{197}\text{Au}$  spectrum at 4.2 K of  $\text{Au}_{55}(\text{PPh}_3)_{12}\text{Cl}_6$ , using two Lorentzian singlets and one Lorentzian doublet (a), and using the transmission integral method with the same number of resonance lines (b).

In the thin absorber limit, the exponent in the transmission integral may be approximated by a Taylor expansion up to the linear term. The analytical solution for the integral, which can be obtained using the residue theorem of the function theory [4], can be written as

$$\frac{F(v)}{F_\infty} = 1 - f_s + f_s \sum_i W_i n_r \beta f_a \sigma_0 \frac{(\Gamma_a + \Gamma_s)^2/4}{(v - v_a^i)^2 + (\Gamma_a + \Gamma_s)^2/4}. \quad (2.61)$$

Often when fitting Mössbauer spectra, the use of a number of Lorentzian lines will introduce little or no error. Necessary conditions are that the spectral lines being fitted are well separated and that one is using a relatively thin absorber.

However, when Mössbauer lines overlap, the use of the transmission integral for fitting becomes essential. This is shown in fig. 2.5a, where a 4.2 K spectrum of a Au cluster material, described later in this thesis, is fitted with only two singlets and one doublet using the Lorentzian approximation. In the Lorentzian approximation, the linewidth is an extra free parameter, that in cases like this creates such a freedom that only four Lorentzian lines are sufficient to fit the spectrum. A linewidth of 3.12 mm/s results from this fit, which should be compared to twice the natural linewidth, i.e. 1.87 mm/s appropriate for Au in the thin absorber limit. An exact calculation of the absorption profile can be done using the above transmission integral method. Then the linewidth is not a free parameter, but depends on the relative thickness of the absorber,  $\tau_a = n_r \beta f_a \sigma_0$ , and the natural linewidth. Fitting the spectrum, calculating the line shape by this method with the same number of resonance lines as in fig. 2.5a, shows how unrealistic the use of two singlets and one doublet actually is, see fig. 2.5b, and thus how drastically the Lorentzian approximation can lead to erroneous conclusions from an apparently excellent fit. The



transmission integral method, at the same time, guarantees that saturation effects, as well as the accompanying deviation from Lorentzian line shapes, are properly accounted for.

### 2.6.2 Fluctuating Hyperfine Field

The Mössbauer line shape in the presence of time-dependent hyperfine parameters has been described extensively in the literature. In some papers one starts from a Hamiltonian, which describes the entire system of nuclear and electronic spin system [25-28]. We will not follow this approach, since because of its complexity some of the hyperfine interactions have to be treated as perturbations. On the other hand, the fluctuations can be treated in a stochastic model [29-32]. The line shape can then be calculated for all possible fluctuation rates. We will only be interested in fluctuations of the hyperfine field in  $^{57}\text{Fe}$  M.E.S., and will assume the other hyperfine parameters to be static. The transitions between the nuclear levels will be assumed to have no influence on the electronic system, which means that an effective field approximation can be applied (see also the discussion in section 2.3.2). Moreover, we will be concerned with Ising-like systems in which the electronic spin is restricted to be along the easy axis. Consequently the hyperfine field will be either  $+H_{hj}$  or  $-H_{hj}$ . The spectral line shape in the case of spherical relaxation is described e.g. in refs. [33,34].

The rate of hyperfine field fluctuations,  $\Gamma_\omega$ , that influence the Mössbauer spectrum for  $^{57}\text{Fe}$  are found in the frequency range given by

$$\Delta\Gamma < \Gamma_\omega < \delta_0^2/\Delta\Gamma. \quad (2.62)$$

The frequency boundaries of the Mössbauer window are determined by the experimental resolution, i.e. the smallest observable line broadening,  $\Delta\Gamma$ , which is of the order of 0.01 mm/s for  $^{57}\text{Fe}$  M.E.S. The upper boundary is also determined by the energy difference,  $2\delta_0$ , of the two states that are coupled by the fluctuating hyperfine field. These two states are represented by  $|aI_0m_0I_1m_1\rangle$ , where  $a$  represents the sign of the hyperfine field,  $a = \pm 1$ . Note that for each transition,  $|I_0m_0I_1m_1\rangle$ , a separate  $\delta_0$  can be defined, and that  $\delta_0$  in the Mössbauer effect takes the same place as the nuclear Larmor frequency,  $\omega_L$ , in N.M.R. theory. For ferrous compounds with a hyperfine field of the order of 10 T, the frequency window is  $10^5$  to  $10^9$  Hz, whereas for ferric compounds with a hyperfine field of  $\sim 50$  T, the window can be as large as  $10^5$  to  $10^{11}$  Hz. For fluctuation frequencies below this window, the hyperfine field appears to be static in the Mössbauer spectrum. Above this window, the thermally averaged value of the hyperfine field is observed.

The time-dependent Hamiltonian for the Mössbauer nucleus can be given by

$$\mathcal{H}(t) = \sum_j V_j f_j(t), \quad (2.63)$$

where  $f_j(t)$  is a stochastic function that jumps between  $n$  different values, corresponding to  $n$  different ways in which the Hamiltonian can be constructed, and

$V_j$  stands for the different operators. We will be interested in the case where  $V_1$  is the static Q.S. and applied magnetic field term (eq. 2.34), with  $f_1(t) = 1$ , and where  $V_2$  is the fluctuating internal hyperfine field due to the electrons, with  $f_2(t)$  stochastically jumping between the values  $\pm 1$ .

In some cases, e.g. when the total hyperfine field in each of the  $n$  different ways in which the Hamiltonian can be constructed is parallel to the main axis of the E.F.G., the Hamiltonian of eq. 2.63 commutes with itself at different times. These cases will be referred to as adiabatic relaxation, since the time variation of  $\mathcal{H}(t)$  does not cause transitions between the eigenstates of  $\mathcal{H}$ , but only changes the energies of the eigenstates. The two transitions that are coupled by the fluctuating hyperfine field,  $|aI_0m_0I_1m_1\rangle$  with  $a = \pm 1$ , can then be described separately, which makes the description of the spectral line shape relatively simple. An analytical formula can be found in refs. [31,32].

We will now discuss some characteristic features of Mössbauer spectra that reflect an adiabatic relaxation of the hyperfine field. For convenience, we assume the transition probabilities for  $f(t)$  to be equal and the applied magnetic field to be zero. Then in the slow relaxation regime ( $\Gamma_\omega < \delta_0$ ), to first order the spectrum is affected by an equal broadening of the linewidths of all transitions by  $2\Gamma_\omega$ . To second order, the splitting,  $\delta$ , of the two transitions that are coupled by the fluctuating hyperfine field decreases as [35]

$$\delta = \delta_0 - \frac{\Gamma_\omega^2}{2\delta_0}. \quad (2.64)$$

In the fast relaxation regime, the two transitions will coincide at their thermal average. The corresponding excess linewidth,  $\Delta\Gamma$ , is given by  $\delta^2/\Gamma_\omega$ . For the entire Mössbauer frequency window the excess linewidth can be summarized in the equation

$$\Delta\Gamma = \frac{\delta_0^2\Gamma_\omega}{\Gamma_\omega^2 + \frac{1}{2}\delta_0^2}, \quad (2.65)$$

where one should keep in mind that if  $\Gamma_\omega \approx \delta_0$ , the line shape deviates from being Lorentzian.

However, in general the Hamiltonian of eq. 2.63 will not commute with itself at different times. This is e.g. the case when the hyperfine field is not parallel to the main axis of the E.F.G., or when an arbitrary angle exists between the static applied magnetic field and the fluctuating hyperfine field due to the electrons. The fluctuations not only change the energy of the eigenstates, but also cause transitions between them. This non-adiabatic effect causes an anomaly which is referred to as the Blume asymmetry [29]. The Blume asymmetry is observed for a nucleus which is subject to a static quadrupole splitting and a fast fluctuating hyperfine field. In this fast fluctuation regime, one of the spectral lines of the doublet is broadened more than the other. In contrast to the adiabatic case, where the nuclear Zeeman term broadens the Mössbauer line with  $m_1 = \pm \frac{3}{2}$  most, non-adiabatic relaxation causes the line with  $m_1 = \pm \frac{1}{2}$  to be broadened most. It may be clear that the spectral line shape can no longer be described in terms of a summation of doublets. The entire spectrum should be evaluated as a whole. A very transparent derivation

is given by Blume and Tjon [29,30], which we will not reproduce here. The resulting spectral line shape  $F(\nu)$  is given in matrix form of order  $(2I_1 + 1)(2I_0 + 1)n$ , where  $n$  is the number of possible values for the stochastic function  $f(t)$  in eq. 2.63,

$$F(\nu) = \frac{1}{2I_1 + 1} \sum_{m_1 m_0 m'_1 m'_0} \langle I_1 m_1 | I_0 m_0 L m \rangle \langle I_1 m'_1 | I_0 m'_0 L m' \rangle F_{Lm}^{Lm'}(\theta, \phi)$$

$$\sum_{ab} p_a \langle I_0 m_0 I_1 m_1 a | [pI - W - i \sum_j V_j^\times F_j]^{-1} | I_0 m'_0 I_1 m'_1 b \rangle. \quad (2.66)$$

The first three factors after the summation sign are concerned with the transition probabilities, and can be found in section 2.4. For  $^{57}\text{Fe}$ , only magnetic dipole radiation has to be considered ( $L = 1$ ). The last factor in eq. 2.66 is the actual interaction matrix, where  $p = \Gamma/2 - i\nu$ , and  $\Gamma$  is the sum of the source and absorber linewidth.  $I$  represents the unit matrix.  $V_j^\times$  is the Liouville operator associated with the operator  $V_j$  (see eq. 2.63), and can be calculated from eq. 2.34, using the property of Liouville operators that

$$\langle I_0 m_0 I_1 m_1 | V_j^\times | I_0 m'_0 I_1 m'_1 \rangle = \delta_{m_1 m'_1} \langle I_0 m_0 | V_j | I_0 m'_0 \rangle - \delta_{m_0 m'_0} \langle I_1 m_1 | V_j | I_1 m'_1 \rangle. \quad (2.67)$$

$F_j$  in eq. 2.66 is a diagonal matrix with the possible values for  $f_j(t)$  on its diagonal. The physical information resides in the matrix  $W$ . Its off-diagonal elements,  $\langle a | W | b \rangle$ , are the transition probabilities that  $f(t)$  jumps from  $a$  to  $b$ . The diagonal elements, given by

$$\langle a | W | a \rangle = - \sum_{b(\neq a)} \langle a | W | b \rangle, \quad (2.68)$$

are equal to the negatives of the inverse lifetime of  $f(t)$  with value  $a$ . Equation 2.66 only holds for processes in equilibrium. The a priori probabilities,  $p_a$ , of a specific value,  $a$ , of  $f(t)$  to occur, are defined by the condition for detailed balance

$$p_a \langle a | W | b \rangle = p_b \langle b | W | a \rangle, \quad (2.69)$$

and from the normalization of  $p_a$ ,  $\sum_a p_a = 1$ .

It is obvious that in the case of paramagnetic relaxation without an external magnetic field, the a priori probabilities are equal for finding the hyperfine field up or down. One can, however, expect that for e.g. ferromagnets with a spontaneous electronic moment, these a priori probabilities are unequal.

Shenoy et al. [36] have rewritten eq. 2.66 into

$$F(\nu) = \text{Re} \sum_j \frac{\sum_{kl} V_{jk}^{-1} A_{kl} V_{lj}}{\Omega_j - i\nu}. \quad (2.70)$$

The indices  $j$ ,  $k$ , and  $l$  run from 1 to  $(2I_1 + 1)(2I_0 + 1)n$  and are composed of the indices for the nuclear spin quantum numbers,  $m_0$  and  $m_1$ , and the stochastic index

a.  $\Omega_j$  denotes the eigenvalues, and  $V$  is the matrix composed of the eigenvectors of the interaction matrix described by the last factor in eq. 2.66, with  $p$  replaced by  $\Gamma/2$ . The matrix elements  $A_{\mathbf{M}}$  can be calculated by (section 2.4)

$$A_{m_0 m_1 a m'_0 m'_1 b} = p_a \langle I_1 m_1 | I_0 m_0 L m \rangle \langle I_1 m'_1 | I_0 m'_0 L m' \rangle F_{L m}^{L m'}(\theta, \phi). \quad (2.71)$$

The advantage of eq. 2.70 is that the eigenvalues and vectors of the interaction matrix need to be evaluated only once for a spectrum instead of for each data point.

The hyperfine field fluctuations in the Blume and Tjon model are assumed to occur stochastically, i.e. randomly in time or irrespective of the history. Hence, the time correlation of the hyperfine field, on which this model is based, is given by

$$\langle H_{hf}(t) H_{hf}(0) \rangle \propto \exp(-\Gamma_\omega t), \quad (2.72)$$

where  $\Gamma_\omega$  is the fluctuation rate, which is equal to  $2p_a \langle a | W^{-1} | b \rangle$ . Under the assumption that the fluctuating hyperfine field is the local field originating from the electrons of the Mössbauer atom itself, the hyperfine field in eq. 2.72 can be replaced by the electronic spin, yielding the spin autocorrelation function,  $\langle S^x(t) S^x(0) \rangle$ , which is the physical quantity we will be investigating in chapter 4.

## References

- [1] R.L. Mössbauer, *Z. Physik* 151 (1958) 124 & *Z. Naturforsch.* 14 (1959) 211.
- [2] H.J. Lipkin, *Ann. Phys.* 9 (1960) 332.
- [3] N.N. Greenwood and T.C. Gibb, "Mössbauer Spectroscopy", London (1971).
- [4] H. Wegener, "Der Mössbauer Effect und seine Anwendung in Physik und Chemie", Mannheim (1965).
- [5] V.I. Goldanskii and R.H. Herber, eds. "Chemical Applications of Mössbauer Spectroscopy", New York (1968).
- [6] U. Gonser, ed. "Mössbauer Spectroscopy", Topics in Applied Physics, Vol. 5, Springer-Verlag, Berlin (1975).
- [7] P. Gütlich, R. Link, and A. Trautwein, eds. "Mössbauer Spectroscopy and Transition Metal Chemistry", Springer-Verlag, Berlin (1978).
- [8] D.A. Shirley, *Rev. Mod. Phys.* 36 (1964) 339.
- [9] G.K. Shenoy and F.E. Wagner, eds. "Mössbauer Isomer Shifts", North Holl. Publ. Comp., A'dam (1978).
- [10] J. Sivadriere, M. Blume, and M.J. Clouser, *Hyp. Int.* 1 (1975) 227.
- [11] A. Abragam, "The Principles of Nuclear Magnetism", Oxford University Press (1961).
- [12] K.W.H. Stevens, *Proc. Phys. Soc. (London)* A65 (1952) 209.
- [13] M.T. Hutchins, *Sol. St. Phys.* 16 (1964) 227.
- [14] A. Vermaas, W.L. Groeneveld, and J. Reedijk, *Z. Naturforsch.* 32A (1977) 1393.
- [15] R. Ingalls, *Phys. Rev.* 133 (1964) A787.
- [16] J.T. Schriempf and S.A. Friedberg, *Phys. Rev.* 136 (1964) A518.
- [17] W. Kündig, *Nucl. Instr. and Meth.* 48 (1967) 219.
- [18] H. Spiering, *Hyp. Int.* 3 (1977) 213.
- [19] J. van Dongen Torman, R. Jagannathan, and J.M. Trooster, *Hyp. Int.* 1 (1975) 135.
- [20] M. Brink and G.R. Satchler, "Angular Momentum", Oxford University Press (1962).
- [21] H. Prosser, F.E. Wagner, G. Wortmann, G.M. Kalvius, and R. Wäppling, *Hyp. Int.* 1 (1975) 25.
- [22] S. Margulies, P. Debrunner, and H. Frauenfelder, *Nucl. Instr. and Meth.* 21 (1963) 217.
- [23] M.P.A. Vieggers, PhD Thesis, Katholieke Universiteit te Nijmegen (1976).
- [24] K. Rübénbauer and T. Birchall, *Hyp. Int.* 7 (1979) 125.
- [25] A.M. Afanasev and Yu. Kagan, *Sov. Phys. JETP* 18 (1964) 1139.
- [26] Yu. Kagan and A.M. Afanasev, *Sov. Phys. JETP* 20 (1965) 743.
- [27] H. Wegener, *Z. Physik* 186 (1965) 498.
- [28] E. Bradford and W. Marshall, *Proc. Phys. Soc. (London)* 87 (1966) 731.
- [29] M. Blume and J.A. Tjon, *Phys. Rev.* 165 (1968) 446.
- [30] M. Blume, *Phys. Rev.* 174 (1968) 351.
- [31] F. van der Woude and A.J. Dekker, *Phys. Stat. Sol.* 9 (1965) 977.
- [32] H.H. Wickman, M.P. Klein, and D.A. Shirley, *Phys. Rev.* 152 (1966) 345.
- [33] F.J. Litterst, J.M. Friedt, J.L. Tholence, and F. Holtsberg, *J. Phys. C* 15 (1982) 1049.
- [34] F. Hartmann-Boutron, *Ann. Phys.* 9 (1975) 285.
- [35] M.J. Clouser, *Phys. Rev. B* 3 (1971) 3748.
- [36] G.K. Shenoy and B.D. Dvalap, in *Proc. of the Int. Conf. on Mössb. Spectr.*, Cracow, Poland (1975).
- [37] E.U. Condon and G.H. Shortley, "The Theory of Atomic spectra", Cambridge (1964).

## 3 Experimental Arrangements

### 3.1 Introduction

For the  $^{57}\text{Fe}$  Mössbauer measurements a cryostat was required that could be operated at temperatures down to well below 1 K with the possibility to apply an external magnetic field. The special  $^{197}\text{Au}$  Mössbauer experiments, for which both absorber and source must be cooled to maintain a reasonable recoilfree fraction, and for which it must be possible to change absorber on a frequent basis, were planned to be performed in the same cryostat. To meet these requirements, an existing  $^4\text{He}$  bath cryostat that has been described extensively in ref. [1] has been modified. A superconducting magnet with a maximum field of 7.5 T has been installed. A continuously circulating  $^3\text{He}$  refrigerator has been implemented, and a quick exchange of samples has been made possible by the use of a drawer system as designed by the Mössbauer group of the Katholieke Universiteit te Nijmegen [2]. A description of the modified cryostat and insert can be found in section 3.2. Most components of the Mössbauer setup have been bought commercially. The setup will be described briefly in section 3.3. Some words will be spent on the preparation of the sources and absorbers in section 3.4. Especially the treatment of single crystals in order to obtain well oriented platelets with a thickness of the order of 0.1 mm will be discussed. In section 3.5 we will present the method by which we have determined the absolute recoilfree fractions in the  $^{197}\text{Au}$  measurements.

### 3.2 Cryostat

A schematic representation of the cryostat is shown in fig. 3.1. The vertical geometry employed is most convenient if source and absorber must be cooled. Moreover, this geometry made it possible to build in a superconducting solenoid with compensation area for the source. The cryostat consists of a stainless steel cylinder that holds the general vacuum. Two concentric cylinders make up the liquid nitrogen reservoir (2, the numbers between brackets refer to fig. 3.1). Copper radiation shields (4) are thermally linked to the top and bottom of the nitrogen tank. The  $^4\text{He}$  tank (3) is sealed with an indium o-ring to a stainless steel flange (11). The tubing between the  $^4\text{He}$  container and the top flange at room temperature is made of kapton foil wrapped and glued with stycast [3]. Kapton tubes have the advantage of being readily available in all desired dimensions and have a small thermal conductivity. Since helium gas diffuses slowly through these tubes at room temperature, containers with activated charcoal (10) have been attached to the bottom of the  $^4\text{He}$  tank. These maintain the pressure of the general vacuum below  $1.0 \cdot 10^{-6}$  torr. The kapton tubes were glued to brass flanges that could be sealed with indium o-rings to both stainless steel flanges. The best metal-plastic tube joint was obtained by Deltabond 151. The windows (21) that are transparent for Mössbauer radiation are made of aluminium foil, which is obtained by press rolling a button of very pure aluminium to a thickness of about 20  $\mu\text{m}$ . Household aluminium foil contains

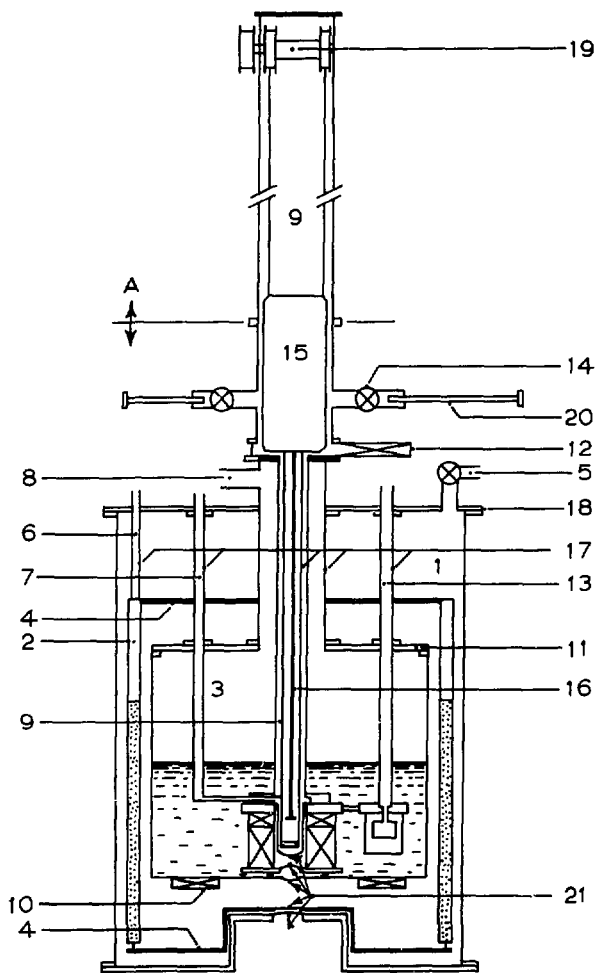


Figure 3.1: Schematic drawing of the cryostat.

- |                              |                           |                                      |
|------------------------------|---------------------------|--------------------------------------|
| 1. general vacuum            | 9. exchange gas space     | 15. transducer, laser, and Michelson |
| 2. LN <sub>2</sub> tank      | 10. charcoal pump         | 16. transducer rod                   |
| 3. LHe tank                  | 11. top flange of He tank | 17. kapton tubes                     |
| 4. radiation shield          | 12. gate valve            | 18. top flange                       |
| 5. outlet to vac. pump       | 13. pump tube of 1 K pot  | 19. hoisting system                  |
| 6. LN <sub>2</sub> fill tube | 14. transfer valve        | 20. transfer rod                     |
| 7. <sup>3</sup> He pump tube |                           | 21. kapton windows                   |
| 8. <sup>4</sup> He exhaust   |                           |                                      |

too much iron and disturbs  $^{57}\text{Fe}$  experiments if the iron content in the sample is low. The aluminium foil is sandwiched between two layers of kapton with teflon coating. After a heat treatment at  $300\text{ }^\circ\text{C}$  in order to melt the teflon coating, a strong window is obtained with a negligible helium diffusivity.

In operation, the transducer (15) and the tail which accommodates the source and absorber can be hoisted up. In the upward position the absorber is at the level of the transfer rod (20). A large gate valve (12) can then be closed, making it possible to open the top part (A) of the cryostat. However, during a  $^{197}\text{Au}$  experiment (for  $^{197}\text{Au}$   $t_{1/2} = 18\text{ h}$ ) heating the absorber block up to room temperature, replacing the absorber, pumping the top part of the cryostat vacuum and cooling the absorber block to helium temperatures takes far too much time (approximately two and a half hours). The present drawer system makes it possible to replace the drawer that contains the absorber by a transfer rod (20), while the absorber block is kept fixed by another similar rod. The transfer valve (14) prevents any air or water freezing down onto the absorber block while the absorber is exchanged outside the cryostat. The whole operation of which the cooling down to helium temperatures takes the longest time, can easily be done within half an hour.

A commercially bought superconducting magnet with a maximum field of  $7.5\text{ T}$  and a bore of  $41.0\text{ mm}$  is built into the cryostat. In view of the duration of a typical M.E.S. experiment, it was a necessary condition that the magnet could be operated in the persistent mode. A field inhomogeneity of  $10^{-2}$  over the sample space is acceptable for  $^{57}\text{Fe}$  Mössbauer experiments, since such an inhomogeneity causes a line broadening of  $0.01\text{ mm/s}$  at maximum field, which should be compared to a linewidth of  $0.25\text{ mm/s}$  as commonly observed. In the case of other Mössbauer isotopes, the situation is even more favourable. On top of the solenoid a compensation coil is placed, such that at  $67\text{ mm}$  from the maximum field the magnetic field is completely cancelled. The Mössbauer source is positioned in this compensated field area, preventing the single line being split up by the nuclear Zeeman interaction. Since the transducer, that provides for the Doppler shift of the  $\gamma$ -ray energy, is situated far from the superconducting solenoid, stray fields do not disturb the precisely controlled movement of the source. The current leads of the magnet that form the electrical connection between solenoid and electrical feed throughs near the top flange of the cryostat are made of brass wire-netting. In parallel with this, a superconducting multi-filament wire is soldered that carries the current as long as its temperature is below the superconducting transition temperature. The current leads are force-cooled by a tube that encircles the leads over their full length. The heat that is transferred to the  $^4\text{He}$  bath via the current leads boils off helium which is thus forced to find its way to the helium exhaust in close thermal contact with the wire-netting. The field homogeneity and distance between maximum field and compensation area was checked by means of a Hall probe. An absolute calibration of the field turned out to be best performed by a Mössbauer measurement. In this way most systematic errors are avoided. The diamagnetic compound  $\text{K}_4\text{Fe}(\text{CN})_6 \cdot 3\text{H}_2\text{O}$  is a good calibration candidate, since the field experienced by the nucleus of this diamagnetic insulating iron sample is equal



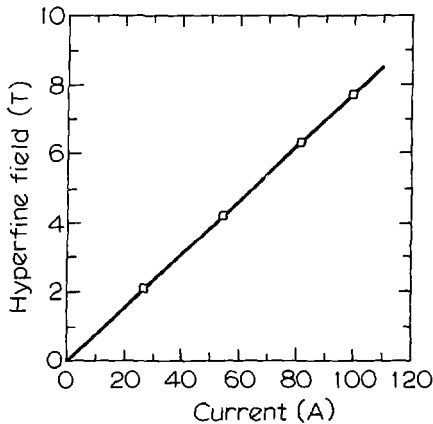


Figure 3.2: Field calibration of the superconducting magnet by means of the hyperfine field of  $\text{K}_4\text{Fe}(\text{CN})_6 \cdot 3\text{H}_2\text{O}$ .

to the applied field. Moreover, this compound has the advantage of a very large recoilfree fraction and of a zero quadrupole splitting such that a single crystal is not required. A plot of the observed field versus the magnet current can be found in fig. 3.2. The calibration yields  $12.88(\pm 0.01)$  A/T.

In order to perform Mössbauer measurements well below 1 K, a  $^3\text{He}$  continuous circulation refrigerator has been designed and built. A schematic drawing can be found in fig. 3.3. Since we did not want to depart from the above described sample handling system and since the bore of the magnet presents a limiting condition, we chose for the following geometry. The bottom part of the exchange gas space (1, the numbers from here onwards refer to fig. 3.3) is used as  $^3\text{He}$  pot, where the absorber block (2) is in direct contact with the liquid. A separate  $^3\text{He}$  pump tube (3) was installed, since the transducer and the tail left too little space for the required pumping speed. A high vacuum (4) provides for the thermal insulation of the  $^3\text{He}$  pot. Because of the limiting size of the magnet bore, the supporting frame of the magnet (5) itself was used as a vacuum can. The aluminium frame is held between two stainless steel flanges (6) kept together by rods (7). Between the flanges and the frame indium o-rings provide a vacuum seal. In order to prevent a difference in thermal expansion the rods have been made of aluminium.

At the high pressure side of the refrigerator, the  $^3\text{He}$  gas enters the cryostat via a capillary. The capillary (8) is thermally linked to the liquid nitrogen radiation shield before it enters the helium reservoir. The  $^3\text{He}$  is cooled from 4.2 to 1 K and condensed by the 1 K pot (9). Finally, the high and low pressure side of the  $^3\text{He}$  circulation system are connected by a flow impedance (10). The  $^4\text{He}$  bath supplies the 1 K pot with  $^4\text{He}$  via an amorphous brass filter (11). A flow impedance (12) determines the flow rate and consequently the cooling power of the 1 K pot. Note that for the above mentioned reasons, the  $^3\text{He}$  pump tube is not thermally anchored to the 1 K pot. This is usually the case, since it has the advantage of reducing the heat input of the  $^3\text{He}$  bath. Moreover, condensation of the  $^3\text{He}$  will occur if it is inserted via the pump tube.

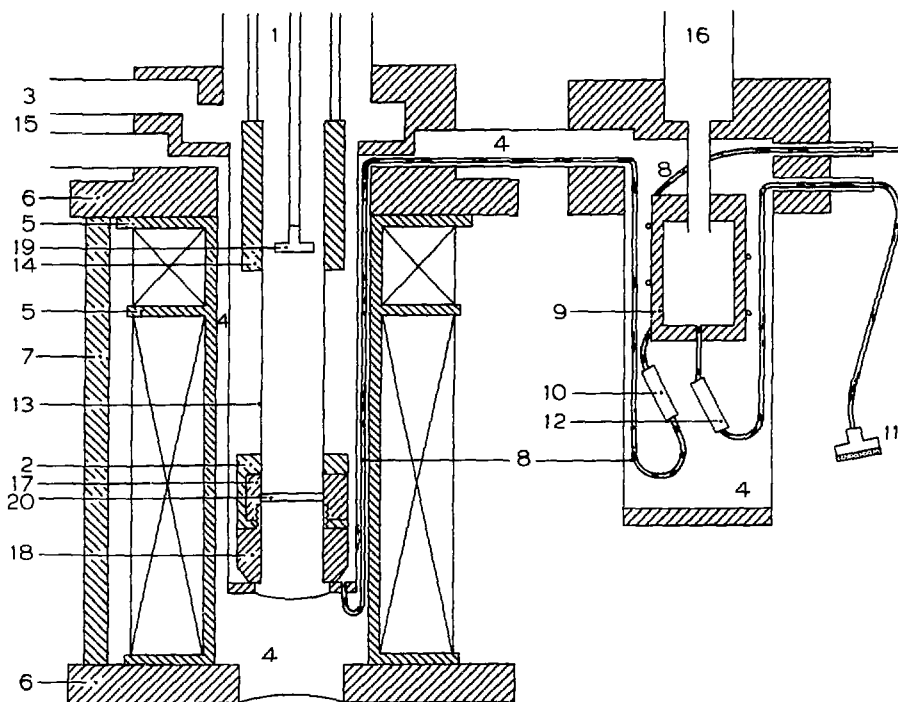


Figure 3.3: Schematic drawing of the  $^3\text{He}$  refrigerator.

- |                            |                                  |                             |
|----------------------------|----------------------------------|-----------------------------|
| 1. exchange gas space      | 9. 1 K pot                       | 15. high vacuum pump tube   |
| 2. absorber block          | 10. $^3\text{He}$ flow impedance | 16. $^4\text{He}$ pump tube |
| 3. $^3\text{He}$ pump tube | 11. $^4\text{He}$ filter         | 17. absorber drawer         |
| 4. high vacuum             | 12. $^4\text{He}$ flow impedance | 18. ring for heat exchange  |
| 5. magnet frame            | 13. kapton absorber support      | 19. source                  |
| 6. stainless steel flanges | 14. source shield                |                             |
| 7. support rods            |                                  |                             |
| 8. $^3\text{He}$ capillary |                                  |                             |

The heat balance of the system has been calculated. Several terms are responsible for the heat input of the  $^3\text{He}$  system. The radiation of the  $\gamma$ -rays and radiation from the surrounding which is at 4.2 K onto the  $^3\text{He}$  bath can be neglected. The temperature of the  $^3\text{He}$  pot is chosen to be at 0.5 K for the present estimations of the heat input. The absorber block is connected to the tail by a 5 cm long kapton tube (13). Since the heat conductivity of kapton is unknown, an average of the results found for other plastics is taken [4]. This yields an heat input of 0.028 mW. The heat dissipated in the  $^3\text{He}$  gas due to its viscosity can be neglected. Furthermore, the heat conductivity of the gas and the perceptible heat of the gas are of the same order of magnitude and will cancel one another. The electrical connections of the heater and the thermometers on the absorber block are made of manganine wire which has a negligible heat conductivity. The heat input will be mainly due to the thin wall of the stainless steel pump tube (0.25 mm). The thermal gradient in the pump tube is built up over the 5 cm between the absorber block and the source shield (14). This heat leak amounts to 0.33 mW. The total heat input evaporates 15  $\mu\text{mole}$   $^3\text{He}$  per second at a temperature of 0.5 K. The temperature dependent latent heat of  $^3\text{He}$  and other valuable relations can be found in ref. [5]. The evaporation rate is estimated to be roughly 10 % higher than calculated, since the continuously supplied  $^3\text{He}$  liquid from the 1 K pot has to be cooled.

Now that the mass flow of the  $^3\text{He}$  is known, it is possible to calculate the pressure drop over the pump tubes. The pressure drop can be calculated from Knudsen's relation appropriate for the molecular flow and from Poiseuille's relation in the case of viscous flow [5]. The molecular and viscous flow in  $\mu\text{moles/s}$  can respectively be given by

$$\dot{n}_M = \frac{\Delta P \rho D^3 T^{\frac{1}{2}}}{1.36 \cdot 10^{-6} P \ell}, \quad (3.1)$$

$$\dot{n}_V = \frac{\Delta P \rho D^4}{9.3 \cdot 10^{-9} \eta \ell}, \quad (3.2)$$

where  $P$  and  $\Delta P$  are the pressure and pressure difference in torr,  $D$  and  $\ell$  are the diameter and length of the tubes in cm,  $\eta$  is the viscosity in  $\mu\text{poise}$ , and  $\rho$  is the density in  $\text{g/dm}^3$ . The total mass flow is assumed to be the summation of viscous and molecular flow. Since the pressure drop over a pump tube with a certain temperature gradient depends on pressure and temperature, the pressure is numerically integrated. In practice the diameters of the pump tubes at different temperatures could be chosen in such a way that the total pressure drop from  $^3\text{He}$  bath to pump inlet only amounts to a few percent. The lowest attainable temperature using a pump that has a pumping speed of 4  $\text{dm}^3/\text{s}$ , can be calculated to be 0.45 K.

We have also calculated the heat balance for the 1 K pot. The radiation from the surrounding at 4.2 K onto the 1 K pot has been neglected. For the same reasons as mentioned above, we have discarded the heat conductivity and the perceptible heat of the gas. The heat input due to heat conductivity of the pump tube is estimated to be 0.33 mW. The cooling power necessary to condense and to cool down the  $^3\text{He}$  to 1 K with a rate of 15  $\mu\text{mole/s}$  is equal to 1.2 mW. The total cooling power of the

1 K pot was chosen to be roughly twice as large as the sum of these two terms, since if the  $^3\text{He}$  system is operated at temperatures between 0.6 and 4.2 K, the circulation rate of the  $^3\text{He}$  will be higher and consequently the necessary cooling power of the 1 K pot as well. The total mass flow of the  $^4\text{He}$  should again be twice as high as is calculated from the cooling power, since the  $^4\text{He}$  itself should be cooled from 4.2 to 1.2 K. With a latent heat of 90 J/mole, this yields a mass flow of 70  $\mu\text{mole/s}$ .

The flow impedances have been designed after ref. [6]. They have been constructed from a brass cylinder with a length in the order of 1 cm and an inner diameter of several mm. Both ends fit into a top into which the capillary was soldered. The cylinder was filled with closely packed  $\text{Al}_2\text{O}_3$  powder, with a average particle diameter of 0.05  $\mu\text{m}$ . At both ends a platelet of amorphous brass prevents the powder from blocking the capillaries. The advantage of these impedances with respect to wire-in-capillary impedances is that the risk of getting blocked is much smaller. Moreover, their flow rate is much more predictable.

Since it takes quite some time to build in the flow impedances inside the cryostat and test their performance, they were tested with  $^4\text{He}$  gas at room temperature and at liquid nitrogen temperature. Assuming that small channels with the diameter of the powder particles are responsible for the flow, eq. 3.1 and 3.2 can be used to scale the test flows to the operational flow. The input pressures used for the flow test were chosen in such a way that the rate of viscous and molecular flow is comparable to that for the operational circumstances. After being assembled, both impedances showed the predicted flow and did not have to be replaced.

The lowest temperature the  $^3\text{He}$  circulation system reaches in operation is 0.50 K. This temperature is measured by an Allan & Bradley carbon thermometer placed at the bottom of the  $^3\text{He}$  pot and by the  $^3\text{He}$  gas pressure. The total mass flow in the  $^3\text{He}$  system can now experimentally be determined from this pressure and the pumping speed of the pump, and was found to amount to 21  $\mu\text{mole/s}$ . The corresponding heat input is equal to 0.69 mW. The agreement with the estimated heat input is within a factor of two, which is good enough in view of the crudity of the estimations. The lowest temperature of the absorber block is 610 mK. In order to minimize the temperature difference between  $^3\text{He}$  bath and absorber block several actions were undertaken. The standard brass drawer that contains the absorber was replaced by a copper one (17). The latter was supplied with a fine screw thread, such that an additional copper ring (18) could be screwed in from the bottom of the absorber block. The copper ring is in direct contact with the  $^3\text{He}$  liquid. Moreover, this ring is provided with holes filled with fine silver powder sinter. In this way the contact area between the liquid and the absorber block was enhanced and the Kapitza resistance decreased. We think that the temperature difference of the  $^3\text{He}$  liquid and the absorber block is a result of the large heat leak of the stainless steel pump tube. This heat is transferred to the top of the absorber block. Since the thermal contact between the absorber block and the liquid is not optimal, a temperature difference results. An easy way to overcome this problem is to make the bottom part of the  $^3\text{He}$  pot and the lowest part of the pump tube up to the top of the absorber block of copper. Then the heat entering via the pump

tube is no longer transferred to the absorber block. The thermal contact through the gas and between the liquid and the absorber block should then be sufficient to reduce the temperature difference. The lowest temperatures reached, however, were sufficient for the planned experiments. In order to perform measurements at temperatures above 0.6 K, a heater was provided on the absorber block. A power dissipated in the heater up to roughly 10 mW turned out to be sufficient to stabilize any required temperature between 0.6 and 4.2 K. In addition, temperatures between liquid helium and room temperature could be established by evacuating the exchange gas space.

A thermometer as well as a heater wire were attached to the 1 K pot, in order to determine the cooling power of the 1 K pot. The lowest temperature reached by the 1 K pot is 1.1 K. The maximum power was experimentally determined to be 3.0 mW. This result is in good agreement with the specifications of the design.

The temperature measurement of the absorber was carried out with a four point a.c. bridge, designed and built by the electronic department of our laboratory. The off-balance voltage of the bridge serves as an input for a proportional and integration circuit, that regulates the heater current. Four resistance thermometers have been installed on the absorber block, namely a platinum thermometer for temperatures between 293 K and 90 K, a glass-carbon thermometer between 1.25 and 90 K, and a germanium thermometer for temperatures below 1.25 K, the latter two have been calibrated in our laboratory [7]. For measurements in an applied field the glass-carbon thermometer or an Allan & Bradley carbon thermometer could be used, since the influence of a magnetic field can be corrected for [8,9]. The measurement stability over 24 hours, its reproducibility, and accuracy between 0.6 and 4.2 K are better than 5 mK. Between 4.2 K and room temperature the temperature determination and controlling is better than 1 %.

In conclusion it may be stated that the here described  $^3\text{He}$  cryostat meets the requirements mentioned in section 3.1. It is in operation since summer 1987. Unfortunately, a planned study on the planar antiferromagnetic chain system TMMC ( $(\text{CH}_3)_4\text{NMnCl}_3$ ) could not be performed due to preparative problems concerning the substitution of a small fraction of the Mn ions by  $^{57}\text{Fe}$ . However, a study on a with  $^{57}\text{Fe}$  substituted high  $T_c$  ceramic superconductor  $\text{YBa}_2\text{Cu}_3\text{O}_{7-\delta}$ , could be extended to 0.6 K, which gave additional information on the slow relaxation behaviour observed in the  $^{57}\text{Fe}$  Mössbauer spectra [10]. In fig. 3.4 we show two Mössbauer spectra of  $\text{FeClBiPy}_3$ , measured at 0.6 K with and without an applied field. These data made it possible to determine the magnetic anisotropy well below the three-dimensional ordering temperature by determining the intensities of absorption lines 2 and 5 as a function of applied field. Moreover, conclusive information could be obtained on the mechanism that causes the line broadening at temperatures below 4.0 K [11].

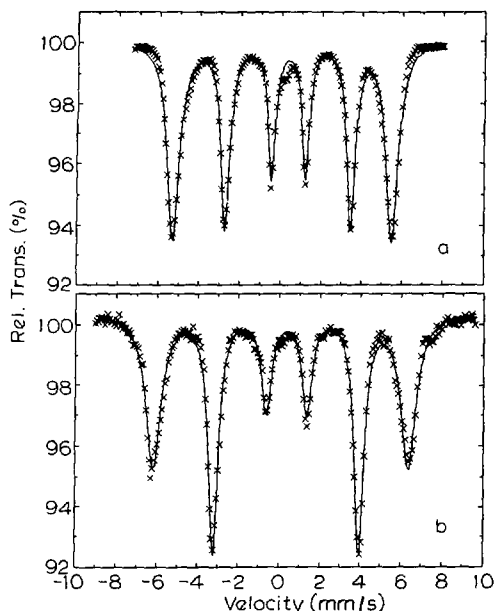


Figure 3.4: Illustrative spectra of  $\text{FeBiPyCl}_3$  taken 610 mK a) without an applied field and b) in a field of 7.5 T.

### 3.3 Mössbauer Spectrometer

The Mössbauer spectrometer is of the conventional type. We will only give a brief description, since further details can be found in previous theses [1,12,13]. A block diagram of the spectrometer can be found in fig. 3.5. The clock controls the timing of the spectrometer. The digital function generator (DFG) generates a channel advance (CA), a multi scaling start (MSS) and a reference signal. The first two control the multi channel analyzer (MCA). The reference signal is of triangular form and determines the movement of the source. The drive amplifier is based on a feedback principle. Its output is presented to the drive coil of the transducer, which is placed in a magnetic field. The difference between the reference and a feedback signal that comes from a pick-up coil in the transducer is minimized by the drive amplifier. To a good approximation the velocity of the source is proportional to the triangular reference signal. During one period a spectrum with increasing and decreasing velocity is taken simultaneously. Usually each spectrum contains 256 channels. Originally a clock, DFG, drive amplifier and transducer were used that have been made in our laboratory. Recently, these were replaced by a commercially available system (Wissel, drive transducer and amplifier 260, and DFG with built in clock DFG-100).

The velocity calibration is performed by means of a Michelson interferometer. A moving mirror is placed on the transducer rod onto which also the source is

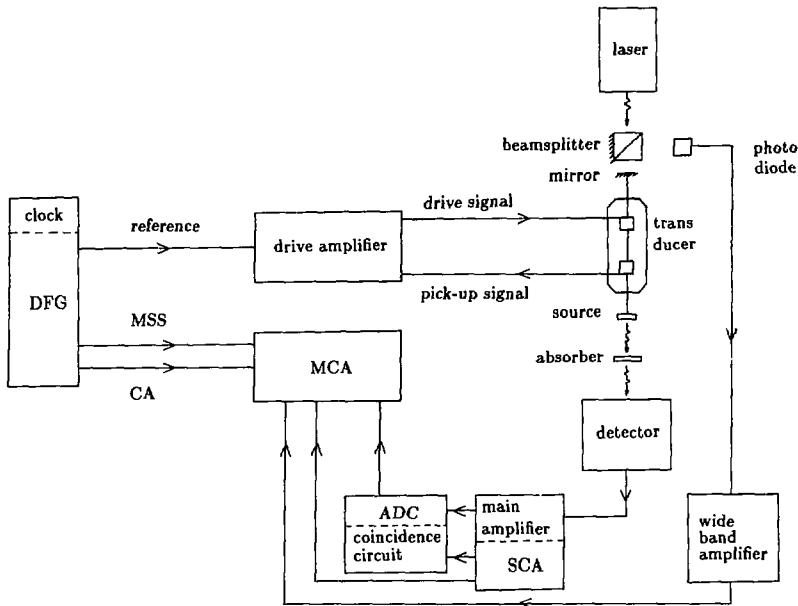


Figure 3.5: Block diagram of the Mössbauer spectrometer.

mounted. A Ne-He laser, which is placed in the top part of the exchange gas space, provides the monochromatic light. A photo diode registers the minima of the interference. A wide band amplifier and pulse shaper translates these minima into pulses that can be stored in the MCA. The velocity in each channel  $v_i$  can be calculated from the formula

$$v_i = \frac{\lambda N n_i}{2t}, \quad (3.3)$$

where  $N$  is the number of channels,  $n_i$  the number of counts in channel  $i$ ,  $\lambda$  the wave length of the light (6328 Å), and  $t$  the calibration time normally chosen to be 600 s. Since the source was mounted on the far end of the driver rod, natural iron spectra have been measured to rule out the effects of the elasticity of the rod. The line positions of the iron foil correspond within 0.01 mm/s with the values available in the literature.

The  $\gamma$ -rays of  $^{57}\text{Fe}$  are detected by means of a proportional counter. The commercially bought detectors (Harwell) have been provided with a valve in order to make the replacement of the gas filling (90 % Ar and 10 %  $\text{CH}_4$  at 0.7 atm) possible. The performance of the quench gas  $\text{CH}_4$  declines, resulting in an unacceptable energy resolution after roughly half a year. Since Harwell stopped producing Mössbauer equipment, two detectors have been copied in the workshop of our laboratory for a fraction of the price. An intrinsic Ge detector (Harshaw, HPP32) with a crystal of 7 mm thick has been used for the detection of the  $\gamma$ -rays of the  $^{197}\text{Au}$  transition. The thickness of the crystal is chosen in such a way that the efficiency

of the detector is maximum (80 %) around 100 keV, and falls off below 10 % at a few hundred keV. High energy radiation like e.g. the 268.8 keV  $\gamma$ -rays of  $^{197}\text{Au}$  is therefore scarcely detected, preventing any saturation effects in the electronics. The energy resolution of the intrinsic Ge detector is of the order of 2 %, which reduces with increasing count rate, and becomes unacceptable at count rates of  $10^5$  cps.

The pulses originating from the detector are amplified and shaped by a main amplifier. A single channel analyzer singles out pulses in a restricted voltage range, corresponding to the energy range containing the Mössbauer radiation (Ortec, 590A). The TTL output pulses of the single channel analyzer are stored in the MCA. An analog to digital converter (ADC) generates a pulse height spectrum which can be stored in the MCA. The pulse height spectrum gives information on the performance of the detector and the relative thickness of the absorbers (see section 3.4). Moreover, the adjustment of the single channel analyzer becomes very simple, since the part of the pulse height spectrum that is selected by the single channel analyzer can be visualized by means of a coincidence circuit. Most of the spectra described in this thesis have been taken using an MCA based on a 8085 microprocessor [12]. A LSI 11/23 computer controlled the microprocessors and made it possible to inspect and save the measured data. The pulse height spectra were taken by a ND-2200 series MCA. At a later stage a commercially available MCA card (Intequip Nuclear BV) that fits in a IBM compatible PC was purchased. This plug-in card can be used in multi channel scaling mode and in pulse height analysis mode, using a separate ADC (Silena, 7411/N). Analysis of the Mössbauer spectra is performed on a VAX 11-750 and a main frame IBM 3083 computer.

### 3.4 Source and Absorber Preparation

The source for the  $^{197}\text{Au}$  measurements consists of a platinum foil enriched to 45.8 % in  $^{196}\text{Pt}$ <sup>1</sup>. It was irradiated for 24 hours in a flux of  $2 \cdot 10^{12}$  neutrons/cm<sup>2</sup>/s at the Interuniversitair Reactor Instituut te Delft. A fraction of the  $^{196}\text{Pt}$  captures a neutron and decays to  $^{197}\text{Au}$  with a half life of  $t_{1/2} = 18$  h (see fig. 3.6). The obtained activity was estimated to be between 40 and 50 mCi. The source can be transported 3 h after the irradiation and the first spectra were already taken after 5 h. The source has an useable lifetime of roughly three half lives. During one run, approximately 15 spectra could be measured. The absorbers for the  $^{197}\text{Au}$  experiments are prepared of finely powdered material, avoiding any line intensity asymmetries due to texture. A ring containing the absorber material is wrapped in aluminium foil, which provides for the thermal contact and an homogeneous temperature. If sufficient sample material was available, absorbers with 250 mg/cm<sup>2</sup> of Au were used. This roughly corresponds with a relative absorber thickness of three. The accompanying line broadening can be accounted for by the use of the transmission integral method (cf. section 2.6).

<sup>1</sup>Kindly provided by the molecular spectroscopy group of the Katholieke Universiteit te Nijmegen.



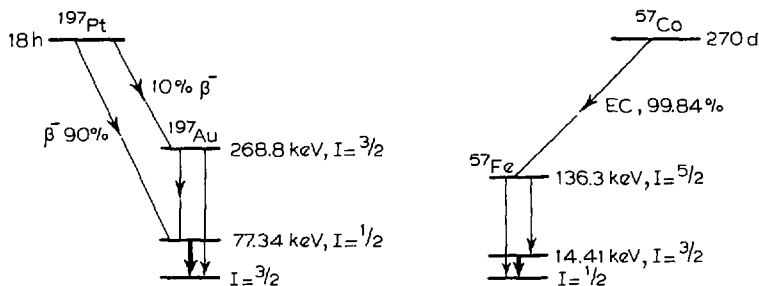


Figure 3.6: Decay schemes of  $^{197}\text{Pt}$  and  $^{57}\text{Co}$ .

For  $^{57}\text{Fe}$  measurements commercially obtained  $^{57}\text{Co}:\text{Rh}$  sources with an initial activity of 100 mCi were used.  $^{57}\text{Co}$  decays by electron capture to  $\text{Fe}$ , with a half life of 270 days (see fig. 3.6). The powder absorbers are prepared with the same considerations as mentioned above. The relative absorber thickness is chosen to be roughly two, which corresponds to about 8 mg natural  $\text{Fe}$  per square cm.

In order to apply an external magnetic field along a well defined crystallographic axis, single crystal absorbers have been prepared. Temperature independent line broadening that has been observed in Mössbauer experiments in an applied field, has been attributed to a misalignment of the single crystals [12,14]. Therefore, special care is taken to orient the crystals with an accuracy of one degree. Moreover, the crystal platelets must have a thickness of the order of 0.1 mm/s to make Mössbauer experiments possible. For the preparation of the single crystal absorbers, the following procedure has been employed. The crystal is set on a goniometer and oriented<sup>2</sup> using the Laue method of X-ray scattering [15]. With a rectangular device the oriented crystal is placed without loss of orientation in a delrin cylinder, of which the axis will correspond to the preferred  $\gamma$ -ray direction. The crystal is circumfused with a two component epoxy resin (Stycast 1266). The plastic cylinder containing the crystal is sawed into thin slices. With several small crystal platelets, a mosaic can be formed. One face of the mosaic is exposed and rubbed down manually with fine abrasive paper until a large well defined crystal surface appears. This face is then covered by a thin layer of epoxy resin. Subsequently the other face of the mosaic is exposed and rubbed down. Initially the thickness of the absorber is followed by taking pulse height spectra several times during the rubbing down process. After a  $\gamma$ -ray peak appears in the pulse height spectrum, it becomes also worthwhile to take Mössbauer spectra to determine the optimal thickness. This occurs if the product of the percentage absorption of the Mössbauer spectrum and the square root of the transmitted counts per unit time is maximized. When this product starts to decrease again, the absorber is assumed to have the right thickness and the mosaic is covered with epoxy resin. Subsequently, a lead mask is made which prevents the  $\gamma$ -rays to pass around the crystal.

<sup>2</sup>We are indebted to the group of Prof. Dr. Tuinstra of the Technische Universiteit te Delft for the use of their X-ray apparatus and acknowledge in particular A. van den Berg for his assistance.

The resulting platelet is glued in a brass ring with an external spherical shape. This ring is mounted on the goniometer and Laue exposures are taken for the final orientation adjustments. In addition, the relative orientations of the crystallites of the mosaic can be checked. By means of the above mentioned rectangular device this ring is placed in another ring, with a half spherically shaped aperture. In this way we define the base of the latter ring as the plane perpendicular to the crystal axis parallel to which the field and  $\gamma$ -rays will be. The ring can be placed in the drawer system of the absorber block as discussed in section 3.2.

The here described method of orientation assures a crystal orientation with an accuracy of the order of one degree.

### 3.5 Absolute Debye-Waller Factor Determination

For the  $^{197}\text{Au}$  measurements, it turned out to be of relevance to enable an absolute determination of the Debye-Waller factor of the absorber. The energy resolution of the detector of about 2 % allows selection of the 77.4 keV resonance line only. Therefore, the transmission integral method described by eq. 2.45 in section 2.6 can be applied. The Debye-Waller factor of the absorber,  $f_a$ , and of the source,  $f_s$ , determine the line intensity.  $f_s$  has been calibrated by means of measurements at 4.2 K on a rolled gold foil. Its thickness has been measured (168.4 mg/cm<sup>2</sup>) and the absolute Debye-Waller factor of bulk Au has been taken from an accurate experimental study of Erickson [16].

Furthermore, these measurements have been repeated at various times during the useable life of the source. The absolute Debye-Waller factor of the source appeared to increase with time. We think this results from the dead time,  $t_d$ , in the detector, and assume that the effective Debye-Waller factor,  $f_s(t)$ , of the source has a simple dependence on time

$$f_s(t) = f_{s,\infty}(1 - t_d R_0 2^{t/t_d}), \quad (3.4)$$

where  $f_{s,\infty}$  is the actual Debye-Waller factor of the source which is observed at infinite time, and  $R_0$  is the initial count rate.  $f_{s,\infty}$  was estimated to be 0.220( $\pm 0.005$ ), the value obtained in two different gold runs after more than four half lives. In fig. 3.7, the logarithm of the experimentally obtained  $f_s(t) - f_{s,\infty}$  is plotted versus the time at which the calibration spectrum is taken ( $t = 0$  corresponds to the moment the source is taken out of the reactor). From this plot the product  $t_d R_0$  is determined to be 0.39, which corresponds to a dead time of approximately 4.5  $\mu\text{s}$  (during the experiment the count rate was monitored). For each spectrum an effective Debye-Waller factor of the source has been calculated.

Since the absorber and the source are located quite closely to one another in the exchange gas space, heating the absorber will have an effect on the temperature of the source. Therefore the temperature of the source was monitored, using an Allan & Bradley carbon resistance thermometer. A Debye approximation was used to correct the Debye-Waller factor of the source. The Debye temperature for the Au:Pt source was estimated to be 186( $\pm 3$ ) K.

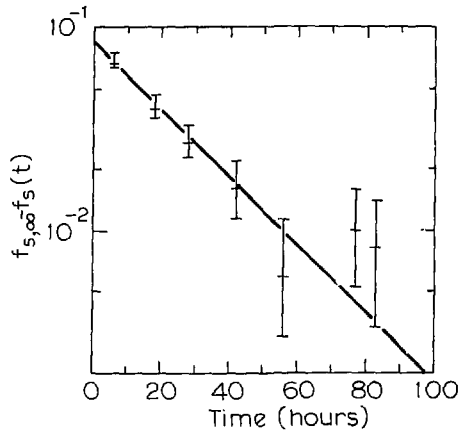


Figure 3.7: Difference between actual and observed Debye-Waller factor  $f_{s,\infty} - f_s(t)$  of the source as a function of time.

A measurement to check the determination of the absolute f-factor was performed on a gold foil at 42 K. The measured  $f_s$  coincided with the value reported by ref. [16] within 5 %.

## References

- [1] F.J. van Steenwijk, Thesis Universiteit te Leiden (1976).
- [2] T. Vieggers, Thesis Universiteit te Nijmegen (1976).
- [3] R.C. Thiel, H.J.M. de Groot, J.W.C. de Vries, *Cryogenics* 24 (1984) 702.
- [4] O.V. Lounasmaa, "Experimental Principles and Methods Below 1 K", Academic Press, London (1974).
- [5] R.R. Conté, T. Kitchens, and T. Overluisen, *Cryogenics* (1972) 138.
- [6] M. Gauthier and E.J.A. Varoquaux, *Cryogenics*, (1973) 272.
- [7] M. Durieux et al, *Metrologia* 15 (1979) 65.
- [8] H.H. Sample, B.L. Brandt, and L.G. Rubin, *Rev. Sci. Instrum.* 53 (1982) 1129.
- [9] L.J. Neuringer and Y. Shapira, *Rev. Sci. Instrum.* 40 (1969) 1314.
- [10] M.W. Dirken, R.C. Thiel, H.H.A. Smit, and H.W. Zandbergen, submitted to *Physica C*.
- [11] H.H.A. Smit, T.A.M. Haemers, R.C. Thiel, L.J. de Jongh, W.M. Reiff, and D.H. Jones, to be published.
- [12] H.Th. Le Fever, Thesis Universiteit te Leiden (1980).
- [13] H. de Graaf, Thesis Universiteit te Leiden (1982).
- [14] H.H.A. Smit, H.J.M. de Groot, R.C. Thiel, L.J. de Jongh, C.E. Johnson, and M.F. Thomas, *Sol. St. Commun.* 53 (1985) 573.
- [15] E.W. Nuffield, "X-ray diffraction methods", Wiley (1966).
- [16] D.J. Erickson, L.D. Roberts, J.W. Burton, and J.O. Thomson, *Phys. Rev. B* 3 (1971) 2180.

## 4 Non-linear Excitations in Ising-like Quasi One-dimensional Magnetic Systems

### Abstract

Temperature and field dependent Mössbauer effect spectroscopy measurements on the Ising-like antiferromagnetic chain systems  $\text{FeC}_2\text{O}_4 \cdot 2\text{H}_2\text{O}$  and  $\text{RbFeCl}_3 \cdot 2\text{H}_2\text{O}$  are reported. The spectra of these systems show relaxation behaviour over a large temperature range which can be explained in terms of non-linear excitations. The influence of an applied magnetic field has been studied. An attempt to describe the excitations by the ideal kink gas resulted in three major discrepancies. We discuss a phenomenological model which is based on the excitation spectrum of the Ising-like chain system and which is compatible with the present data and the experimental data in the current literature.

### 4.1 Introduction

In recent years one-dimensional (1-d) magnetism has gained renewed interest, since it has proven to generate model systems for investigating non-linear excitations, see e.g. ref. [1]. Non-linear excitations, as solitons or kinks, are local excitations that connect degenerate ground states. In a ferromagnet, a  $\pi$ -soliton mediates a spin up and spin down region (fig. 4.1a). Similar  $\pi$ -solitons separate degenerate ground state configurations of the antiferromagnetic chain, which are obtained by a simultaneous rotation of the spins of the two sublattices over an angle  $\pi$  (fig. 4.1b). We will use the term soliton for the large amplitude solutions of a non-linear differential equation (e.g. the sine-Gordon equation). In highly anisotropic systems, the soliton width decreases to zero, as depicted for an antiferromagnetic chain system in fig. 4.1c. We will refer to these "narrow" solitons as kinks. Under the assumption that the kinks neither interact with other kinks nor with the lattice, they can be described as an ideal kink gas. These free kinks have the intriguing characteris-

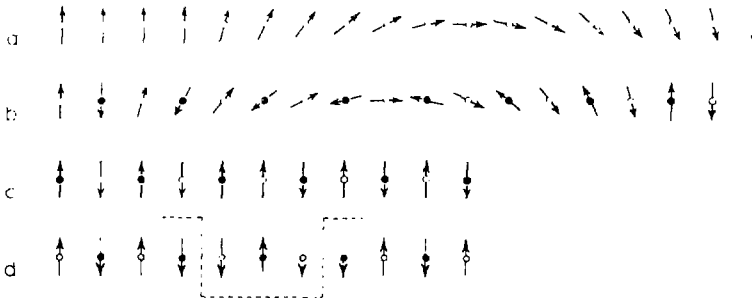


Figure 4.1: Non-linear excitations in magnetic chains: a,b)  $\pi$ -soliton in a classical ferro- and antiferromagnetic chain, and c,d) single kink and a kink pair excitation in a quantum mechanical  $S = \frac{1}{2}$  antiferromagnetic chain.

tic that their energy is preserved when they are translated along the chain, which means that an initially given momentum is constant during the propagation. The dynamic behaviour of the kinks determines the spin correlation function. With the Mössbauer effect one probes the autocorrelation function,  $\langle S^z(0)S^z(t) \rangle$ , of the electronic spins on the magnetic chains. The Mössbauer effect spectroscopy (M.E.S.) has proven to be a very valuable tool for observing the dynamics of kinks, since its frequency window ( $10^5$  to  $10^9$  Hz) is well below that of neutron diffraction measurements. It carries, therefore, the information about the long-time correlations of the electronic spins inaccessible by the neutron scattering technique.

In earlier papers and theses of our group, it has been shown that relaxation behaviour, resulting from non-linear excitations, appears both in ferro- and antiferromagnetic Ising-like chain systems at temperatures roughly between  $T_c$  and  $3T_c$ , where  $T_c$  is the three-dimensional (3-d) ordering temperature [2-7]. In this temperature regime the compounds are 1-d model systems, since the intra-chain interactions are larger than the thermal energy,  $k_B T$ , resulting in strong 1-d correlations, whereas the inter-chain interactions that cause the 3-d ordering at  $T_c$ , are still too weak to play an important role. In the earlier work, the measured spectra seemed to fit the stochastic model for the M.E.S. line shape of Blume and Tjon quite well, which made it possible to evaluate relaxation frequencies in MHz. The activation energy, as determined from the electronic flip rate as a function of the inverse temperature, was systematically found to be twice the energy of a single kink, that is it corresponds instead to the energy of a kink pair (see fig. 4.1d). This posed a problem for some time, since ideal kink gas descriptions predict the activation energy to be that of a single kink. Moreover, M.E.S. experiments on  $\text{Fe}(\text{NH}_4)_2(\text{SO}_4)_2$  showed the superposition of two subspectra in a compound with only one crystallographic iron site [8]. This could be interpreted in terms of a slowly and a fast relaxing subspectrum, of which the static Mössbauer parameters are identical [4]. The slowly relaxing subspectrum showed again the activation energy of twice the kink energy, whereas the fast relaxing subspectrum gave a temperature independent relaxation rate. A.c. susceptibility absorption ( $\chi''$ ) measurements between 10 and  $10^6$  Hz on the doped Ising-like ferromagnetic compounds  $M_x\text{Fe}_{1-x}\text{Cl}_2(\text{Py})_2$  (where M is Ni, Cd, Mn, or Co, and Py is  $\text{NC}_5\text{H}_5$ ) revealed the activation energies of both single kinks and kink pairs [5,6].

The first system we report upon in this chapter,  $\text{FeC}_2\text{O}_4 \cdot 2\text{H}_2\text{O}$ , not only shows an activation energy of twice the soliton energy, but also shows systematic deviations between the M.E.S. data and the spectra generated by the stochastic model of Blume and Tjon. We have chosen this particular antiferromagnetic Ising-like chain system, since it has a very pronounced 1-d character and its magnetic characteristics are well known in the literature. The intra-chain exchange interaction,  $J$ , and the 3-d ordering temperature,  $T_N$ , have been reported in independent experimental investigations, namely specific heat and susceptibility studies. Moreover, the hyperfine field in the present system is typically 3 times as large as in the compounds reported earlier [3,7]. The experimental resolution in the relaxation regime is therefore much larger, which allows one to better distinguish between the differ-

ent propagation mechanisms for the kinks, and investigate the shortcomings of the ideal kink gas model. It is interesting to note that already the first N.M.R. experiments on both planar (TMMC) and Ising-like ( $\text{RbFeCl}_3 \cdot 2\text{H}_2\text{O}$ ) indicated deviations from the ideal kink gas behaviour [9,10]. More recently, also low energy neutron scattering and neutron spin echo experiments on TMMC showed shortcomings of the ideal kink gas description [11,12].

In order to investigate the influence of an applied magnetic field on the dynamics of non-linear excitations, M.E.S. experiments on single crystal absorbers have been performed. A suitable candidate is the Ising-like chain system  $\text{RbFeCl}_3 \cdot 2\text{H}_2\text{O}$ , since large single crystals can be grown<sup>1</sup>. Its magnetic quantities,  $T_N$  and  $J$ , have been determined by various magnetic specific heat, magnetization, and susceptibility studies. The electronic spins are ordered antiferromagnetically in a slightly canted configuration. The presence of the resulting ferromagnetic components provides the possibility to overcome the inter-chain coupling and suppress the 3-d ordering temperature to zero by applying a moderate magnetic field parallel to these ferromagnetic components. In this way the influence of the 3-d ordering temperature can be studied.

This chapter will be arranged as follows. In section 4.2 we will give the details of the magnetic properties of the investigated compounds. Section 4.3 will deal with the M.E.S. spectra and elucidate the method of analysis. The discrepancies between the ideal non-interacting kink gas and the experiment will be discussed in section 4.4. In section 4.5 we will propose a phenomenological model, which explains the present data and is compatible with the a.c. susceptibility absorption ( $\chi''$ ) experiments [5,6]. Subsequently, the M.E.S. results will be compared to the N.M.R. and neutron scattering experiments reported in the recent literature (section 4.6).

## 4.2 Properties of the Investigated Compounds

In this thesis we will study two quasi 1-d  $\text{Fe}^{2+}$  magnetic systems by means of the  $^{57}\text{Fe}$  Mössbauer effect. The chain systems under investigation are antiferromagnetically coupled in the chain, and have a large intra- to inter-chain interaction ratio.

The first compound,  $\alpha\text{-FeC}_2\text{O}_4 \cdot 2\text{H}_2\text{O}$  or Fe-oxalate, hereafter referred to as FOX, is known in the literature for quite some years. The structure, as determined by P.C. Carić [13], can be described by the monoclinic space group  $C2/c$  with unit cell dimensions  $a = 12.04 \text{ \AA}$ ,  $b = 5.58 \text{ \AA}$ ,  $c = 9.89 \text{ \AA}$ , and with  $\beta = 127^\circ 34'$ . It is found that the  $\text{FeC}_2\text{O}_4$  units form a linear chain along the  $b$  direction (see fig 4.2a, drawn after Carić). The delocalized  $\pi$ -electrons of the oxalate group serve as an effective intermediary for significant superexchange along the chain [14]. The chains are separated by the water molecules in one direction, whereas the exchange path in the third direction is also quite long (i.e.  $\text{Fe-O}_2\text{-O}_4\text{-Fe}$ , see fig. 4.2b). The ferrous ion is surrounded by a distorted octahedron formed by a rectangle of oxygens of

---

<sup>1</sup>We thank the group of Prof. Dr. W.J.M. de Jonge of the Technische Universiteit te Eindhoven for providing the crystals.

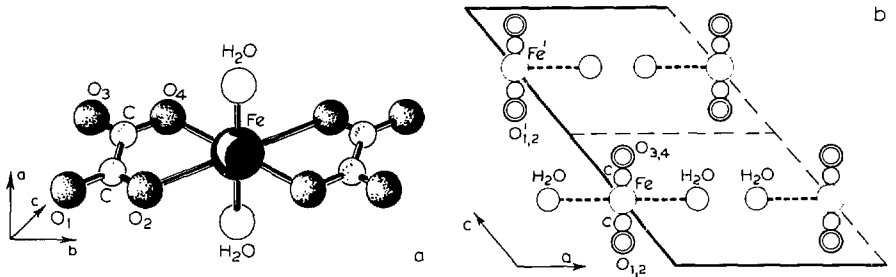


Figure 4.2: Schematic representation of the crystallographic structure of  $\text{FeC}_2\text{O}_4 \cdot 2\text{H}_2\text{O}$  (a), and a projection on the  $ac$  plane of the atomic positions in the unit cell (b).

the oxalate groups and two oxygens belonging to the water molecules.

In earlier work, the Mössbauer data [15,16] have been misinterpreted by attributing the line broadening, observed between about 10 and 25 K, to an additional structure or some cooperative effect. Also, from these data, the 3-d ordering temperature was estimated incorrectly as  $T_N = 26$  K. Only recently the 3-d ordering temperature has unambiguously been determined from a small maximum in the specific heat at 11.7 K [17]. This was confirmed by subsequent neutron diffraction experiments on  $\text{FeC}_2\text{O}_4 \cdot 2\text{D}_2\text{O}$ , reported upon in the same reference. FOX is a very good 1-d system as can be inferred from the size of the peak in the specific heat that accompanies the 3-d ordering. Most of the magnetic entropy is concerned with the 1-d correlations, leaving only a small fraction for the 3-d ordering. The crystal field levels have been determined from ligand field spectra and the temperature dependence of the quadrupole splitting, following the method described in section 2.3.3. The lowest spin quintuplet shows a nearly degenerate doublet as the ground state, the next excited state being at about 60 K. At temperatures low compared to this splitting, only the ground state doublet is populated, resulting in a description of the magnetic properties within the effective  $S = \frac{1}{2}$  Hamiltonian

$$\mathcal{H} = -2J \sum_i (S_i^x S_{i+1}^x + \epsilon S_i^z S_{i+1}^z + \epsilon S_i^y S_{i+1}^y). \quad (4.1)$$

The large single-ion anisotropy is reflected into a strong anisotropy in the exchange constant, i.e.  $\epsilon \ll 1$ . The magnetic susceptibility was fit by the first (Ising) term of this Hamiltonian, yielding  $J/k_B = -82.6$  K [17].

We have also examined an Fe-oxalate compound with a substitution of the water molecules by Imidazole ( $\text{Iz}$  or  $\text{C}_3\text{N}_2\text{H}_4$ ). The crystal field at the iron sites changes drastically by this substitution, since the nitrogen atoms enlarge the distortion of the octahedral surrounding. This results in a change of sign of the observed quadrupole splitting, and the spin anisotropy changes from Ising- to XY-like. From the temperature dependence of the hyperfine field we estimate the 3-d ordering temperature as 5.4 K. Since the M.E.S. measurements do not show relaxation behaviour over a large temperature range in this compound, the estimation of the 3-d

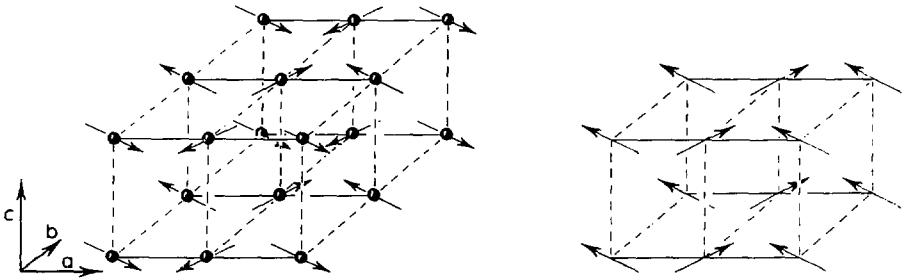


Figure 4.3: Representation of the magnetic structure of  $\text{RbFeCl}_3 \cdot 2\text{H}_2\text{O}$  a) at zero field and temperature and b) as proposed at  $B_c > 1.24$  T and zero temperature.

temperature by the M.E.S. experiments can be trusted to within a few tenths of a degree Kelvin. An attempt has been made to calculate the crystal field levels. This gave a lowest spin quintuplet, with a singlet as the ground state and the first excited doublet at a few degrees Kelvin, resulting in a negligible easy axis anisotropy in the easy plane. The value of  $\eta$ , as found in ref. [16] and confirmed by our experiment, probably finds its origin in a difference in direction of the main axes of the electric field gradient contributions due to the lattice and due to the valence electrons.

The second compound is  $\text{RbFeCl}_3 \cdot 2\text{H}_2\text{O}$ , which will be denoted as RFC in what follows. Large single crystals with typical dimensions of  $2 \times 2 \times 0.5$  cm<sup>3</sup> were grown by slow evaporation of anhydrous  $\text{FeCl}_2$  and  $\text{RbCl}$  in a 0.03*N* solution of  $\text{HCl}$ . The nearly transparent crystals are stable in normal atmosphere and may be cleaved easily along the *ab* plane. The crystallographic structure as determined by neutron diffraction experiments [18] can be described by the orthorhombic space group  $P2/c2/c2/a$ . The unit cell accommodates four formula units and has the dimensions  $a = 8.876$  Å,  $b = 6.872$  Å, and  $c = 11.181$  Å at 4.2 K. The magnetic structure of RFC as reported in the literature [18] is shown in fig. 4.3a. The antiferromagnetic chains are along the *a* axis, where the chlorine ions give rise to the superexchange interaction between the ferrous ions. The magnetic interaction in the *b* direction is two orders of magnitude smaller than in the *a* direction, since the chains are separated by the Rb ions. The magnetic interactions along the *c* axis, where the water molecules separate the chains, are again weaker. Magnetic specific heat measurements revealed a sharp anomaly at 11.96 K, indicating the 3-d ordering [19]. They could best be fit by the rectangular  $S = \frac{1}{2}$  Ising model with an intra-chain interaction  $J_a/k_B = -39$  K and an inter- to intra-chain interaction ratio  $J_b/J_a = 2 \cdot 10^{-2}$ . Single crystal susceptibility measurements [20] and the temperature dependency of the quadrupole splitting [8] could be explained by a lowest spin quintuplet that shows a nearly degenerate doublet ground state with the next excited state at 60 K. This indicates that the magnetic properties of RFC below this temperature can be described by an effective spin  $S = \frac{1}{2}$  Hamiltonian (eq. 4.1).

The magnetic moments are slightly canted by an angle of 19° from the *a* axis



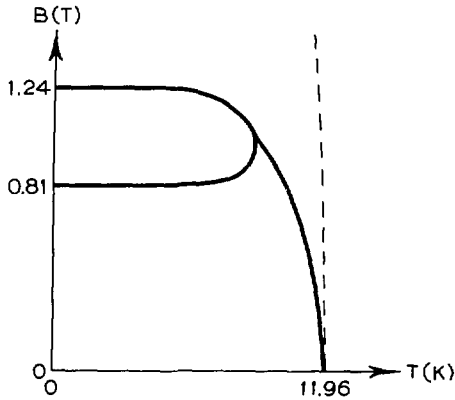


Figure 4.4: A schematic representation of the phase diagram for  $\text{RbFeCl}_3 \cdot 2\text{H}_2\text{O}$ , drawn after ref. [20]. The solid and the broken lines represent the phase boundaries, if the applied field is parallel to the ferro- and antiferromagnetically aligned spin components, respectively.

towards the  $c$  direction. This results in weak ferromagnetic components in the  $ac$  planes, which are however alternating in going from one plane to the next (fig. 4.3a). For an applied field  $B_c = 0.81$  T along the  $c$  axis, a first order spin transition occurs [20], and for  $B_c > 1.24$  T, the weak ferromagnetic components are aligned parallel to the field in the magnetic structure shown in fig. 4.3b (at  $T = 0$  K). In this way the 3-d ordering temperature can be completely suppressed in a moderate applied field. A schematic representation of the phase diagram, drawn after ref. [20] can be found in fig. 4.4.

## 4.3 Mössbauer Spectra and Analyses

### 4.3.1 Excess Linewidth

Some representative powder spectra of FOX are shown below in fig. 4.7. First inspection of the spectra leads to the conclusion that the resonance lines are broadened over a large temperature range. It is obvious from these spectra that the hyperfine field does not decrease to zero at the three dimensional ordering temperature,  $T_N$ , which was determined by an independent experimental technique (i.e. specific heat) as 11.7 K [17]. The effective hyperfine field is, therefore, not proportional to the spontaneous magnetization, which fact prohibits to determine  $T_N$  from M.E.S. experiments. The excess linewidth is caused by slow fluctuations of the hyperfine field. Other mechanisms like a distribution of Néel temperatures as suggested and subsequently rejected by Le Fever [8] can also be ruled out here on basis of the pronounced sharp peak in the specific heat measurements. Another possibility would be a distribution of hyperfine fields. This is, however, very unlikely, since FOX is a completely regular crystalline solid, in which a regular 3-d magnetic

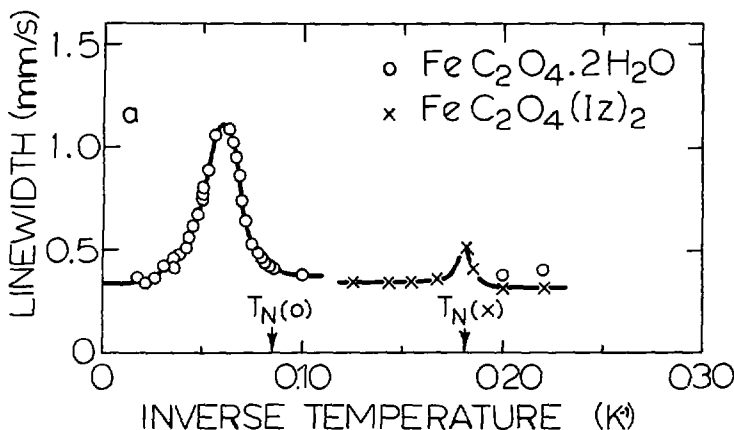


Figure 4.5: Mössbauer linewidth versus inverse temperature for the two Fe-oxalate compounds.

ordering of the moments below  $T_N$  is observed in neutron diffraction experiments [17].

As a first trial, we have analysed the measured spectra in terms of Lorentzians. (N.B. These fits are not those shown in fig. 4.7.) At low temperatures, the fluctuations of the hyperfine field are slow compared to the nuclear level splitting (i.e.  $\Gamma_\omega < \delta$ , see section 2.6.2). Eight Lorentzians are observed, which have been fitted as discussed in section 2.3.4. The excess linewidths were assumed to be equal for all lines. In the high frequency region,  $\Gamma_\omega > \delta$ , the spectra show a doublet with Blume asymmetry. These spectra can be analysed using a doublet with two independent parameters for the linewidths. The averaged results for the linewidth are shown in fig. 4.5.

This figure shows that anomalous line broadening appears over a large temperature range, i.e. between  $\sim T_N$  and  $\sim 3T_N$ . Critical fluctuations accompanying the 3-d ordering cannot account for the observed anomaly, since they will be present in the temperature range  $t = |T - T_N|/T_N < 0.1$  only.

The anomalous line broadening has been observed in a large number of systems [2-7], all of which are characterized by a large Ising-type magnetic anisotropy. Counter examples are e.g. the  $\text{FeC}_2\text{O}_4(\text{Iz})_2$  and  $^{57}\text{Co}:\text{Co}(\text{SO}_4)_2(\text{N}_2\text{H}_5)_2$ , which both show planar (XY-type) anisotropy (see section 4.2 and ref. [2] respectively). For the former, this is experimentally shown by the curve of the excess linewidth in fig. 4.5. Mössbauer source measurements on the latter also lack any slow relaxation behaviour [2]. The absence of slow relaxation behaviour can be understood from the fact that the elementary excitations in the XY systems are spin waves and not solitons [21] (the same argument holds for Heisenberg systems). The fluctuation frequencies are then of the order of  $10^{12}$  Hz, which is much faster than the characteristic Mössbauer frequency. Consequently, the hyperfine field is proportional to

the thermally averaged spin value (or sublattice magnetization) over the complete temperature range. For kink-type excitations to occur, a symmetry breaking Ising component, and thus a degeneracy of the ground state, is a necessary prerequisite.

As a comparison with our data, we want to mention the results on a dilute Fe compound, since it gives interesting information about the relaxation mechanism involved. The Mössbauer spectra of  $\text{Fe}_x\text{Zn}_{1-x}(\text{SO}_4)_2(\text{N}_2\text{H}_5)_2$ , with  $x = 0.07$ , [8] show a single narrow doublet at temperatures down to 4.2 K, and any excess linewidth, as has been observed in the pure Fe compound ( $x = 1$ ) up to much higher temperatures, is absent. As the majority of the ferrous ions ( $\sim 85\%$ ) are surrounded by non-magnetic Zn ions, this observation excludes single-ion relaxation as a possible source for the anomalous line broadening in our quasi 1-d anisotropic magnetic systems.

### 4.3.2 Powder Data and the Blume and Tjon Model

To obtain more information from the measured spectra we have employed the relaxation model of Blume and Tjon (see section 2.6.2; in what follows it will be referred to as the BT model). Especially if  $\Gamma_\omega \approx \delta$ , the BT model provides a way to study the spectra more reliably than the above described method using Lorentzians. Moreover, as discussed in section 2.6.2, the BT model has the advantage that non-adiabatic effects can be taken into account. And finally, since the BT model is based on a stochastic Markov process, this immediately checks whether the relaxation mechanism causes the electronic spins to flip randomly in time. No perpendicular hyperfine field components were considered, since the anisotropy constants are large compared to the temperature. Therefore the main components of the spins are along the easy axis. The same reasoning is used in ref. [22] to justify the neglect of the contribution of the fluctuations of the perpendicular hyperfine field components to the nuclear spin lattice relaxation.

As is shown in fig. 4.6, the BT model does not give an acceptable fit for FOX. In this respect, the magnitude of the hyperfine field is crucial, because it is only for the present large hyperfine field values ( $H_{hf} = 15.0$  T) that the spectra have enough structure and detail in the relaxation regime for the deviations between the data and the fit to become apparent. It is very important to realize that, since the BT model does not fit the data, one may conclude that the effective hyperfine field does not fluctuate randomly in time with a single fluctuation rate for all Mössbauer sites.

An alternative is prompted by the deviations of the fitted line from the data in fig. 4.6, since the data show still some additional Mössbauer lines originating from a hyperfine split subspectrum. The spectra are assumed to consist of two subspectra with equal static M.E.S. parameters (I.S., Q.S.,  $\Gamma_0$ , and  $H_{hf}^0$ ), but different relaxation rates. In several representative spectra (see fig. 4.7) these distinct contributions are separately shown. As can be seen in these figures, very acceptable fits are obtained. The compounds studied in our earlier papers did not exhibit such large hyperfine fields, and were initially fit by a single relaxation spectrum. How-

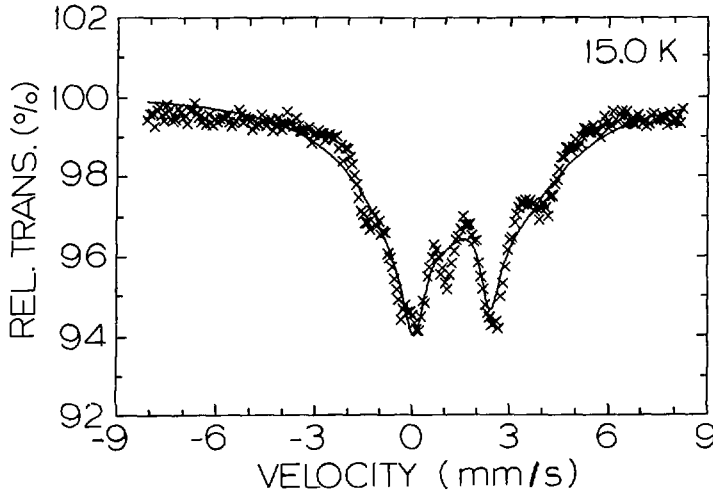


Figure 4.6: Mössbauer spectrum of  $\text{FeC}_2\text{O}_4 \cdot 2\text{H}_2\text{O}$  at 15 K. The solid line represents the best obtainable fit using the Blume and Tjon model with a single relaxation frequency.

Table 4.1: Static M.E.S. parameters as determined at 4.2 K. The I.S. is relative to  $^{57}\text{Co}:\text{Rh}$  at room temperature.

	FOX	FOX( $\text{Iz}$ ) <sub>2</sub>	RFC
I.S. (mm/s)	1.21 (0.02)	1.11 (0.02)	1.19 (0.02)
Q.S. (mm/s)	-1.88 (0.02)	2.06 (0.02)	-1.36 (0.02)
$\eta$	0.7 (0.1)	0.6 (0.1)	0.6 (0.1)
$H_{hf}^0$ (T)	15.0 (0.1)	5.3 (0.1)	7.4 (0.1)
$\theta$ ( $^\circ$ )	84 (5)	72 (5)	29 (2)
$\phi$ ( $^\circ$ )	90 (20)	90 (20)	46 (20)

ever, a refit with the here described procedure also gave better results. In table 4.1 the static Mössbauer parameters are given, which are in agreement with earlier publications, both for FOX [15] and for RFC [8]<sup>2</sup>.

In fig. 4.8 and 4.9 the logarithm of the flip rates of both the relatively slowly and fast relaxing subspectra are plotted versus the inverse temperature for FOX and RFC respectively. The flip rate of the relatively slowly relaxing subspectrum can be described by a thermal activation process:

$$\Gamma_w \propto \exp(-E_a/k_B T). \quad (4.2)$$

The activation energies,  $E_a$ , are 150(20) K and 110(10) K for FOX and RFC re-

<sup>2</sup>Some of the powder results of RFC are obtained from a refit of the data measured by H.Th. Le Fever.

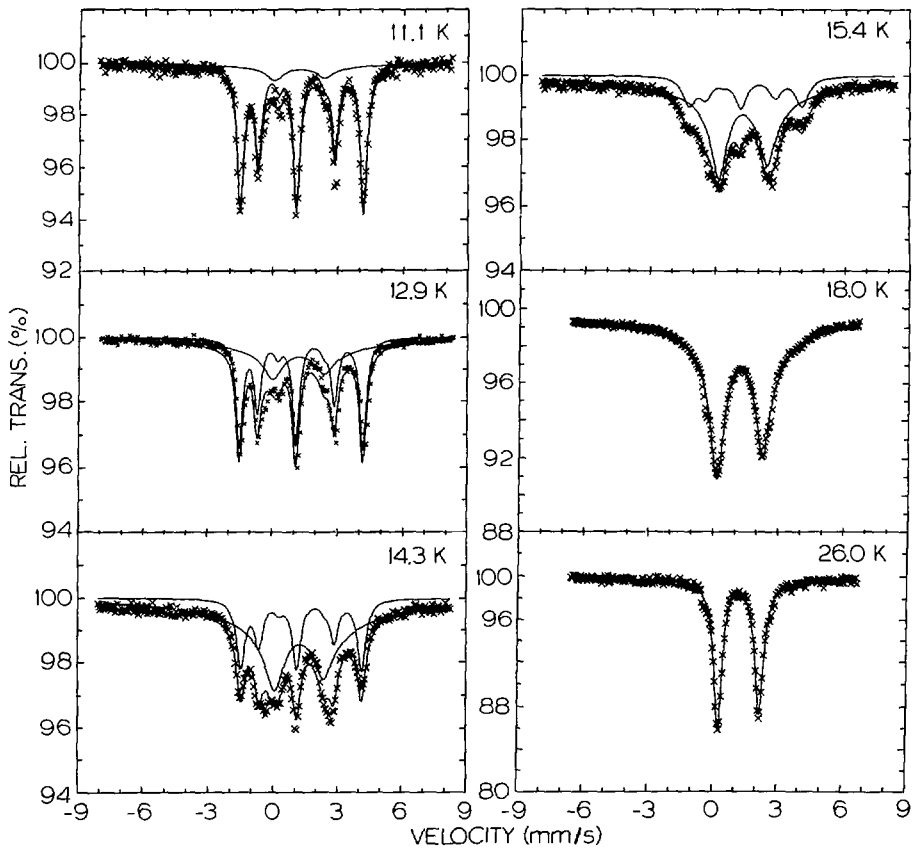


Figure 4.7: Representative M.E.S. powder spectra of  $\text{FeC}_2\text{O}_4 \cdot 2\text{H}_2\text{O}$  at various temperatures. The solid lines represent the two subspectra generated by the Blume and Tjon model and their superposition.

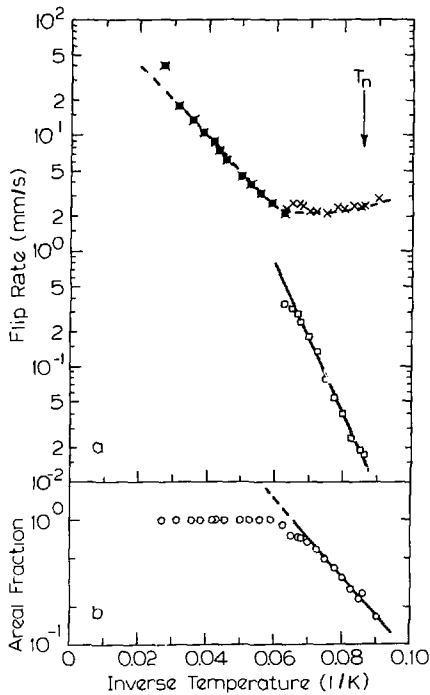


Figure 4.8: The flip rate of the slowly ( $\square$ ) and fast ( $\times$ ) relaxing subspectra of  $\text{FeC}_2\text{O}_4 \cdot 2\text{H}_2\text{O}$ . The lower part shows the relative intensity of the fast relaxing component. The solid lines illustrate the activated processes.

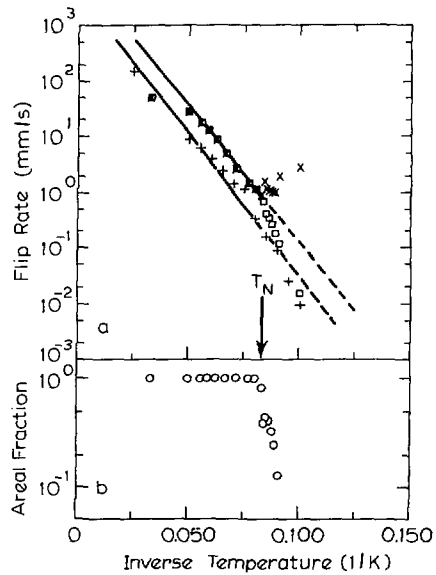


Figure 4.9: The flip rate of the slowly ( $\square$ ) and fast ( $\times$ ) relaxing subspectra of the powder measurements on  $\text{RbFeCl}_3 \cdot 2\text{H}_2\text{O}$ . (+) represents the flip rate obtained from the measurements in a field of 3T along the  $a$  axis. The lower part shows the relative intensity of the fast relaxing component for the zero field data.

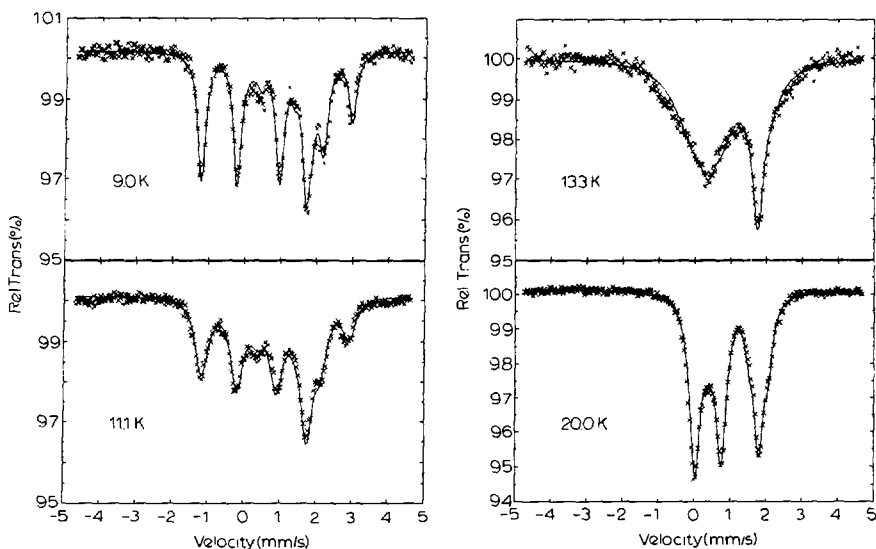


Figure 4.10: Representative single crystal spectra of  $\text{RbFeCl}_3 \cdot 2\text{H}_2\text{O}$  measured in a field of 3T along the  $a$  axis. The solid lines represent the fit using the Blume and Tjon model.

spectively. These activation energies correspond to roughly twice the intra-chain exchange energy, i.e.  $2J/k_B$ , since this amounts to 165 and 78 K, respectively. The relatively fast relaxing component shows a temperature independent relaxation rate of about 40 and 10 MHz for FOX and RFC, respectively. Above a certain temperature, the intensity of the slowly relaxing subspectrum becomes negligible, such that only a single spectrum was sufficient to fit the experiment. In fig. 4.8 and 4.9, also the intensity of the doublet is plotted versus the inverse temperature for each compound. As is clearly seen, the intensity of the doublet increases monotonically as a function of the temperature. In the RFC compound a jump in the relative area of the fast relaxing subspectrum occurs at the 3-d ordering temperature.

#### 4.3.3 Single Crystal Results in an Applied Field

First we will discuss the results of the application of a magnetic field of 3 T along the crystallographic  $a$  axis of RFC. Since the field is directed along the antiferromagnetically aligned components of the spins (fig. 4.3) and the exchange field is of the order of 15 T, the influence of the field on the 3-d ordering temperature can be neglected (see fig. 4.4). Representative spectra are shown in fig. 4.10. At the lowest temperatures, the contributions of the two sublattices can be observed separately, since the effective hyperfine field is the vector sum of the applied field and of the internal field originating from the electrons. At the highest temperatures, the internal hyperfine field fluctuation frequencies are much higher than the

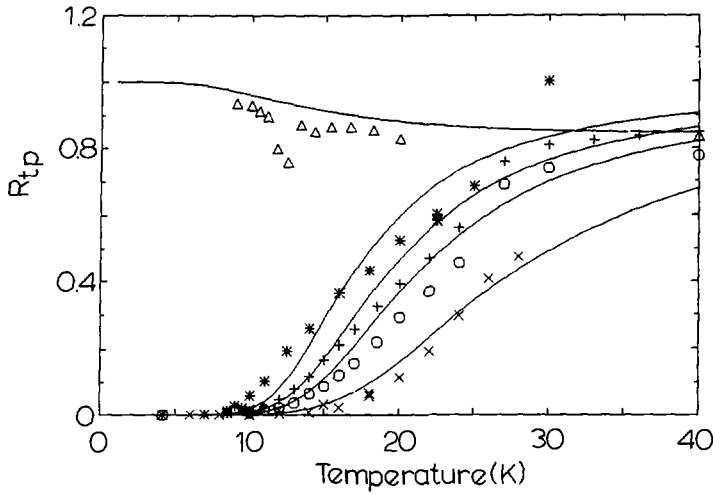


Figure 4.11: Ratio of transition probabilities,  $R_{tp}$ , of  $\text{RbFeCl}_3 \cdot 2\text{H}_2\text{O}$  versus temperature for  $B_a = 3$  T ( $\Delta$ ) and  $B_c = 1.5, 2.25, 3.0, 6.0$  T (\*, +, o,  $\times$  respectively). The solid lines represent the predictions for an ideal  $S = \frac{1}{2}$  Ising chain.

Mössbauer frequency window, such that the internal hyperfine field is proportional to the thermally averaged spin value  $\langle S_x \rangle$ . The spectra were fitted by the BT model, assuming the applied field and the quadrupole splitting to be static, and the internal hyperfine field to jump randomly between  $+H_{hf}$  and  $-H_{hf}$ . The probabilities for the spin being parallel and anti-parallel to the applied field were allowed to be unequal. The static hyperfine parameters were determined at 4.2 K and kept at these values at higher temperatures. Within the experimental accuracy, these parameters correspond to the powder values in table 4.1. The applied field was fixed at 3 T. The polar and azimuthal angles of the  $\gamma$ -rays and the applied field relative to the main axis of the E.F.G. were found to be  $30(5)^\circ$  and  $45(20)^\circ$ , i.e. parallel to the internal hyperfine field, in agreement with ref. [8]. From the fits, shown by the solid lines in fig. 4.10, it can be concluded that a single fluctuation rate is sufficient for fitting the spectra. This is in contrast to the powder measurements as discussed in section 4.3.1. The resulting fluctuation rates can be found in fig. 4.9. An activation energy of 119 (15)K is obtained, which corresponds to the powder value. Below the 3-d ordering temperature, the fluctuation rate falls off steeper than for an activated process. The ratio of transition probabilities, hereafter referred to as  $R_{tp}$ , is defined between 0 and 1. It is plotted in fig. 4.11, where it is shown to be comparable to the prediction for the Ising chain [23], with  $J_a/k_B = -39$  K,  $B = (\mu_a/\mu_B)B_{app}$ , where  $B_{app} = 3$  T and  $\mu_a = 4.6\mu_B$  [20]. Evidently this model neglects the 3-d ordering, and one can see the strongest deviations at temperatures where 3-d critical fluctuations are likely to be present.

Subsequently, magnetic fields of 1.5, 2.25, 3.0, and 6.0 T were applied along the



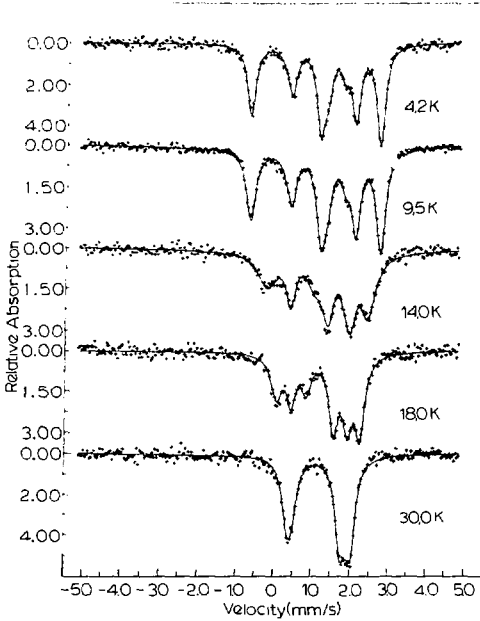


Figure 4.12: Representative single crystal spectra of  $\text{RbFeCl}_3 \cdot 2\text{H}_2\text{O}$  measured in a field of 1.5 T along the  $c$  axis. The solid lines represent the fit using the Blume and Tjon model.

$c$  axis. Representative spectra are shown in fig. 4.12. These fields are sufficiently strong to align the ferromagnetic components of the spins parallel to the field at  $T = 0$  K. As a result, at the lowest temperatures only one magnetic site remains, and the spectra show one octet. The corresponding  $R_{tp}$  is equal to zero. At the highest temperatures, the observed octet has a hyperfine field that is the vector sum of the applied field and the internal field, which is proportional to  $\langle S_x \rangle$ . The spectra were analysed using the BT model, with the same considerations as for the field along the  $a$  axis. The polar and azimuthal angles of the  $\gamma$ -rays and the applied field were found to be  $120(10)^\circ$  and  $45(20)^\circ$  respectively. The fluctuation rates and the  $R_{tp}$ 's as obtained from these fits are plotted in fig. 4.13 and 4.10, respectively. The fluctuation rates follow the exponential behaviour over the whole frequency window of the M.E.S. This is in accordance with suppression of the 3-d ordering temperature by applying magnetic fields larger than 1.24 T along the  $c$  axis. The activation energy appears to increase with increasing applied field. The solid lines in fig. 4.13 correspond to activation energies of 100(10), 130(15), 145(20), and 200(40) K. The  $R_{tp}$ 's correspond quite well to the prediction for the Ising chain [23], where the canted spin configuration was represented by a ferromagnetic chain with  $J_a/k_B = 39$  K and  $B = (\mu_c/\mu_B)B_{app}$ , where according to ref. [20]  $\mu_c = 1.6\mu_B$ .

#### 4.4 Ideal Kink Gas

One of the commonly used non-linear differential equations in the theoretical literature on solitons is the sine-Gordon equation, which describes a continuous

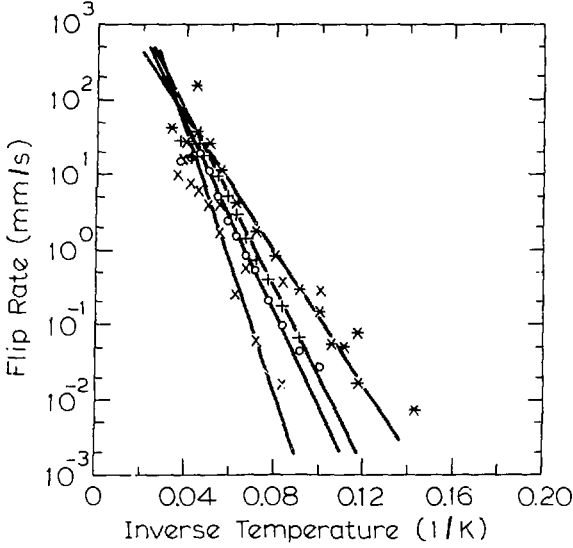


Figure 4.13: The flip rate of the BT fits to the spectra of  $\text{RbFeCl}_3 \cdot 2\text{H}_2\text{O}$  obtained with an applied field of 1.5 (\*), 2.25(+), 3.0 (o), and 6.0 (x) Tesla along the  $c$ -axis. The solid lines illustrate the activated processes.

field  $\phi$  as a function of position (in one dimension) and time [24],

$$\frac{d^2\phi}{dx^2} - \frac{1}{c_0^2} \frac{d^2\phi}{dt^2} = \frac{1}{2d^2} \sin(2\phi). \quad (4.3)$$

This non-linear differential equation has as solutions the solitons and the breathers. Breathers are pulsory excitations that can be viewed as small amplitude kink-antikink pairs or inharmonic phonons [24]. We will not discuss the breathers, since they have negligible effect on the presented results. The soliton solutions of eq. 4.3 can be written as

$$\phi(x, t) = 4 \arctan\left(\exp\left(\pm \frac{\gamma}{d}(x - vt)\right)\right), \quad (4.4)$$

where  $d$  is the soliton width,  $\gamma = (1 - (v/c_0)^2)^{-\frac{1}{2}}$ , and  $c_0$  is the soliton cut-off velocity. The solitons can be seen as relativistic pseudo-particles [24]. A characteristic feature of soliton solutions is that they are found in anisotropic systems and connect degenerate ground states. Solitons do not lose their initial velocity, and when colliding with each other or with impurities suffer only a phase shift [25]. The equation of motion for a system of coupled spins on a discrete chain can be mapped onto the sine-Gordon equation (eq. 4.3) under the following two assumptions: i) the spins can be represented by classical vectors, and ii) the continuum limit can be taken i.e.  $\phi_i - \phi_{i+1} \rightarrow 0$  [26]. For the ferro- and antiferromagnetic chain systems, soliton solutions are illustrated in figs. 4.1a and 4.1b, respectively.

However, since both compounds investigated in this chapter can best be described by the effective  $S = \frac{1}{2}$  Hamiltonian,

$$\mathcal{H} = -2J \sum_i (S_i^x S_{i+1}^x + \frac{\epsilon}{2} (S_i^+ S_{i+1}^- + S_i^- S_{i+1}^+)), \quad (4.5)$$

where  $S_i^\pm = S_i^x \pm iS_i^y$ , the quantum mechanical treatment given by Maki [27] and Villain [28] will be followed. As long as  $\epsilon \ll 1$  and  $J < 0$ , the ground state of Hamiltonian 4.5 is well approximated by the Néel state. The excited states can be approximated by

$$|\cdots + - + -; - + - + \cdots \rangle. \quad (4.6)$$

The spin configuration represented by eq. 4.6 is illustrated in fig. 4.1c. Note that the overlap,  $\epsilon$ , between two excited states, differing only in that the kink is replaced over two lattice sites, is non-zero, which guarantees the dynamic behaviour of the kinks. The theoretical prediction for the thermally averaged kink velocity is given by

$$v_k = \frac{4}{\pi} k_B T \left[ I_0\left(\frac{2\epsilon J}{k_B T}\right) \right]^{-1} \sinh\left(\frac{2\epsilon J}{k_B T}\right), \quad (4.7)$$

where  $I_0(z)$  is a modified Bessel function. The kink density is given by

$$n_k = \frac{1}{2} I_0\left(\frac{2\epsilon J}{k_B T}\right) \exp\left(\frac{-|J|}{k_B T}\right). \quad (4.8)$$

The dynamics of a magnetic chain can be described by the spin correlation function. Only the parallel components are considered, because of reasons discussed earlier (see p. 60). In the free gas approximation for kinks, the spin-spin correlation function is given by [27]

$$\langle S^x(0,0) S^x(x,t) \rangle = \langle S^x \rangle^2 \exp(i\pi x - 2N(x,t)), \quad (4.9)$$

where  $N(x,t) = n_k(x^2 + v_k^2 t^2)^{\frac{1}{2}}$ . The quantity  $\langle S^x \rangle^2$  for a pure Ising system equals  $S^2$ . It can be reduced by perpendicular spin components and by renormalization due to quantum and thermal effects [27], which in our Ising-like compounds can be neglected. As already stated, M.E.S. probes the autocorrelation function, which can easily be obtained by setting  $x = 0$  in eq. 4.9, yielding

$$\langle S^x(0) S^x(t) \rangle = \langle S^x \rangle^2 \exp(-\Gamma_\omega t), \quad (4.10)$$

where  $\Gamma_\omega = 2n_k v_k$  is the relaxation rate or flip rate.

Comparing the autocorrelation function as given in eq. 4.10 with the BT model described in section 2.6.2, one observes that the ideal kink gas is based on precisely the same autocorrelation function as the BT model. Therefore, a comparison between the ideal kink gas and the experimental data is easily performed by analyzing the spectra using the BT model. As described in section 4.3, the following discrepancies result. Firstly, the M.E.S. line shape of the powder spectra does not fit the BT model (fig. 4.6). Secondly, the experimental activation energy is a factor

of two larger than the ideal soliton gas predicts. And finally, if we estimate  $\epsilon \approx 0.1$ , the calculated flip rate at 10 K exceeds the M.E.S. frequency window, which means that the ideal kink gas predicts a doublet over the complete temperature regime investigated. From these three major discrepancies one should conclude that the ideal kink gas is inadequate to describe the autocorrelation function as observed by the Mössbauer effect.

From the spin-spin correlation function (eq. 4.9), the static correlation function can easily be obtained

$$\langle S^z(0) S^z(x) \rangle = \langle S^z \rangle^2 \exp(i\pi x - 2n_k x). \quad (4.11)$$

This indicates that if  $\epsilon = 0$ , the 1-d magnetic correlation length is equal to  $\xi_{1-d} = 1/(2n_k) = \exp(|J|/k_B T)$ . This correlation length corresponds exactly to the prediction for the Ising chain. Quasi-elastic neutron diffraction and susceptibility ( $\chi'$ ) measurements are experimental methods that are sensitive to the magnetic correlation length, and indeed in such studies a correlation length in the chains is found that is proportional to the inverse kink density [3,37]. This seems to be trivial. However, it has a strong implication for the interpretation of our experiment. Namely, a systematic observation of twice the kink energy implies that the autocorrelation function as probed by M.E.S. is *not* simply proportional to the kink density. Therefore, the basis of the ideal kink gas description, which lies in the fact that the relaxation rate is proportional to the product of kink density and velocity (eq. 4.9) breaks down.

Several deviations from the ideal kink gas are dealt with in the theoretical literature. A number of papers are devoted to the two approximations that are made to map a magnetic chain onto the sine-Gordon equation (4.3). The first concerns the description of a discrete number of spins by a continuous field [29-31]. The second approximation concerns the classical treatment of the spins. Dashen et al. [32] investigated the quantum mechanical analogue of the sine-Gordon equation, which gave comparable soliton-like excitations with renormalized soliton width and energy (to higher and lower values respectively). However, the description of Villain and Maki is based on the quantum mechanical chain Hamiltonian (eq. 4.5), such that the above two approximations, as well as their implications for the dynamics of the non-linear excitations, become irrelevant.

## 4.5 Phenomenological Model

The excitation spectrum of the 1-d Ising-like antiferromagnetic chain is known in the literature [33,34]. It is illustrated in fig. 4.14a, which shows three possible classes of excitations. Two of them excite the chain from the ground state (so called inter-band excitations): A) kink pair excitations (with energy  $\sim 2|J|$ , also referred to as magnon bound states [35]), and B) single kink excitations (with energy  $\sim |J|$ ). The third class of excitations contains the intra-band excitations that couple two states in the continuum band around an energy of  $2|J|$ . The single kink excitations are only found in calculations of finite chains if free ends are considered

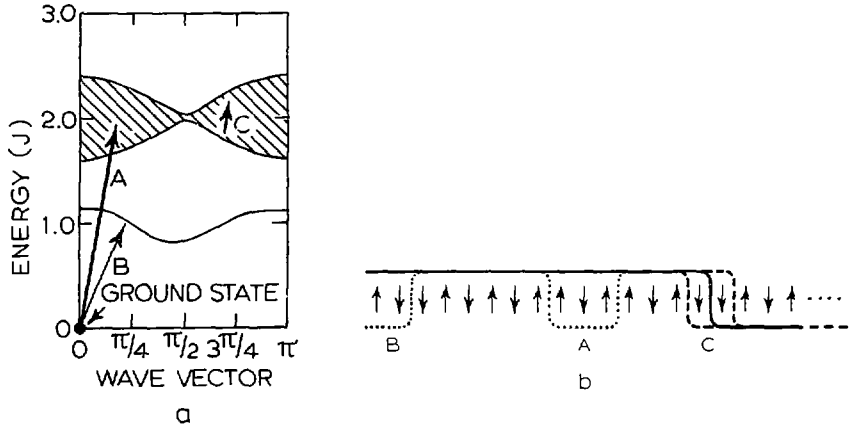


Figure 4.14: Excitation spectrum for a finite Ising-like antiferromagnetic chain system (taken from ref [37]). A) Kink pair or magnon bound state excitations, B) single kink excitations created at the ends of the chain, and C) intra-band excitations. The same excitations are illustrated in an antiferromagnetic chain segment.

instead of cyclic boundary conditions [21]. Moreover, for a chain with  $N$  spins, the statistical weight for exciting single kinks and kink pairs will be proportional to  $N$  and  $N^2$  respectively. Therefore, experimentally, single kink excitations can safely be neglected for sufficiently long chains. Experimental methods like spin cluster excitation [36] and inelastic neutron scattering [37,38], probe the excitation spectrum and indeed find inter-band excitations with energies roughly equal to  $2|J|$ . In addition to these excitations, the latter experiments on  $\text{CsCoCl}_3$  revealed also the presence of the intra-band excitations at much lower energies.

In M.E.S. experiments on powders, two distinct subspectra are observed up to temperatures above which the intensity of one of them becomes negligible. The first is the slowly relaxing subspectrum, which shows an activation energy of about  $2|J|$ . This subspectrum can be identified with the creation and annihilation of kink pairs. In fig. 4.14b, they are illustrated by the dotted line. This is in strong contrast to the ideal kink gas approximation, in which it is supposed that the kinks are present on basis of entropy considerations, and their displacement is responsible for the spin fluctuations. Since the kink pair excitations appear to be thermally activated, it is most probable that the coupling between the phonon bath and the spin system is responsible for their creation and annihilation. The present ferrous chain systems show strong spin-orbit coupling, which may provide for the thermal link between the phonon and the spin system [39]. A quantitative description of the proportionality constant that can be added to eq. 4.2 is at present not available in the literature, but a semi-quantitative approach to a related problem can be found in ref. [40]. The second subspectrum, the doublet, relaxes fast and

shows a temperature independent relaxation rate. We identify this subspectrum with the intra-band excitations illustrated in fig. 4.14a. The level splittings in this kink pair band are small with respect to the temperature, resulting in a fast (paramagnetic) relaxation behaviour. We remark that these rapid fluctuations have to be restricted to only parts of the chain during the characteristic Mössbauer time, since otherwise the slowly relaxing component would simply be not present. In a more phenomenological approach, one can consider the two spins which bracket the kink to be frustrated, since they experience two competing nearest neighbour interactions. Their two possible energy levels, corresponding to spin up and down, are degenerate. An illustration can be found in fig. 4.14b. Since the flip rate is temperature independent, spin-spin interactions are thought to be responsible. If this supposition is true, the relaxation frequency of the order of  $10^7$  to  $10^8$  Hz corresponds to inter-spin distances of between the 10 and 15 Å, which is slightly larger than the inter-chain distance. The fast relaxing component in the spectra disappears if a magnetic field is applied (section 4.3.2). This is as expected, since an applied field polarizes the spins and lifts the degeneracy of their energy levels. The third type of excitations in the Ising-like chain systems, the single kink excitations, are not observed for the reasons given above.

The relaxation behaviour observed at temperatures at which the intensity of the slowly relaxing subspectrum has become negligible, is a result of the combination of the relaxation mechanisms that are depicted in fig. 4.14. The dominating relaxation mechanism determines which activation energy will be observed. In RFC the dominating relaxation mechanism appears to be the thermal excitation of the kink pairs, since an activation energy of about  $2|J|$  is found. Moreover, the measurements in an applied field, which suppresses the intra-band excitations, show the same activated process. In FOX, on the other hand, an activation energy of 70(10) K is found, which is comparable to  $|J|/k_B$ , indicating that the intra-band excitations are dominant. Hence, the relaxation rate is proportional to the density of the kinks.

The phenomenological model presented here was already applied in the work of ElMassalami [5,6], who has performed a.c. susceptibility measurements between 10 and  $10^5$  Hz on the doped Ising-like ferromagnetic compounds  $T_x\text{Fe}_{1-x}\text{Cl}_2(\text{Py})_2$  (where T is Ni, Cd, Mn, or Co, and Py is  $\text{NC}_5\text{H}_5$ ). The real part, ( $\chi'$ ), as well as the imaginary part, ( $\chi''$ ), of the susceptibility as function of frequency could be described by the superposition of two Debye curves. The susceptibility decreases from isothermal in the low frequency regime to adiabatic at high frequencies. The accompanying maxima in the  $\chi''$  showed activated processes with activation energies  $|J|$  and  $2|J|$  respectively. The a.c. field disturbs the equilibrium of the spin system. Thermal excitation of kinks at the ends of the chains and of kink pairs or magnon bound states reestablishes equilibrium. Enlarging the degree of doping evidently breaks up the magnetic chains and creates more excitations. Indeed in the  $\chi''$  experiment, the intensity of the relaxation of single kinks was enhanced in this way. Since the available frequency range was between 10 and  $10^5$  Hz, no indication of the intra-band excitations was found in the susceptibility. However, complementary

Mössbauer studies of these doped materials clearly demonstrated their presence.

## 4.6 Discussion

An important feature of the experimental results is the observation of two sub-spectra, each of which shows a separate relaxation mechanism.

The slowly relaxing subspectrum shows the thermal activation of kink pairs. This relaxation mechanism has not been considered in the ideal gas approximation. Moreover, for the interpretation of the neutron scattering experiments on TMMC and N.M.R. measurements on TMMC and RFC, this kind of excitations are not taken into account. Since the characteristic measuring time for quasi-elastic neutron scattering, using thermal neutrons, is of the order of  $10^{12}$  Hz, it is plausible that the creation of kink pairs, although of dominant importance for interpreting the slowly relaxing Mössbauer subspectrum, does not influence the neutron data.

The second relaxation mechanism observed by the Mössbauer effect concerns the fast (paramagnetic) relaxation of only parts of the chains. This relaxation mechanism might be related to a diffusive motion or random walk of the kinks. A necessary condition is then that this diffusive motion of the kinks is restricted to only parts of the chain during the characteristic M.E.S. time. In that case, a diffusive motion generates a fast relaxing subspectrum with a relative intensity that reflects the fraction of spins that are subject to this motion. The diffusive kink model as proposed in refs. [41,42], describes the N.M.R. data on both TMMC [9] and RFC [10] much better than the ideal kink gas. We want to return briefly to the results of the quasi-elastic neutron scattering on TMMC. During the characteristic time interval of quasi-elastic neutron scattering ( $\sim 10^{-12}$  s), the ideal soliton gas predicts a displacement of the soliton of the order of one lattice unit (according to e.g. ref. [43],  $v_s = 1.4 \cdot 10^{12}$  l.u./s). This might be the reason why the first experiments on TMMC could be interpreted in terms of an ideal soliton gas [43]. In later neutron scattering experiments, where a time resolution of the order of  $10^9$  to  $10^{11}$  Hz was obtained in a spin-echo experiment, deviations from the ideal soliton description were found, and a diffusive propagation behaviour became of importance for the interpretation [11]. As regards the Mössbauer experiments, however, to the authors' knowledge no M.E.S. line shape has been calculated incorporating the autocorrelation function appropriate for kink diffusion or a random walk.

The relative intensity of the fast relaxing component increases with increasing temperature. Since the density of the kinks is proportional to  $\exp(-|J|/k_B T)$ , it is tempting to seek the same temperature dependence for the relative area of the doublet. This seems to be the case for FOX, see fig. 4.8, where an excitation energy of 73(10) K is found. The intensity of the doublet as a function of the inverse temperature for the RFC powder measurements is shown in fig. 4.9. Here the temperatures at which an activated process would be observable, coincide with the 3-d ordering. With the interpretation of the intensity of the fast relaxing component in terms of an activated process one should be careful, however, because the doublet intensity may also be influenced by the number of spins per kink that take part in the

paramagnetic relaxation during the characteristic Mössbauer time. Moreover, the number of imperfections in the chain can change the kink density quite drastically, as is concluded in ref. [5,6,44].

The influence of 3-d ordering in RFC is clearly reflected in the intensity of the fast relaxing subspectrum (fig. 4.9). We believe that, at this temperature, the total number of kinks decreases drastically, because of the onset of magnetic correlation in the directions perpendicular to that of the chain. At zero temperature a perfect antiferromagnetic crystal would not include any kinks, in contrast to the ferromagnet, where demagnetization effects induce domains. Moreover, below the 3-d ordering temperature, the relaxation rate no longer follows that of an activated process, irrespective whether an applied field is present or not. This is also observed in e.g.  $\text{FeCl}_2(\text{Py})_2$  [3]. There is, however, no reason to assume that the coupling between the phonon and the spin system changes at the 3-d ordering. From this it can be concluded that the activated kink pairs that propagate in the paramagnetic state, become frozen in below the 3-d ordering temperature. On the one hand, the propagation above  $T_N$  is in agreement with the overlap between the eigenstates in eq. 4.6, and on the other hand with the experimental results of N.M.R.  $T_1^{-1}$  and neutron diffraction measurements. FOX does not give any indication of what happens at the 3-d ordering temperature, since at this temperature the Mössbauer spectra are already fully split.

If an external field is applied upon RFC parallel to the ferromagnetic components of the spins, the activation energy of the kink pairs or magnon bound states appears to be strongly field dependent. Qualitatively this is evident, since the creation of kink pairs is accompanied by the loss of Zeeman energy of the spins located between these two kinks. It is evident that a quantitative interpretation of the loss of Zeeman energy is dependent on the angle the magnetic spins make with respect to the applied field, which determines the size of the ferromagnetically aligned spin components. If one assumes that the angle of the spins with the applied field is field independent, a quantitative estimate of the average number of spins that are directed anti-parallel to the field during the creation of a kink pair is of the order of ten. The fact that the direction of the internal hyperfine field is only slightly dependent on the applied field gives credence to this quantitative estimate. Moreover, the experimental data of the ratio of transition probabilities,  $R_{lp}$ , as shown in fig. 4.11, are described quite nicely by a field independent ferromagnetic component.

## 4.7 Conclusion

In this paper we have studied the spin dynamics in the highly anisotropic quasi 1-d magnetic systems  $\text{FeC}_2\text{O}_4 \cdot 2\text{H}_2\text{O}$  and  $\text{RbFeCl}_3 \cdot 2\text{H}_2\text{O}$ , as probed by the Mössbauer effect. The first compound exhibits a large hyperfine field, which enhances the experimental resolution. This forced us to interpret the data at low temperatures in terms of two subspectra, with equal static M.E.S. parameters and with different relaxation rates, resulting from two relaxation mechanisms. The slowly relaxing



subspectrum shows a thermal activated process with an activation energy  $2|J|$ . The fast relaxing component has a constant relaxation rate. The intensity of the latter component increases as a function of temperature. Above a certain temperature, only one spectrum can be distinguished. Upon applying a magnetic field, the fast relaxing subspectrum disappears. The activation energy increases with increasing field along the ferromagnetically aligned spin components.

The ideal gas description of non-interacting solitons is unable to describe the data because: i) the relaxation rate predicted by the ideal kink gas is far too high, ii) the spectral line shape calculated with a single Markov process by the BT model does not fit the measured spectra, and iii) the experimental activation energy is twice as large as predicted.

One can understand the observations by assuming: i) frustrated spin regions, where via spin-spin relaxation the flip rate is relatively high and temperature independent, and ii) creation and annihilation of kink-pairs, involving energy exchange with the lattice.

## References

- [1] L.J. de Jongh, *J. Appl. Phys.* 53 (1982) 8018.
- [2] R.C. Thiel, H. de Graaf, and L.J. de Jongh, *Phys. Rev. Lett.* 47 (1981) 1415.
- [3] H.J.M. de Groot, L.J. de Jongh, R.C. Thiel, and J. Reedijk, *Phys. Rev.* B30 (1984) 4041.
- [4] H.J.M. de Groot, PhD. Thesis, Rijksuniversiteit te Leiden (1987).
- [5] M. ElMassalami, H.H.A. Smit, H.J.M. de Groot, R.C. Thiel, and L.J. de Jongh, in *Proc. in Phys.* 23, "Magnetic Excitations and Fluctuations II", eds. U. Balucani, S.W. Lovesey, M.G. Rasetti, and V. Tognetti, p. 178 Springer-Verlag, Berlin (1987).
- [6] M. ElMassalami, PhD. Thesis, Rijksuniversiteit te Leiden (1987).
- [7] H.H.A. Smit, H.J.M. de Groot, R.C. Thiel, L.J. de Jongh, C.E. Johnson, and M.F. Thomas, *Sol. St. Commun.* 53 (1985) 573.
- [8] H. Th. Le Fever, PhD. Thesis, Rijksuniversiteit te Leiden (1980).
- [9] J.P. Boucher, H. Benner, F. Devreux, L.P. Regnault, J. Rossat-Mignod, C. Dupas, J.P. Renard, J. Bouillot, and W.G. Stirling, *Phys. Rev. Lett.* 48 (1982) 431.
- [10] A.M.C. Tinus, C.J.M. Denissen, H. Nishihara, and W.J.M. de Jonge, *J. Phys. C, Sol. St. Phys.* 15 (1982) L791.
- [11] J.P. Boucher, F. Mesei, L.P. Regnault, and J.P. Renard, *Phys. Rev. Lett.* 55 (1985) 1778.
- [12] J.P. Boucher, L.P. Regnault, R. Pynn, J. Bouillot, and J.P. Renard, *Eur. Phys. Lett.* 1 (1986) 415.
- [13] P.C. Carić, *Bull. Soc. Franç. Miner. Crist.* LXXXII (1959) 50.
- [14] S. de S. Barros and S.A. Friedberg, *Phys. Rev.* 141 (1966) 637.
- [15] F. de S. Barros, P. Zory, and L.E. Campbell, *Phys. Lett.* 7 (1963) 135.
- [16] P.C.M. Gubbens, A.M. van der Kraan, J.A.C. van Ooijen, and J. Reedijk, *J. de Phys.* C2 (1979) 328.
- [17] Jiing-Yann Chen, Satoru Simizu, and S.A. Friedberg, *J. Appl. Phys.* 57 (1985) 3338.
- [18] J.A.J. Basten, Q.A.G. van Vlimmeren, and W.J.M. de Jonge, *Phys. Rev.* B18 (1978) 2179.
- [19] K. Kopinga, Q.A.G. van Vlimmeren, A.L.M. Bongaarts, and W.J.M. de Jonge, *Physica* 86-88 B+C (1977) 671.
- [20] Q.A.G. van Vlimmeren, and W.J.M. de Jonge, *Phys. Rev.* B19 (1979) 1503.
- [21] J.D. Johnson and J.C. Bonner, *Phys. Rev.* B22 (1980) 251.
- [22] F. Borsa, *Phys. Lett.* 80A (1980) 309.
- [23] E. Ising, *Z. Phys.* 31 (1925) 253.
- [24] A.R. Bishop, J.A. Krumhansl, and S.E. Trullinger, *Physica* 1D (1980) 1.
- [25] M.B. Fogel, S.E. Trullinger, A.R. Bishop, and J.A. Krumhansl, *Phys. Rev.* B15 (1977) 1578.
- [26] H.J. Mikeska, *J. Phys. C, Sol. St. Phys.* 13 (1980) 2913 & *J. Appl. Phys.* 52 (1981) 1950.
- [27] K. Maki, in "Progress in Low Temperature Physics", ed. D.F. Brewer, North-Holland, Amsterdam (1981) Vol. VIII.
- [28] J. Villain, *Physica* 79B (1975) 1.
- [29] M. Peyrard and M.D. Krumhansl, *Physica* 14D (1984) 88.
- [30] C. Willis, M. El-Batanouny, and P. Stancioff, *Phys. Rev.* B33 (1986) 1904.
- [31] J.F. Currie, S.E. Trullinger, A.R. Bishop, and J.A. Krumhansl, *Phys. Rev.* B15 (1977) 5567.
- [32] R.F. Dashen, B. Hasslacher, and N. Neveu, *Phys. Rev.* D11 (1975) 3424.
- [33] N. Ishimura and H. Shiba, *Prog. Theor. Phys.* 63 (1980) 743.
- [34] H. Yoshizawa, K. Hirakawa, S.K. Satija, and G. Shirane, *Phys. Rev.* B23 (1981) 2298.
- [35] J.B. Torrance Jr. and M. Tinkham, *Phys. Rev.* 187 (1969) 587 & 595.
- [36] Q.A.P. van Vlimmeren, C.H.W. Swüste, W.J.M. de Jonge, M.J.H. van der Steeg, J.H.M. Stoelinga, and P. Wyder, *Phys. Rev.* B21 (1980) 3005.

- [37] S.E. Nagler, W.J.L. Buyers, R.L. Armstrong, and B. Briat, *Phys. Rev. B* **28** (1983) 3873.
- [38] W.J.L. Buyers, M.J. Hogan, R.L. Armstrong, and B. Briat, *Phys. Rev. B* **33** (1986) 1727.
- [39] R. Orbach, *Proc. Roy. Soc. London*, **A264** (1961) 458.
- [40] M. Tinkham, *Phys. Rev.* **188** (1969) 967.
- [41] K. Maki, *Phys. Rev. B* **24** (1981) 335.
- [42] L. Gunther and Y. Imr, *Phys. Rev. Lett.* **44** (1980) 1225.
- [43] J.P. Boucher and J.P. Kenard, *Phys. Rev. Lett.* **45** (1980) 486.
- [44] T. de Neef, *J. Phys. Soc. Japan*, **37** (1974) 71.

## 5 Mössbauer and Specific Heat Studies of the Vibrations of Metal Core atoms in Polynuclear Gold Cluster Compounds

### Abstract

$^{197}\text{Au}$  Mössbauer effect spectroscopy and specific heat measurements have been performed as a function of temperature on the three gold polynuclear cluster compounds  $[\text{Au}_9(\text{PPh}_3)_8](\text{NO}_3)_3$ ,  $\text{Au}_{11}(\text{PPh}_3)_7(\text{SCN})_3$ , and  $\text{Au}_{55}(\text{PPh}_3)_{12}\text{Cl}_6$ . The Mössbauer data yield information on the vibrational motions of the various distinguishable Au sites, as well as on the motion of the clusters as a whole. The Mössbauer and the specific heat data are successfully described by a superposition of inter- and intra-cluster vibrations. The latter are determined by calculating numerically the normal modes of vibration of the metal cores.

### 5.1 Introduction

During the last decade chemists have made considerable progress in synthesizing polynuclear metal cluster compounds [1-4]. Ru, Rh, Pt, and Au metal cluster compounds with a nuclearity of 55 [5,6], and even a Pd cluster compound with about 560 core atoms have been reported [7]. Metal cluster compounds are chemically synthesized materials, composed of large and in some cases giant molecules, which are made up of a metal core that is surrounded by a shell of ligands. The ligand shell in many cases stabilizes the metal core and prevents the metal cores from coalescing. A big advantage in comparison to e.g. colloidal metal particles is that a cluster compound is formed out of completely identical clusters, both in nuclearity number and in structure. Moreover, in contrast to mass spectroscopic experiments on clusters formed in beams, large amounts of material can be supplied, often in the order of grams. Finally, one is able to study their properties as a function of cluster size. Interest in the physical and chemical properties of small metal particles has revived in recent years [8]. Fundamental questions arise when the particle size becomes so small that the bulk properties are lost (quantum size effects). Moreover, the fraction of surface atoms is very large. Consequently, they are model systems for surface effects and may be of interest for the understanding of the properties of small metal particle catalysts.

A few years ago our group started a systematic study of the physical properties of polynuclear metal cluster compounds. Magnetization and susceptibility measurements have been performed on a.o. Ni and Pt carbonyl clusters [9] and an N.M.R. study of Pt carbonyl clusters was reported [10]. The  $\text{Au}_{55}(\text{PPh}_3)_{12}\text{Cl}_6$  cluster compound was found to show interesting dc-conductivity behaviour [11] and was studied by means of  $^{197}\text{Au}$  Mössbauer experiments [12]. The Mössbauer effect spectroscopy (M.E.S.) provides an ideal microscopic tool to probe the chemical environment of the metal atoms in cluster compounds via their isomer shifts (I.S.) and quadrupole splittings (Q.S.). The metal core is composed of Au atoms occupying inequivalent

sites, since inner-core atoms are coordinated to other Au atoms only, and surface atoms of the metal core are either unbonded or bonded to different ligands. The inequivalent sites can be distinguished on the basis of their I.S. and Q.S. In addition, by studying the temperature dependence and the absorption intensities of the M.E.S. spectra, information on the Debye-Waller factors (f-factors, Mössbauer fractions, or recoilfree fractions) can be obtained. Since inequivalent Au sites can be distinguished in the Mössbauer spectra of metal cluster compounds, the Debye-Waller factors of these sites can be investigated separately. These possibilities appear to be of importance in connection with the problem of the size-dependent phonon spectra of very small metal particles. Recently, we have reported a temperature dependent Mössbauer study of  $\text{Au}_{55}(\text{PPh}_3)_{12}\text{Cl}_6$  [12]. We pointed out the importance of the vibrations of the particles as a whole on the overall intensity of the Mössbauer spectra. These inter-cluster vibrations come in addition to the intra-cluster vibrations which affect the Debye-Waller factors of the four distinguishable Au sites of the metal core differently. In this chapter we will set up a mathematical framework (section 5.2) for calculating the intra-cluster vibrations. In order to investigate the dependence on cluster size, the experiments have been extended to the smaller Au clusters  $[\text{Au}_9(\text{PPh}_3)_8](\text{NO}_3)_3$  and  $\text{Au}_{11}(\text{PPh}_3)_7(\text{SCN})_3$ , of which the syntheses and the structures are described in section 5.3. The Mössbauer data and some experimental details can be found in section 5.4. On the basis of the isomer shifts (I.S.) and the quadrupole splittings (Q.S.), that are discussed in section 5.5, the subspectra are assigned to the different Au sites. The Debye-Waller factors are successfully described by the model for the inter- and intra-cluster vibrations (section 5.6). With the same model the specific heat (section 5.7) can be calculated without any adjustable parameters. The results are found to compare very well indeed with the experiments. In section 5.8 other related experiments will be compared to the present results. Some words will be spent on the microscopic geometries that determine both the differences in Debye-Waller factors and the directional anisotropies in the vibrations, in particular for the surface sites.

## 5.2 Cluster Vibrations

In this section we will consider the mathematical framework in which the vibrations of the clusters can be calculated. The sizes of the metal clusters are sufficiently small to use a simple, brute force method to calculate the normal modes. From these normal modes and their corresponding energies, both the specific heat and the Mössbauer fraction can be determined.

In the following, we will consider small vibrations and will describe them using classical mechanics [13]. It is convenient to introduce mass-weighted cartesian displacement coordinates

$$q_i = \sqrt{m_i} \delta x_i, \quad i = 1, \dots, 3N, \quad (5.1)$$

where  $N$  is the number of particles per cluster. The kinetic and potential energy

can then be written as

$$2U = \sum_{i=1}^{3N} \left( \frac{dq_i}{dt} \right)^2, \quad (5.2)$$

$$\begin{aligned} 2V &= 2V_0 + 2 \sum_{i=1}^{3N} \left( \frac{dV}{dq_i} \right)_0 q_i + \sum_{i,j=1}^{3N} \left( \frac{d^2V}{dq_i dq_j} \right)_0 q_i q_j + \dots \\ &= 2V_0 + 2 \sum_{i=1}^{3N} F_i q_i + \sum_{i,j=1}^{3N} F_{ij} q_i q_j + \dots \\ &= \sum_{i,j=1}^{3N} F_{ij} q_i q_j. \end{aligned} \quad (5.3)$$

Here we have introduced the notation  $F_i$  and  $F_{ij}$  for the first and second derivatives of the potential energy,  $V_0$  is chosen to be zero, terms higher than second order are neglected, and all  $q_i$ 's are zero in the equilibrium state. After substitution into the Newtonian equations of motion, one obtains

$$\frac{d^2 q_j}{dt^2} + \sum_{i=1}^{3N} F_{ij} q_i = 0, \quad j = 1, \dots, 3N. \quad (5.4)$$

For this set of simultaneous second order linear differential equations we introduce as trial solutions

$$q_i = A_i \cos(\Omega t + \phi). \quad (5.5)$$

The set of algebraic equations, obtained after substitution, can be written as an eigenvalue problem

$$\sum_{j=1}^{3N} F_{ij} A_{jk} = \Omega_k^2 A_{ik}, \quad k = 1, \dots, 3N, \quad (5.6)$$

with eigenvalues  $\Omega_k^2$  and normalized eigenvectors  $\vec{A}_k$ . In practice we will calculate the  $3N \times 3N$  matrix elements  $F_{ij}$  and solve the eigenvalue problem (5.6) numerically. The general solution for  $q_i$  can then be given by a linear combination of normal modes

$$q_i = \sum_{k=1}^{3N} A_{ik} K_k \cos(\Omega_k t + \phi_k), \quad i = 1, \dots, 3N, \quad (5.7)$$

where the constants  $K_k$  and  $\phi_k$  are determined by the initial conditions.

Since only intra-cluster interactions are included in the potential, six of the  $3N$  eigenvalues are zero. They represent the three translational and the three rotational degrees of freedom of the entire cluster. We will refer to them as inter-cluster vibrations and discuss them separately. The other  $(3N - 6)$  normal modes will be referred to as intra-cluster vibrations.

The mathematical description as given above does not specify yet the kind of interaction between the atoms, nor whether only nearest neighbour or also longer range interactions are to be taken into account. We will assume an ideal massless

spring between nearest neighbours, representing the stretching forces. This simple approach, which neglects bond bending forces, appears to be reasonable in cluster compounds, since the atoms are bound in a three-dimensional structure, albeit of small dimension. A comparison of different potentials by J.J. Burton [14] leads to the conclusion that the main features of the phonon spectra resulting from different types of interactions are in fact quite similar.

The energy of the vibrations is quantized by the standard equation [15]

$$\epsilon_k = (n_k + \frac{1}{2}) \hbar \Omega_k, \quad (5.8)$$

where  $n_k$  is the occupation number of the normal mode with energy  $\Omega_k$ . The thermal average of the occupation number is given by the Planck's distribution

$$\langle n_k \rangle = \frac{1}{\exp(\hbar \Omega_k / k_B T) - 1}. \quad (5.9)$$

From the energies of the normal modes and the thermal average of the occupation of each mode one obtains for the specific heat

$$C = R \sum_{k=1}^{3N-6} \frac{(\hbar \Omega_k / k_B T)^2 \exp(\hbar \Omega_k / k_B T)}{(\exp(\hbar \Omega_k / k_B T) - 1)^2}. \quad (5.10)$$

The summation limits reflect the presence of only  $3N - 6$  normal modes for the intra-cluster vibrational specific heat. The specific heat in the classical or high temperature limit will therefore be equal to  $(3N - 6)R$ . From the eigenvalues and the eigenvectors, as obtained from the normal modes, also the Mössbauer fractions for the different sites in the cluster can be calculated. We start from equation 2.6 which gives for the Mössbauer fraction  $f_i(T)$  at site  $i$

$$f_i(T) = \exp\left\{\frac{-\hbar}{2m_i N} \sum_{k=1}^{3N-6} \frac{(\vec{\mu}, \vec{u}_{ik})^2}{\Omega_k} \left(1 + \frac{2}{\exp(\hbar \Omega_k / k_B T) - 1}\right)\right\}, \quad (5.11)$$

where  $\vec{\mu}$  is the wave vector of the  $\gamma$ -ray,  $\vec{u}_{ik}$  is the amplitude of the displacement of an atom at site  $i$  from equilibrium due to normal mode  $k$ ,  $m_i$  is the mass of an atom at site  $i$ , and  $N$  is the number of atoms per cluster. Again only the intra-cluster vibrations have been taken into account, and the inter-cluster vibrations will be treated separately. Since we are dealing with powder samples, the inner product in equation 5.11 can be integrated over the spherical coordinates  $\theta$  and  $\phi$ , yielding  $\frac{1}{3} \vec{u}_{ik}^2 \vec{\mu}^2$ . Here  $\vec{\mu}$  can be replaced by  $E_\gamma / \hbar c$ , where  $E_\gamma$  is the energy of the  $\gamma$ -ray and  $c$  the velocity of light. Furthermore we can replace  $\vec{u}_{ik}$  by the elements of the normalized eigenvector that corresponds to site  $i$ . The normalization of  $\vec{A}_k$  corrects for the factor  $N$  appearing in formula (5.11) which then results in

$$f_i(T) = \exp\left\{\frac{-E_\gamma^2}{6m_i c^2} \sum_{k=1}^{3N-6} \sum_{j=3i+1}^{3i+3} \frac{A_{jk}^2}{\hbar \Omega_k} \left(1 + \frac{2}{\exp(\hbar \Omega_k / k_B T) - 1}\right)\right\}. \quad (5.12)$$

This formula makes it possible to investigate the Debye-Waller factors of each distinct site in small clusters. In section 5.8 we will see how this factor depends on

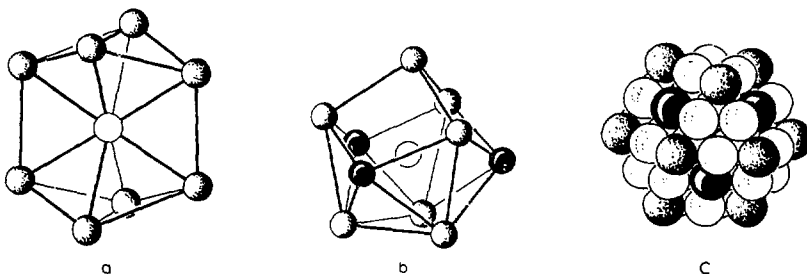


Figure 5.1: A schematic representation of the structures of the  $\text{Au}_9$  (a),  $\text{Au}_{11}$  (b) and the  $\text{Au}_{55}$  (c) cluster, with the bonding ligands removed. The P bonded gold surface atoms are the gray spheres, while the Cl or SCN bonded gold atoms are the black spheres. The unbonded gold surface atoms are slightly shaded and the inner-core atoms are blank.

cluster size and coordination number. In section 5.6 and 5.7 we will compare the calculations of the Mössbauer fractions and the specific heat with experimental data on the metal cluster compounds  $[\text{Au}_9(\text{PPh}_3)_8](\text{NO}_3)_3$ ,  $\text{Au}_{11}(\text{PPh}_3)_7(\text{SCN})_3$ , and  $\text{Au}_{55}(\text{PPh}_3)_{12}\text{Cl}_6$ .

We will treat the vibrations of the center of mass of the clusters in a Debye scheme. This means that we assume that the density of states is proportional to the corresponding energy squared. In the crystalline  $[\text{Au}_9(\text{PPh}_3)_8](\text{NO}_3)_3$  and  $\text{Au}_{11}(\text{PPh}_3)_7(\text{SCN})_3$  compounds this seems a reasonable assumption, as long as the phonon wavelength exceeds the inter-cluster distance. For  $\text{Au}_{55}(\text{PPh}_3)_{12}\text{Cl}_6$ , which is amorphous, the justification must be sought in the fact that, also in amorphous systems and glasses at long phonon wavelengths, a density of states is found, which is proportional to the phonon energy squared [16,17]. This is plausible since for sufficiently large wavelength both crystalline and non-crystalline materials can be seen as a continuous medium.

### 5.3 Metal Cluster Compounds

Three metal cluster compounds have been investigated,  $[\text{Au}_9(\text{PPh}_3)_8](\text{NO}_3)_3$ ,  $\text{Au}_{11}(\text{PPh}_3)_7(\text{SCN})_3$ , and  $\text{Au}_{55}(\text{PPh}_3)_{12}\text{Cl}_6$ . They are all chemically stable at room temperature and are not air sensitive. They will be denoted by  $\text{Au}_9$ ,  $\text{Au}_{11}$ , and  $\text{Au}_{55}$  in what follows.

The  $[\text{Au}_9(\text{PPh}_3)_8]^{3+}(\text{NO}_3^-)_3$  cluster compound was prepared<sup>1</sup> by means of the reduction of  $\text{AuPPh}_3\text{NO}_3$  using  $\text{NaBH}_4$  in alcohol [18]. The crystal structure of  $[\text{Au}_9(\text{P}(p\text{-MeC}_6\text{H}_4)_3)_8](\text{PF}_6)_3$  is given by Bellon et al. [19]. A sketch of the metal core of  $\text{Au}_9$  can be found in fig. 5.1a. The central gold atom is bonded to eight peripheral gold atoms. Three mutually perpendicular two-fold symmetry axes, as found by Bellon et al., leave only two inequivalent surface Au sites that are both

<sup>1</sup>Prepared by the Anorganic Chemistry group of Prof. Dr. J.J. Steggerda and Dr. J.J. Bour of the Katholieke Universiteit te Nijmegen.



bonded to a PPh<sub>3</sub> ligand. The radial Au-Au distances in the metal core vary from 2.68 to 2.72 Å, whereas these between two peripheral Au atoms are between 2.75 and 2.86 Å. The three NO<sub>3</sub><sup>-</sup> counter ions per formula unit appear to be rather disordered [19].

The second metal cluster compound, Au<sub>11</sub>(PPh<sub>3</sub>)<sub>7</sub>(SCN)<sub>3</sub>, has been prepared<sup>1</sup> using the same reduction method [20] as for Au<sub>9</sub>. Preliminary results of its crystal structure determination, as well as the complete crystal structure of Au<sub>11</sub>(P(p-FC<sub>6</sub>H<sub>4</sub>)<sub>3</sub>)<sub>7</sub>I<sub>3</sub> have been reported [21,22]. A sketch of the metal core of the latter compound is shown in fig. 5.1b. The three-fold symmetry axis running through the top and center Au atom (see fig. 5.1b) leaves five different gold sites. One site is the center gold atom, another the SCN bonded surface site, and further, three crystallographically different sites are bonded to a PPh<sub>3</sub> ligand. The ten radial Au-Au distances are found in the range of 2.60 to 2.71 Å. The peripheral bond lengths are in between 2.84 and 3.19 Å.

The Au metal cluster compound with the largest nuclearity number known until now, is Au<sub>55</sub>(PPh<sub>3</sub>)<sub>12</sub>Cl<sub>6</sub>. The preparation<sup>2</sup> is by means of reduction of (C<sub>6</sub>H<sub>5</sub>)<sub>3</sub>PAuCl with B<sub>2</sub>H<sub>6</sub> in benzene [5]. The cuboctahedral structure proposed [5] for the metal core in Au<sub>55</sub>(PPh<sub>3</sub>)<sub>12</sub>Cl<sub>6</sub> and shown in fig. 5.1c, has only 5 distinct gold sites, because of its high symmetry. The central gold atom and the 12 gold atoms in the first shell, although strictly speaking occupying different sites, have the same nearest neighbour coordination. These 13 atoms will be referred to as inner-core atoms. Six surface sites at the center of a square face are bonded to a chlorine ion outside the metal core, 12 corner sites are bonded to the phosphorous ion of a PPh<sub>3</sub> ligand, and 24 gold surface atoms are not bonded to a ligand and are located in edge positions. The latter atoms will be referred to as unbonded surface atoms in what follows. Based on the atomic radius of gold, the "diameter" of the metal core is roughly 15 Å. The structure has been confirmed by high resolution electron microscopy [23]. Due to the lack of single crystals, no X-ray study could be made and therefore the bond lengths are unfortunately still unknown. In contrast to the two crystalline metal cluster compounds described above, Au<sub>55</sub> forms an amorphous solid.

## 5.4 Mössbauer Results

The spectra of Au<sub>9</sub>, Au<sub>11</sub> and Au<sub>55</sub> cluster compounds are fitted by means of the transmission integral method, since the relative thickness of the absorbers leads to sizable line broadening and the resonance lines in the spectra overlap considerably (see section 2.6). The fit procedure was as follows. First the spectra taken at 4.2 K, which have a very good signal to noise ratio, were analysed with the smallest number of subspectra that still produced an acceptable fit. The subspectra were assigned to the inequivalent gold sites of the cluster compound. Subsequently the spectra measured at higher temperatures were analysed. In these refinements, the

<sup>2</sup>Au<sub>55</sub> is prepared by the Coordination Chemistry group of Prof. Dr. G. Schmid of the Universität Essen.

Table 5.1: The I.S. (relative to Au in Pt at 4.2K) and the Q.S. in mm/s for the different Au-sites. The values with an asterisk were constrained during the refinement.

	Au <sub>9</sub>		Au <sub>11</sub>		Au <sub>55</sub>	
	I.S.	Q.S.	I.S.	Q.S.	I.S.	Q.S.
Au core			2.5	0.0*	-1.4	0.0*
Au unb.surf.					0.3	1.4
Au-SCN			0.8	4.6		
Au-Cl					0.1	4.4
Au-PPh <sub>3</sub> a	2.1	7.0	1.3	7.6	0.6	7.1
b	2.2	5.7	1.3	6.2		

peak positions as found in the 4.2 K spectra were fixed and only the intensity ratios of the subspectra were adjusted.

i) Au<sub>9</sub>

Mössbauer spectra of [Au<sub>9</sub>(PPh<sub>3</sub>)<sub>8</sub>](NO<sub>3</sub>)<sub>3</sub>, taken at five different temperatures between 4.2 and 20 K, are shown in fig. 5.2a. The spectrum at 4.2 K is similar to the one measured by Vollenbroek [24]. For Au<sub>9</sub> the transmission integral method indicates the presence of at least two doublets instead of one as would have been conducted from first sight inspection of the spectrum. However, we are not able to assign the doublets to the three crystallographically distinct Au sites. The intensity ratio of the two doublets is close to one, making it impossible to assign one of them to the central Au atom. For the discussion of the intensities of the resonance lines, the contributions of the doublets will be added. The total will be assumed to be the average contribution of all the gold sites in the metal cluster core. The values obtained for the isomer shift (I.S.) and the quadrupole splitting (Q.S.) can be found in table 5.1. It should be noted that the contribution of the central Au atom apparently has Mössbauer parameters comparable to those of the peripheral Au atoms, since it is not observed separately.

ii) Au<sub>11</sub>

The spectra of Au<sub>11</sub>(PPh<sub>3</sub>)<sub>7</sub>(SCN)<sub>3</sub>, taken at the same temperatures as the spectra of Au<sub>9</sub>, are shown in fig. 5.2b. The spectrum at 4.2 K is similar to the one reported by Vollenbroek [25]. The spectra can be fitted by three doublets and one singlet. The fifth subspectrum that is to be expected on basis of the X-ray data is not observed, probably because of its low intensity. The singlet is assigned to the central gold atom on basis of symmetry considerations. The doublet with the smallest Q.S. is identified with the Au site bonded to the SCN ligand. The doublets with a Q.S. close to 7 mm/s correspond to PPh<sub>3</sub> bonded Au sites. These assignments are based on the work of Vollenbroek [25], who compared various Mössbauer spectra of Au<sub>11</sub>(PPh<sub>3</sub>)<sub>7</sub>X<sub>3</sub>, with X=CN, SCN, and I. They were fitted by three subspectra two of which, a singlet and a doublet with a Q.S. of about 7 mm/s, were nearly independent of X. As in the case of Au<sub>9</sub>, we are unable

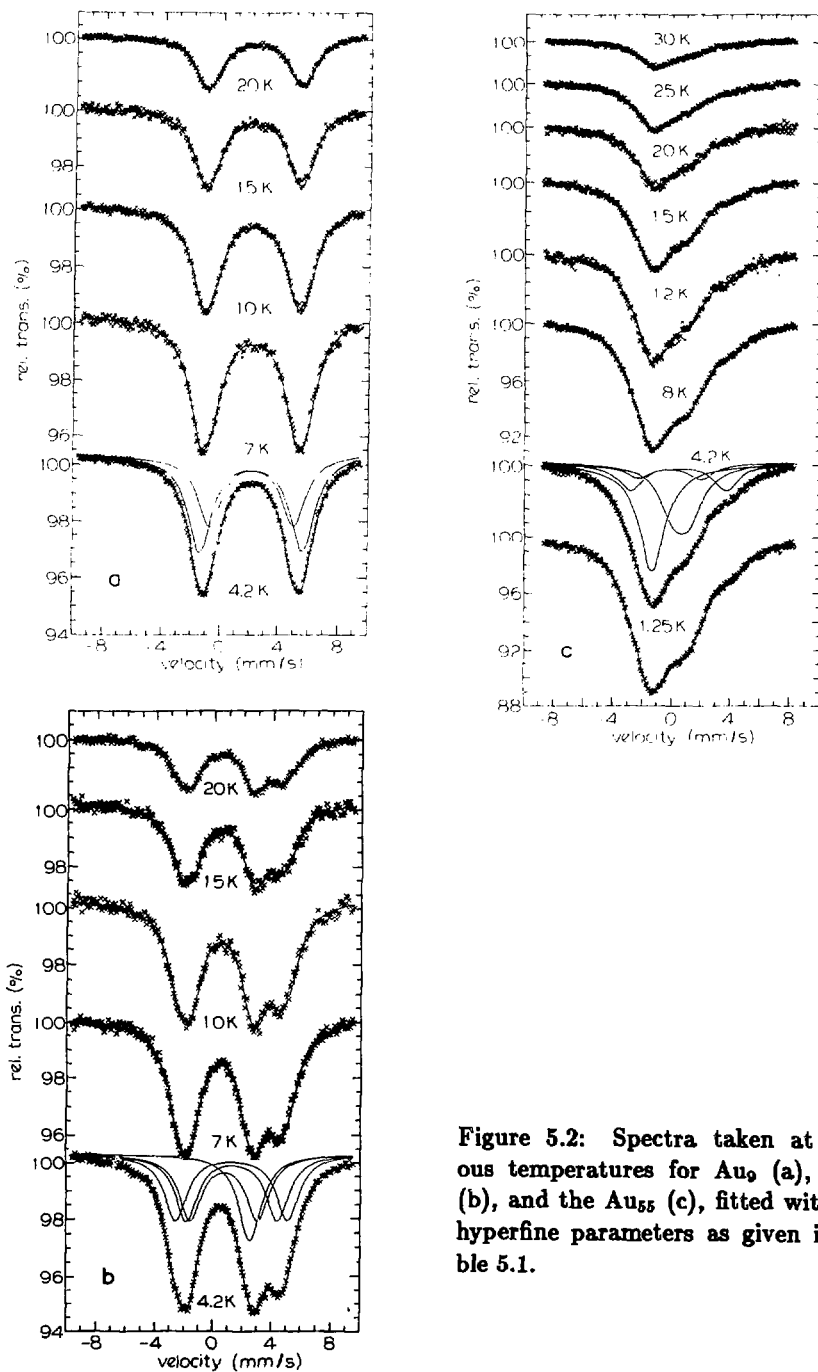


Figure 5.2: Spectra taken at various temperatures for  $\text{Au}_9$  (a),  $\text{Au}_{11}$  (b), and the  $\text{Au}_{55}$  (c), fitted with the hyperfine parameters as given in table 5.1.

to assign the two doublets with largest Q.S. to different  $\text{PPh}_3$  coordinated sites, and we will, therefore, add their intensities in the discussion of the Debye-Waller factors. The Mössbauer parameters can be found in table 5.1.

### iii) $\text{Au}_{55}$

In fig. 5.2c we show the spectra of  $\text{Au}_{55}(\text{PPh}_3)_{12}\text{Cl}_6$ , obtained in the temperature range of 1.25 to 30 K. The 4.2 K spectrum is identical to that measured earlier by Schmid et al. [5] at the same temperature. The spectrum is fitted by means of the transmission integral method using a singlet and three doublets.

The singlet is assigned to the 13 inner-core atoms on basis of symmetry considerations. Again a subspectrum with a Q.S. of about 7 mm/s was found and identified with the twelve Au sites coordinated to  $\text{PPh}_3$  ligands. The doublet with a Q.S. close to 4 mm/s is typical for Cl bonded Au atoms, as was also observed in  $\text{AuCl}$  [26] and  $\text{Au}(\text{PPh}_3)_7\text{Cl}_2\text{PF}_6$  [27]. The remaining doublet, with the smallest Q.S. results from the 24 unbonded Au surface atoms. The Mössbauer parameters are given in table 5.1.

Schmid et al. assumed that the intensity ratios for the three types of surface Au atoms should be proportional to the relative site occupations, i.e. 1:2:4, and fixed this ratio in their fit procedure. They allowed a separate intensity variable for the 13 inner-core atoms, in effect choosing for a model with separate f-factors for surface and inner-core atoms. Using a Lorentzian line shape they obtained a good fit to their data at 4.2 K. However, the transmission integral method forced us to release the constraints on the relative intensities of the four different gold sites. For the same reason we had to refine the Q.S. parameter for the unbonded surface sites which was set to zero by Schmid et al. The deviations of the present M.E.S. parameters from those found by Schmid et al. may be attributed to the here discussed differences in the fit procedure.

## 5.5 Isomer Shift and Quadrupole Splitting

In this section we will first discuss the hybridization states commonly found for Au compounds, and examine how the electron structure of the gold atoms with the attached ligands affects the I.S. and Q.S. Subsequently these ideas will be applied to the Mössbauer parameters of the metal cluster compounds under investigation.

The Isomer Shift (I.S.) is a measure of the electron density at the resonant Mössbauer nucleus. This energy shift, finding its origin in the Coulomb interaction between electron and nucleus, is measured relative to the Mössbauer source. The largest contribution to the electron density at the nucleus, resulting from the inner s-electrons, is independent of the chemical environment, and, therefore, similar in source and absorber. In Au, the main contribution to the I.S. comes from the 6s electron density at the nucleus. The magnitude can be estimated as 8.0 mm/s per s-electron [28]. The electrons in the 6p valence orbital have only a small influence on the I.S., since their screening effect on the s-electrons is nearly completely cancelled by their relativistic density at the nucleus. The 5d valence electrons, on the other hand, have a net screening effect which is roughly equal to -1.6 mm/s per d-electron

[28].

The electron configuration of atomic gold is  $[\text{Xe } 4f^{14} 5d^{10} 6s^1]$ . In Au complexes, the two most common hybridization states are  $\text{Au}_{\text{lin}}^{\text{I}}$ , which hybridizes linearly with two ligands L as  $\text{AuL}_2$ , and  $\text{Au}_{\text{pl}}^{\text{III}}$ , which has a planar  $\text{AuL}_4$  geometry. In  $\text{Au}_{\text{lin}}^{\text{I}}$ ,  $\sigma$ -bonding involves the Au atomic orbitals  $5d_{x^2}$ ,  $6s$ , and  $6p_x$ . The  $5d_{xy}$ ,  $5d_{yz}$ ,  $6p_x$ , and  $6p_y$  orbitals are the basis for the  $\pi$ -bonds. From this it can be inferred that in the case of  $\text{Au}_{\text{lin}}^{\text{I}}$  the electron density at the gold nucleus can change by  $\sigma$ -electron donation or acceptance by the surrounding ligands. A strong  $\sigma$ -donating ligand will enhance the s-electron density at the Au nucleus, and increase the I.S. This dominates the screening effect of the occupation of the  $5d_{x^2}$  orbital on the I.S. A  $\pi$ -electron donating ligand will increase the p- and the d-electron density at the gold atom, and at the same time decrease the I.S.

In auric  $\text{Au}_{\text{pl}}^{\text{III}}$  compounds, the atomic orbitals  $6s$ ,  $6p_x$ ,  $6p_y$ , and  $5d_{x^2-y^2}$  are the basis for the  $\sigma$ -bonding. The  $\pi$ -bonds are built up from the  $6p_x$  and  $5d_{xy}$  orbitals. Evidently, the same arguments as for  $\text{Au}_{\text{lin}}^{\text{I}}$  can be applied to conclude that  $\pi$ -donating and  $\sigma$ -accepting ligands will increase the I.S. for  $\text{Au}_{\text{pl}}^{\text{III}}$  compounds. In Au complexes usually the changes in I.S. due to  $\sigma$ -electron donation (acceptance) and  $\pi$ -electron acceptance (donation) are simultaneously present, since the covalency of the Au compounds implies a small net charge transfer.

The I.S. may also be affected by external pressure. Both in  $\text{Au}_{\text{lin}}^{\text{I}}$  and  $\text{Au}_{\text{pl}}^{\text{III}}$  compounds the enhanced metal-ligand overlap increases the  $\sigma$ -electron donation and  $\pi$ -electron acceptance by the ligand. An increase of the I.S. is then evident. In gold metal external pressure or pressure due to surface tension will decrease the atomic volume, and therefore increase the  $6s$  electron density and the I.S. A quantitative estimate is given by Williamson [28], who gives  $\delta \text{I.S.} / \delta \ln V = -6.8 (\pm 1.0) \text{ mm/s}$ .

The quadrupole splitting (Q.S) arises from a non-spherical charge distribution around the nucleus. One can distinguish two contributions. The first is the lattice contribution, arising from a non-spherical charge distribution of the surrounding atoms. This will be very small in gold complexes, since they are highly covalent and are subject to the Pauling neutrality principle [28,29]. The second and main contribution to the Q.S. originates from the valence electrons. The total Q.S. can be estimated from the occupations of the valence orbitals  $5d_i$  and  $6p_i$ , and the maximum contribution that each of these atomic orbitals contributes to the Q.S., as can be found e.g. in ref. [28]. In the case of a fully occupied  $5d$  orbital, the total contribution equals zero as expected, since the charge distribution is then spherical.

Since the I.S. values of both  $\text{Au}_{\text{lin}}^{\text{I}}$  and  $\text{Au}_{\text{pl}}^{\text{III}}$  vary between 0.0 and 6.0 mm/s, the I.S. of a Au site alone does not identify its hybridization state. However, the combination of I.S. and Q.S., usually gives enough information to determine the hybridization state, as can be seen from the compilation of data for different Au compounds in the Q.S. versus I.S. plot (see fig. 5.3). The data for the two states are covered by two shaded areas and show a clear correlation between I.S. and Q.S. For  $\text{Au}_{\text{lin}}^{\text{I}}$  this can be understood easily, since the  $\sigma$ -bonding orbitals  $5d_{x^2}$  and  $6p_x$  contribute negatively to the Q.S. [28], whereas the  $\pi$ -bonding orbitals,  $5d_{xy}$ ,  $5d_{yz}$ ,  $6p_x$ , and  $6p_y$  contribute positively. The stronger  $\sigma$ -donor and  $\pi$ -acceptor the ligand

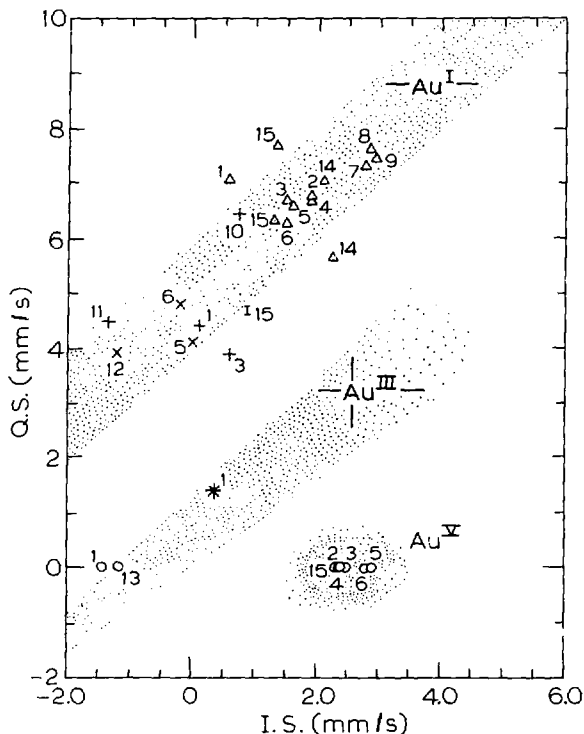


Figure 5.3: Q.S. versus I.S. for gold clusters and related compounds, taken from ref. [24,26,30]. The Au<sup>I</sup> and Au<sup>III</sup> regions are indicated. Core Au atoms are shown by (o), I bonded Au by (x), Cl bonded Au by (+), PPh<sub>3</sub> bonded Au by (Δ), the SCN bonded Au by (I), and the unbonded surface atom by (\*). 1: Au<sub>55</sub>(PPh<sub>3</sub>)<sub>12</sub>Cl<sub>6</sub>, 2: Au<sub>9</sub>(PPh<sub>3</sub>)<sub>8</sub>(SCN)<sub>3</sub>, 3: Au<sub>11</sub>(PPh<sub>3</sub>)<sub>8</sub>Cl<sub>2</sub>PF<sub>6</sub>, 4: Au<sub>8</sub>(PPh<sub>3</sub>)<sub>8</sub><sup>2+</sup>, 5: Au<sub>11</sub>(PPh<sub>3</sub>)<sub>7</sub>I<sub>3</sub>, 6: Au<sub>11</sub>(PPh<sub>3</sub>)<sub>6</sub>(CN-*i*-Pr)I<sub>3</sub>, 7: PPh<sub>3</sub>AuI, 8: PPh<sub>3</sub>AuSCN, 9: PPh<sub>3</sub>AuCl, 10: ClAuCl<sup>-</sup>, 11: AuCl, 12: AuI, 13: Au metal, 14: Au<sub>9</sub>(PPh<sub>3</sub>)<sub>8</sub>(NO<sub>3</sub>)<sub>3</sub>, 15: Au<sub>11</sub>(PPh<sub>3</sub>)<sub>7</sub>(SCN)<sub>3</sub>.

is, the larger the I.S. and the more negative the Q.S. A negative Q.S. for  $Au_{in}^I$  is confirmed experimentally by Prosser et al. [31], who did Mössbauer measurements on a single crystal of  $KAu(CN)_2$ . The situation in  $Au_{pl}^{III}$  is not so transparent, and will not be discussed here.

In metal cluster compounds the valence electrons of the metal atoms and of the coordinating ligands are delocalized over the cluster. For small Au clusters the number of valence electrons allows molecular orbital (M.O.) calculations [32,33]. Unfortunately, the huge number of valence electrons makes M.O. calculations impractical to perform for the  $Au_{55}$ , even if the ligands are discarded. However, the hybridization states  $Au_{in}^I$  and  $Au_{pl}^{III}$  discussed above illustrate how one can make qualitative suggestions about the size of the I.S. and Q.S., based on the separate contributions of the atomic orbitals. It also turns out that the experimental M.E.S. parameters of some Au sites in the metal cluster compounds is comparable to the linear  $Au^I$  or the planar  $Au^{III}$  hybridization.

Fig. 5.3 shows that the surface sites of  $Au_9$ ,  $Au_{11}$ , and  $Au_{55}$ , which are coordinated to a ligand (Cl,  $PPh_3$ , or SCN), have M.E.S. parameters that fall in the region characteristic for the  $Au_{in}^I$  hybridization state. This leads to the suggestion that these surface Au atoms have an occupation of the gold valence orbitals comparable to the hybridization state  $Au_{in}^I$ . This linear hybridization of the Au atoms is most probably directed towards the strongly bonding ligands, and may be understood from the consideration that bond force constants larger than 200 N/m are found between Au and the ligands [34], whereas force constants of the order of 30 N/m are found between the Au atoms (see table 5.2 in section 5.6). The Q.S. values are comparable to those of related compounds, in which Au is coordinated to the same ligands. Illustrative examples, like AuCl and  $PPh_3AuX$ , with  $X=I, Cl$ , and SCN are included in fig. 5.3. Note that in the latter compound the Q.S. is mainly determined by the  $PPh_3$  groups and nearly independent of X. The unbonded surface atoms of the  $Au_{55}$  cluster compound lack this polarizing ligand and show I.S. and Q.S. values that can best be compared to  $Au_{pl}^{III}$ . This may indicate that the overlap towards the four neighbour surface sites is predominant and mainly determine the electronic structure. Whatever the exact electronic structure may be, the 5d atomic orbital is not completely occupied, since the I.S. is too high for a  $Au_{in}^I$  hybridization state. The Q.S. is not zero due to the fact that the charge distribution around the nucleus is far from spherical. It will mainly result from the difference in occupation of the  $6p_i$  orbitals [32] and also of the  $5d_i$  orbitals, since the latter are not completely occupied. It is clear from fig. 5.3 that the I.S. of the central atom of  $Au_{11}$  is almost identical to other single atom centered cluster compounds. The Mössbauer parameters of these single inner-core atoms do not seem to coincide with one of the two most common hybridization states of Au. Their I.S. value is very close to pentavalent  $Au^V$ . This uncommon oxidation state is found at gold sites with octahedral symmetry in compounds like  $CsAuF_6$  and  $X_2AuF_6$ , which have an I.S. of 2.4 and 2.3 mm/s respectively [35]. The Q.S. of all these compounds is zero, as can be expected from the symmetry. Compared to the I.S. of the 13 inner-core atoms of  $Au_{55}$  and metallic gold, the I.S. of the single atom centered

clusters is very large. This can be explained by the fact that, similar to pentavalent gold, the 5d shell only accommodates 6 electrons, and therefore has a much lower shielding effect on the 6s electrons. Quantitatively, if the four 5d electrons would be completely ionized, we would estimate [28] the difference as 6.4 mm/s instead of the experimental value of 4.2 mm/s. Although it is unlikely that the electronic structure of the central Au atoms with eight or ten Au nearest neighbours is exactly the same as for Au<sup>V</sup> with octahedral symmetry, the comparison leads to the conclusion that the 5d electrons also play an important role in the bonding of the inner-core atoms to its surrounding Au atoms. M.O. calculations should be able to further elucidate this point.

The gold atoms in the inner-core of Au<sub>55</sub>, on the other hand, show an I.S. and Q.S. that are very close to gold metal. Most probably, therefore, the electronic structure of these inner-core atoms is already comparable to that of Au atoms in bulk metal, for which it is known that the chemical bonding is mainly provided by the 6s valence electrons. Since the inner-core atoms have a Q.S. equal to zero, we may conclude that the charge distribution of the valence electrons as seen by the resonant nuclei is spherical. Actually the I.S. of the inner-core atoms is slightly more negative than that of bulk gold. An explanation may be that the Au-Au bonds in the Au<sub>55</sub> are longer than in bulk gold, giving rise to a decrease in the 6s electron density at the nucleus. X-ray data on Au<sub>55</sub> unfortunately are not available. The surface tension that decreases bond lengths in gold micro-crystals appears not to be effective in metal clusters which are surrounded by ligands. This may be concluded from X-ray data on the smaller gold cluster compounds. These show that the bond lengths depend strongly on the exact geometry. The bond lengths are comparable to bulk Au, and do not show a clear trend towards smaller or larger values. Therefore, it is improbable that the bond distances in Au<sub>55</sub> would differ much from those in bulk gold, but we cannot decide at present whether they would be slightly larger or smaller. As another possible explanation we point out that the delocalization of the Au valence electrons could be extended over the coordinating ligands, which share in the M.O. Evidently, the degree of delocalization of the valence electrons over the ligands depends strongly on their electronegativity. This seems to be comparable to the delocalization of the valence band electrons of small Pt particles (from 10 to 300 Å) over the chemisorbed CO molecules reported by Rudaz [36], who observed a Korringa relation for the spin-lattice relaxation in a <sup>13</sup>C N.M.R. study.

From fig. 5.3 one may note a successively decreasing I.S. for the PPh<sub>3</sub> bonded Au surface sites in the order Au<sub>1</sub>, Au<sub>9</sub>, Au<sub>11</sub>, and Au<sub>55</sub>. Since these atoms are supposed to be hybridized as Au<sub>inn</sub><sup>1</sup>, this would imply that the 6s electron density shows a decreasing trend with increasing particle size. A similar conclusion was reached by Parish [37], who studied Au-Ru clusters compounds by means of <sup>197</sup>Au M.E.S. A single argument that explains this trend is difficult to give, since apart from the cluster size other quantities like the geometry and the charge of the cluster complex are not identical.

In most single centered metal cluster compounds like [Au<sub>8</sub>(PPh<sub>3</sub>)<sub>8</sub>]<sup>2+</sup>, [Au<sub>9</sub>(PPh<sub>3</sub>)<sub>8</sub>]<sup>+</sup>, Au<sub>11</sub>(PPh<sub>3</sub>)<sub>7</sub>X<sub>3</sub>, and [Au<sub>11</sub>(PPh<sub>3</sub>)<sub>8</sub>X<sub>2</sub>]<sup>+</sup> the central atom shows



a singlet in the M.E.S. spectrum. The zero quadrupole splitting has been ascribed to the cubic-like symmetry of these sites. It is therefore surprising that the  $[\text{Au}_9(\text{PPh}_3)_8]^{3+}$  (and the related complex  $[\text{Au}_8(\text{PPh}_3)_7]^{2+}$ ) do not show a separate signal for the central Au atom. Van der Velden et al. [32] have performed extended Hückel molecular orbital calculations on the metal core of small Au clusters with nuclearities between 2 and 13. According to these calculations it is the difference in occupation of the three  $6p_i$  atomic orbitals, which form a part of the basis of the M.O., that mainly accounts for the Q.S. The clusters that show a single resonance line for the central atom indeed gave a nearly equal population of the three  $6p_i$  orbitals, whereas  $[\text{Au}_9(\text{PPh}_3)_8]^{3+}$  (and  $[\text{Au}_8(\text{PPh}_3)_7]^{2+}$ ) gave a substantial difference in occupation.

## 5.6 Debye-Waller Factors

From fig. 5.2, which shows the spectra of the cluster compounds as a function of temperature, the following three features can be noticed. The first is the *drastic decrease in the absorption intensities* for all three metal cluster compounds as the temperature is increased. The second is that there is *no visual change in the shape of the spectra* as a function of temperature, and finally the intensity ratios found do not correspond to the relative occupancy ratios, giving different absolute f-factors for the different sites. The results for the absolute Debye-Waller factors for each gold site, as obtained from the fits and the relative site occupations, are plotted in fig. 5.4 versus temperature. The difference in f-factors of the Au sites is related to the intra-cluster vibrations and results from a difference in bonding stiffness for each Au site. However, the shape of the spectra in fig. 5.2 is identical over the whole temperature range, indicating that the intra-cluster vibrations do not change the relative intensity ratios of the different Au sites over the measured temperature range. By contrast, the total intensity of the spectrum decreases drastically. This must therefore result from the centre of mass vibrations of the clusters, referred to as inter-cluster vibrations.

Assuming that the inter- and intra-cluster vibrations are decoupled we can write

$$\langle x^2 \rangle_{\text{tot}} = \langle x^2 \rangle_{\text{inter}} + \langle x^2 \rangle_{\text{intra}}, \quad (5.13)$$

where  $\langle x^2 \rangle$  is the mean squared vibrational amplitude. This means that we can simply multiply the f-factors for the inter- and intra-cluster vibrations

$$f_a = f_a^{\text{inter}} \times f_a^{\text{intra}}, \quad (5.14)$$

where  $f_a^{\text{intra}}$  can be calculated by solving the eigenvalue problem of the intra-cluster vibrations (equation 5.6) and plugging the results into formula 5.12. The only free parameter is the force constant between nearest neighbour gold atoms. In  $\text{Au}_{55}$  the Au atoms are in a cuboctahedral close-packing geometry, and we have assumed that the bond lengths are all the same. Moreover, since no X-ray data are present for this cluster compound, we were left with no alternative.  $\text{Au}_9$  and  $\text{Au}_{11}$ , on

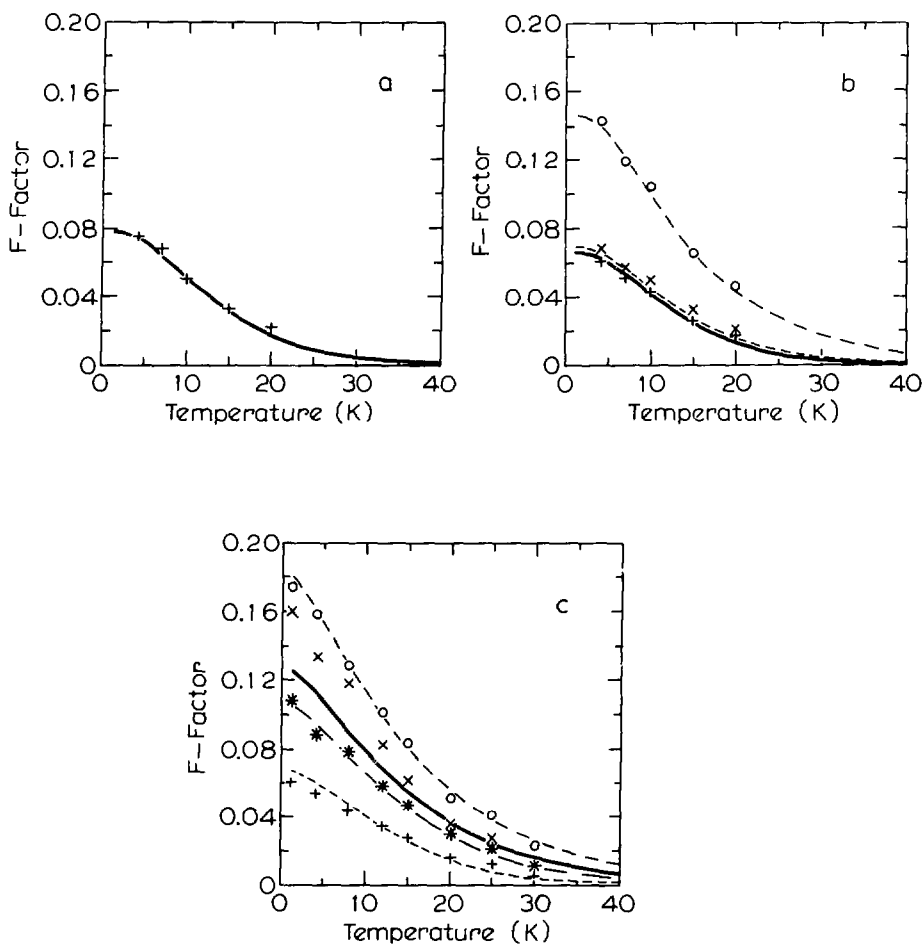


**Figure 5.4:** The temperature dependence of the Mössbauer fraction of the distinguishable gold sites of Au<sub>9</sub> (a), Au<sub>11</sub> (b), and Au<sub>55</sub> (c); (o) core, (x) Cl bonded, (\*) unbonded surface, and (+) PPh<sub>3</sub> bonded Au atoms. The fits shown by the solid lines are discussed in the text.

Table 5.2: The Debye temperature used to fit the inter-cluster vibrations and the force constant  $F_{ij}$  at 2.88 Å with which the intra-cluster vibrations are calculated.

	Au <sub>9</sub>	Au <sub>11</sub>	Au <sub>55</sub>
$F_{ij}$ (N/m)	16 (2)	21 (2)	30 (2)
$\theta_D$ (K)	25 (3)	25 (3)	15 (1)

the other hand, show a geometry that is far from close-packed. And since X-ray data on comparable complexes are available, we have modified the force constants with the sixth power of the inter-atomic distance as suggested by Gans [38]. The inter-cluster vibrations will be calculated using the basic Debye scheme (see section 2.4)

$$f_a^{inter} = \exp\left\{\frac{-3E_\gamma^2}{4Mc^2k_B\theta_D}\left(1 + \frac{4T^2}{\theta_D^2}\int_0^{\theta_D/T}\frac{x dx}{\exp(x) - 1}\right)\right\} \quad (5.15)$$

where  $E_\gamma$  is the energy of the gamma rays,  $\theta_D$  is the Debye temperature corresponding to the cutoff frequency of the phonon density,  $k_B$  is the Boltzmann's constant,  $c$  the velocity of light, and  $M$  is the mass of the entire cluster. Clearly, the free parameter for the inter-cluster vibrations is the Debye temperature, and this was constrained to be equal for all the different gold sites of one particular cluster compound. Summarizing, the solid curves given in fig. 5.4 for each cluster compound are calculated with two adjustable parameters, the force constant for the intra-cluster vibrations and the Debye temperature for the inter-cluster degrees of freedom. The results for these parameters are given in table 5.2. The errors given between brackets in table 5.2 are of the order of ten percent. They result from the fact that absolute f-factors are difficult to determine. The check on the absolute f-factor determination by the measurement of a gold foil at 42 K, that gave an error of 5 % (see section 3.5), gives an indication of the experimental error. Moreover, the two parameters needed to calculate the curves in fig. 5.4 are (negatively) correlated, making a precise determination difficult. However, the curves fit the measurements quite accurately. Especially for the Au<sub>11</sub> and the Au<sub>55</sub> it is striking how well the model for the intra-cluster vibrations predicts the experimental ratio of Debye-Waller factors.

## 5.7 Specific Heat

In the previous section we have shown how the Mössbauer f-fraction is determined by the inter-cluster vibrations, which decrease the total intensity of the spectrum at low temperatures, and by the intra-cluster vibrations which mainly determine the relative intensity ratios of the subspectra. In this section we will use this model and the obtained parameters of table 5.2 to calculate the specific heat contribution of the metal cores.

The specific heat of the Au<sub>11</sub>(PPh<sub>3</sub>)<sub>7</sub>(SCN)<sub>3</sub> has been measured by the square wave excitation (SWEX) method [39] between 0.5 and 20 K. The main reason for

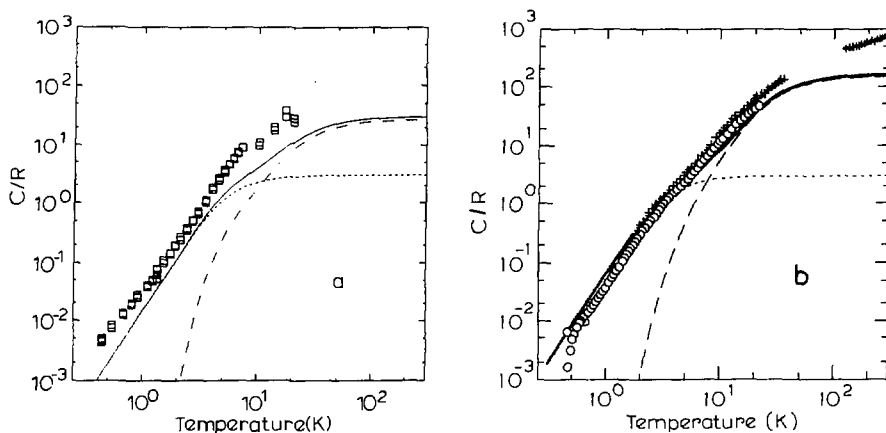


Figure 5.5: Specific heat of the Au<sub>11</sub> (a) and the Au<sub>55</sub> (b) cluster compound. The data shown by (+) was kindly provided by Gmelin. The fit (solid line) is the addition of the inter- (dotted line) and intra-cluster (broken line) vibrational contributions.

choosing this method was that only a small amount of material was available (60 mg or  $1.4 \cdot 10^{-5}$  mole). Heat capacities down to  $10^{-8}$  J/K can easily be determined at 0.5 K and are still larger than the contribution of the empty calorimeter ( $C_a$ ) by a substantial factor. The sample holder consists of a sapphire platelet, an evaporated NiCr heater and a carbon slab thermometer. The heat capacity of the empty calorimeter was determined in a separate run. In the SWEX method the sample is weakly thermally linked to a temperature controlled heat sink. The temperature response of the sample to an applied square wave heat pulse is monitored and fit to a simple exponential ( $\exp(-t/\tau)$ ), both in the heating and in the cooling period. The specific heat immediately follows from  $C_p = \tau P / \Delta T - C_a$ , where  $P$  is the supplied heater power and  $\Delta T$  the asymptotic temperature difference between heating and cooling period. A necessary condition is that the internal thermal relaxations of the sample, sample holder, heater and thermometer are much faster than the observed temperature decay. The experimental specific heat of the Au<sub>11</sub> is shown in fig. 5.5a. At each temperature, the obtained values for the specific heat are given for the heating as well as the cooling period. Their difference gives an indication of the error, which increases as the temperature is raised. This can be attributed to an increase of the relaxation times for internal equilibrium and also for the observed thermal decay, from several seconds at the lowest to minutes at the highest temperatures.

The calculated specific heat resulting from the intra-cluster vibrations is represented by the broken line in fig. 5.5a. First the  $3N \times 3N$  matrix elements  $F_{ij}$  in equation 5.3 are calculated using the X-ray data and the force constant at 2.88 Å given in table 5.2. The force constant is scaled to the Au-Au bond length, as dis-

cussed in section 5.6. After solving the eigenvalue problem, as given in equation 5.6, the eigenvalues  $\Omega_k$  are substituted into equation 5.10. The resulting specific heat of the intra-cluster vibrations falls off exponentially if the temperature becomes smaller than the energy of the lowest normal mode (i.e. 27 K). In the high temperature limit the specific heat  $C/R$  amounts to  $3N - 6 = 27$ , which is equal to the number of internal degrees of freedom. Unfortunately, it was impossible to measure the specific heat by the method employed here at temperatures where this contribution becomes relevant. Over the measured temperature range the specific heat is completely determined by the inter-cluster vibrations, represented in fig. 5.5a by the dotted line. This contribution to the specific heat is given by the well-known Debye formula

$$C/R = 9 \left( \frac{T}{\theta_D} \right)^3 \int_0^{\theta_D/T} \frac{x^4 e^x dx}{(e^x - 1)^2}, \quad (5.16)$$

where the three translational degrees of freedom are taken care of in the prefactor. The full curve in fig. 5.5a which represents the sum of inter- and intra-cluster vibrational specific heats, follows the data quite well. The fact that this curve is not fitted to the data, but calculated using the parameters resulting from the M.E.S. measurements, confirms the idea that only inter-cluster vibrations are responsible for the specific heat at these low temperatures. Below about 5 K the specific heat follows the commonly found third power of the temperature. At the highest temperatures, in the Dulong and Petit limit, a specific heat,  $C/R$ , of 3 is calculated. The discrepancy between the data and the calculated curve may be attributed either to the uncertainty of the absolute f-factor determination or to the crudity of our model. At the highest temperatures it is likely that the ligands contribute to the specific heat.

The specific heat of  $\text{Au}_{55}(\text{PPh}_3)_{12}\text{Cl}_6$  has been measured in our laboratory by means of an adiabatic heat pulse technique between 0.5 and 20 K. Additional data between the 2 and 35 K had been measured earlier using the same technique at the Max Planck Institute in Stuttgart by Gmelin, who kindly provided these data. The specific heat between 120 and 300 K was also measured by Gmelin using a scanning calorimeter (Perkin-Elmer dcs-2). These various data are combined and plotted in fig. 5.5b. Taking the Debye temperature  $\theta_D = 15$  K found in the previous section, we have calculated the specific heat resulting from the inter-cluster vibrations using formula 5.16. This contribution is represented in fig. 5.5b by the dotted curve and predicts the data at low temperatures quite well indeed. Well below the Debye temperature ( $T < 3$  K), the specific heat varies with the third power of the temperature, characteristic for phonons in a three-dimensional continuous medium. According to Derrida et al. [17] and Rosenberg [16], a glass, an infinitely percolating cluster, or an amorphous material (as in our case) can be seen as an effective three-dimensional medium as long as the wave lengths of the phonons are larger than a characteristic length. In our materials this length is determined by the cluster size. When one assumes a longitudinal sound velocity of  $1.5 \cdot 10^3$  m/s, the shortest wave length (i.e. at the Debye cutoff) will be of the order of 50 Å, which is a factor of 2.5 larger than the diameter of the cluster with ligands. Above 5 K

the intra-cluster vibrations start to dominate the specific heat, which is calculated in the same way as for the intra-cluster vibrations in Au<sub>11</sub>. The only difference is that the force constant is assumed to be the same for all Au-Au bonds in this close-packed structure. Evidently, the classical limit for  $C/R$  equals  $3N - 6 = 159$ . Up to temperatures of 20 K, the two contributions to the specific heat predict the data very well. The deviations found above 100 K are probably due to the omission of the ligands in our model. Indeed, at these temperatures the measured specific heat is larger than the classical limit of the Au atoms alone. A way to calculate the specific heat contribution of the ligands would be to determine the valence force fields of the ligands from Raman, infrared, and far infrared spectroscopy. This effort has not been undertaken, because of its complexity and since it falls outside the scope of this thesis. From far infrared and infrared frequency correlation charts, however, one can learn that the frequencies, corresponding to the stretch modes and the in-plane, and out-of-plane modes of the phenyl groups, are mainly found in the range  $200 \text{ cm}^{-1}$  ( $\approx 300 \text{ K}$ ) and higher [40]. They will have a negligible effect on the specific heat in the temperature range below 50 K. Some bond bending modes and rotational degrees of freedom, on the other hand, are commonly found at lower energies and may be one of the reasons for the deviations between experimental data and our model.

A comparison of the calculated specific heats of Au<sub>11</sub> and Au<sub>55</sub> leads to the conclusion that the crossover temperature at which the intra- and inter-cluster contributions to the specific heat are equal, is higher for Au<sub>11</sub> than for the Au<sub>55</sub> compound (11 K and 7.5 K respectively). Three arguments can be brought forward to explain this difference. Firstly, the Debye temperature related to the inter-cluster vibrations of Au<sub>11</sub> is higher than for Au<sub>55</sub> (see table 5.2). Secondly, the normal mode with lowest energy of Au<sub>11</sub> exceeds that of Au<sub>55</sub> (27 K and 23 K respectively). Finally, the contribution of the inter-cluster vibrations becomes larger with decreasing cluster size.

It is interesting to notice that this crossover behaviour in our case between inter- and intra-cluster vibrations is comparable to the crossover behaviour between phonon and fracton excitations in percolating networks [16,17]. In these networks at low temperatures (i.e. in the phonon regime), the phonon wave lengths are larger than some characteristic crossover length, that scales with the percolating correlation length, and the percolating network shows a density of states and a specific heat as if it were an effective continuous medium. At higher temperatures the precise structure of the network becomes of importance and the excitations are supposed to be fracton-like.

Whereas in metals the specific heat contribution due to the electrons predominates at the lowest temperatures, it can be neglected in metal cluster compounds. This can be inferred from molecular orbital calculations on Au clusters with a nuclearity of about ten [33], which predict typical energy splittings at the highest occupied molecular orbital of the order of  $1 \cdot 10^3 \text{ K}$ . The energy splittings increase with decreasing particle sizes. The same conclusion would be reached following the arguments of Perenboom et al. [41], who calculated the average level splitting at

the Fermi level for small metal particles. Also for the  $\text{Au}_{55}$  cluster the electronic level splittings should still be large.

## 5.8 Discussion

The experimental inter-cluster Debye temperatures  $\theta_D^{\text{inter}}$ , as given in table 5.2, can be related to earlier work on colloidal gold particles embedded in a gelatine matrix [42]. In that study, temperature dependent Mössbauer spectra were taken on three samples with average particle diameters of 42, 62, and 176 Å. The Mössbauer fractions obtained could be described very well by the product of two f-factors. One f-factor was related to the intra-particle vibrations, using a Debye function with a cutoff temperature equal to that observed in bulk gold ( $\theta_D = 168$  K). The other described the vibrations of the particle as a whole in terms of an Einstein oscillator. To be able to make a comparison to our results, we have translated these Einstein temperatures  $\theta_E$  to Debye temperatures by the relation  $\theta_D = \sqrt{3}\theta_E$ , valid in the high temperature limit appropriate for the inter-cluster vibrations. For the 42, 62, and 176 Å particles, a Debye temperature of 5.4, 3.3, and 1.1 K has been found respectively. In the Debye scheme, a linear dispersion relation is assumed, where the phonon frequency  $\Omega = (F/m)^{1/2}|\mu|$ . The phonon density is taken to be zero above the wave vector  $\mu_D$ , the corresponding  $\Omega_D$ , evidently, varies with  $(F/m)^{1/2}$ . A mass increase results in a decrease in Debye temperature. This is actually observed both for the colloidal gold particles and the gold cluster compounds (see above and table 5.2). However, the Debye temperature does not change with the square root of the inverse mass. This can be attributed to a difference in force constants due to the different environments of the clusters: the colloidal particles were embedded in a gelatine matrix,  $\text{Au}_9$  and  $\text{Au}_{11}$  (which are a charged and an uncharged cluster compound respectively) are both ordered in a regular crystal structure, and  $\text{Au}_{55}$  is a neutral cluster that is stacked amorphously.

In table 5.2 the force constants are given, evaluated at 2.88 Å, with which the intra-cluster vibrations are calculated and fitted to the M.E.S. data. One can compare these to the bulk value. The compressibility of bulk gold yields a force constant of 34 N/m, if one assumes massless springs between nearest neighbours. This force constant has the same order of magnitude as those obtained experimentally. We think these force constants must be seen as empirical parameters and we do not want to draw further quantitative information from them because of the crudity of the model used. The influence of the ligands as well as of all but the nearest neighbour interactions are neglected, identical interactions are assumed to be present between each gold site, bond bending and other than pair interactions as well as the rotational degrees of freedom of the entire clusters are discarded, inter- and intra-cluster vibrations are assumed to be decoupled, and finally, higher than second order perturbations of the inter-atomic potential are excluded.

A recent publication on LEED measurements of the Debye-Waller factor for atoms at a free (100) and a free (111) surface of bulk gold [43] gave Debye temperatures of 82 K and 83 K, respectively. The Mössbauer fractions corresponding

to these Debye temperatures are equal to 0.03 at zero temperature. This is much smaller than any of the surface  $f$ -fractions observed in the gold cluster compounds (see figure 5.4). This indicates that the bonding of the individual gold atoms on free macroscopic surfaces is considerably weaker than that of surface sites of metal cluster compounds. It is important to keep in mind that the decrease of the Debye temperature at macroscopic surfaces is a result of long wave length surface modes [44]. In small clusters there is evidently a lower limit to the wavelength of the intra-cluster vibrations set by the cluster size, decreasing the specific heat even below the bulk value at low temperatures [14]. The inter-cluster vibrations obscure the comparison between bulk surface and surface sites of metal cluster compounds even further. It is, therefore, questionable whether information on the phonon modes at macroscopic surfaces can be obtained from the observation of small clusters.

We have calculated intra-cluster vibrations of bare cuboctahedral clusters with nuclearity 13, 19, 43, 55, 147, 309, and 561 in order to examine how the  $f$ -factors of the individual sites are affected and how the phonon density of states depends on the cluster nuclearity. We chose these cluster sizes since the first three represent cuboctahedra composed of a central atom with up to the first, the second, and the third nearest neighbours respectively. Cuboctahedral clusters with the nuclearities 55, 147, 309, and 561 are composed of a central atom surrounded with 2, 3, 4, and 5 fully occupied shells of atoms respectively. A Pd cluster consisting of 561 Pd atoms is presently being studied in our group. Moreover, since a computational specific heat study on these and some larger cuboctahedral clusters has been reported by Burton [14], we have the possibility to confirm our mathematical treatment as given in section 5.2, and to convince ourselves that the precise form of the interaction has hardly any influence on the vibrational density of states and the specific heat. Using a force constant of 34 N/m, as we estimated for gold metal, between nearest neighbour gold atoms, the eigenvalues and vectors in equation 5.6 are calculated. The vibrational density of states is shown in fig. 5.6 for clusters with nuclearity of 13, 55, and 561. For the smallest cluster the energies of the normal modes are represented by vertical lines. An envelope is drawn in the form of a block diagram. To make a comparison possible, also the bulk phonon density of states taken from ref. [44] is represented. We want to point out that the vibrational density of states of the 561 cluster already resembles rather closely that of the bulk. A specific heat study of  $\text{Pd}_{561}$  is underway to investigate this. The lowest and highest normal mode energies are given in table 5.3. The highest (cutoff) energy remains roughly constant as the cluster size increases, and is comparable to the Debye temperature of bulk gold (i.e. 168 K). The normal mode corresponding to this energy is the one which is most asymmetric (optical, if one can speak about phonons), and thus determined by the inter-atomic distance. On the other hand, the value of the lowest energy mode decreases as the cluster size increases. The distance between two atoms with maximal opposite displacement due to this symmetric normal mode, and thus its energy, is determined by the cluster size.

Using formula 5.12, the  $f$ -factors at zero temperature are calculated and plotted in fig. 5.7 versus the number of nearest neighbours. For the different core sites in



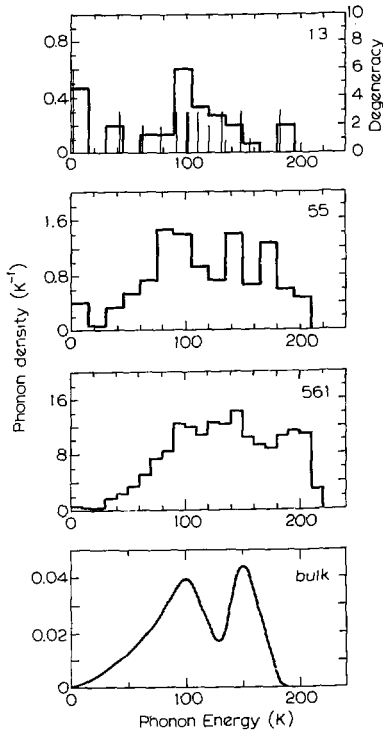


Figure 5.6: Calculated vibrational density of states for bare cuboctahedral clusters with nuclearity 13, 55, and 561 (in  $\text{K}^{-1}$  per cluster) and for a bulk crystal (in  $\text{K}^{-1}$  per atom), the latter is taken from ref. [44].

Table 5.3: The lowest and highest normal mode energy  $\Omega_L$  and  $\Omega_H$  (in K).

Cluster nuclearity	$\Omega_L$	$\Omega_H$
13	183	44
19	183	53
43	201	33
55	197	25
147	210	24
309	215	22
561	216	19

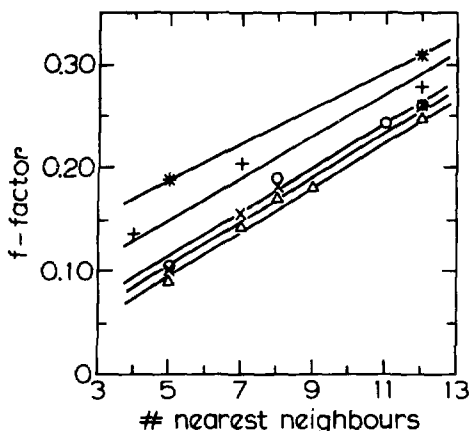


Figure 5.7: The  $f$ -factors at  $T = 0$  K as a function of the number of nearest neighbours, calculated by taking only the intra-cluster vibrations into account. (★) represents Au<sub>15</sub>, (+) Au<sub>19</sub>, (○) Au<sub>43</sub>, (x) Au<sub>55</sub>, and (△) Au<sub>147</sub>. The full lines guide the eye.

the two largest clusters, each of which are coordinated by 12 nearest neighbours, the  $f$ -factors vary less than 3 %. For the sake of clarity their weighted average is plotted. From this figure the correlation between the  $f$ -factors and the number of nearest neighbours is apparent. The fact that in the cluster compounds under investigation different  $f$ -factors at inequivalent sites are found experimentally can thus mainly be attributed to the different number of nearest neighbours that these sites have. Another prominent feature observable in figure 5.7 is the decrease in recoilfree fraction as the cluster size increases. Increasing the cluster size decreases the energy of the lowest normal mode energies (see table 5.3). We believe that these lowest normal modes play a dominant role in decreasing the  $f$ -factors. The  $f$ -factors for the two largest clusters are omitted in fig. 5.7, since they are very similar to those for the 147 atom cluster. (Actually their  $f$ -factors are a few percent smaller.)

Finally we want to spend a few words on the directional anisotropy of the vibrations. The exponent as defined in equation 5.12 is calculated in three orthogonal directions and divided by  $k^2$ , the wave vector of the  $\gamma$ -rays. The resulting mean square vibrational amplitudes and their anisotropies for bare Au<sub>55</sub> clusters can be found in table 5.4. The  $z$  direction is chosen to be radial i.e. normal to the surface. The  $x$  and  $y$  directions are chosen in two perpendicular directions with highest symmetry, in order to find the largest anisotropy for the in-plane vibrations. All surface sites except one show vibrations that are largest in the radial (or normal) direction, as expected in the theoretical literature and also observed experimentally [45]. The interesting point is that this is not the case for the PPh<sub>3</sub> bonded Au sites, which have a larger in-plane mean square vibration. This anomaly may be

Table 5.4: Radial mean square vibrational amplitudes in  $\text{\AA}^2$  and the vibrational anisotropies in % for different sites in the  $\text{Au}_{55}$  cluster compound.

site	$\langle \delta z^2 \rangle$	$\frac{2\langle \delta y^2 \rangle - 1}{\langle \delta x^2 \rangle + \langle \delta y^2 \rangle}$	$\frac{\langle \delta x^2 \rangle - \langle \delta y^2 \rangle}{\langle \delta x^2 \rangle}$
central	0.0126	0	0
1st shell	0.0131	+ 3	3
$\text{PPh}_3$	0.0187	-19	40
Cl	0.0183	+21	0
unb.surf.	0.0183	+ 5	$\sim 0$

related to the precise geometry of the five surrounding atoms. One is coordinated radially, the other four are surrounding this site roughly in a plane forming a rectangle with a separation much larger in the  $y$  than in the  $x$  direction. Although the Mössbauer effect in general is sensitive to anisotropies of vibrations, usually referred to as Goldanskii-Karyagin effect, it is hardly observable in  $^{197}\text{Au}$  M.E.S., since the mixing of  $M_1$  and  $E_2$  radiation accidentally cancels the effect [46]. Recently, larger in-plane mean square vibrational amplitudes have also been found experimentally in a  $\text{Cu}(100)$  surface with chemisorbed Cl using the surface extended X-ray absorption fine structure method [47]. These two examples illustrate that a conventional view can no longer be applied when the microscopic geometry or the electron structure [47] is changed.

## 5.9 Conclusion

To the authors' knowledge, van Wieringen [48] was the first to point out that for understanding the recoilfree fraction in the M.E.S. on small particles the recoil of the entire particle becomes of importance. In a short letter he compared the recoilfree fractions of identical iron oxide particles supported by three matrices which differed in stiffness. The  $f$ -factor decreased with decreasing stiffness of the matrix, for which the particle vibrations are responsible. It is therefore remarkable that in specific heat studies the inter-cluster or inter-particle vibrations have been taken into account in a few cases only [49]. As mentioned above, Vieggers [42] observed a Debye temperature of 1.1 K for the largest colloidal Au particle with a diameter of 176  $\text{\AA}$ . Roughly estimated, this temperature corresponds to the crossover temperature below which the specific heat will be determined by the inter-cluster vibrations. Neither the present specific heat data nor the M.E.S. results can be understood without considering the inter-cluster vibrations, which are of dominant importance for the specific heat at temperatures below  $\sim 10$  K. They also determine the overall intensity of the M.E.S. spectra in the measurable temperature range (up to  $\sim 30$  K). In a study of a large number of molecular gold compounds, Vieggers [50] has found a strong correlation between the square root of the mass and the logarithm of the  $f$ -factor at 4.2 K. This indicates that the inter-molecular vibrations are of importance for the low temperature specific heat of molecular compounds.

By contrast, in the literature one finds a variety of studies devoted to the intra-cluster vibrations. We want to mention a few of these, and briefly explain why they have been not considered here. The Debye model with or without including various kinds of corrections can be used to describe the temperature dependence of the f-factors. None of these models predict different f-factors for inequivalent Au sites as observed in the present M.E.S. experiments, and therefore are irrelevant for metal cluster compounds. A more realistic approach is a description in terms of the fraction  $(1 - \alpha)$  of surface atoms and the fraction  $(\alpha)$  of inner-core atoms, each characterized by a Debye function [51]. The fact that LEED measurements as discussed above show a surface Debye temperature unequal to the bulk value makes this idea even more appealing. It has, however, still the disadvantage of not predicting different f-factors for the different surface sites, as is most clearly the case in our Au<sub>55</sub> M.E.S. data. Recently, a large number of studies have been concerned with vibrational modes in isotropic spheres [52,53]. This model will be compared to the specific heat measurements in a future paper by our group. Evidently, again severe problems will arise when one wants to compare this model to the present M.E.S. data, since on the grounds of symmetry the vibrations will be identical over the whole surface.

In conclusion, we stipulate that the intra-cluster vibrations of metal cluster compounds up to at least 55 atoms cannot be described by models starting from a macroscopic view point. On the other hand, the microscopic approach as introduced in section 5.2 is not only capable of explaining the intra-cluster vibrations as observed by a microscopic technique (M.E.S.), but also predicts the results obtained by a macroscopic technique (specific heat) very well indeed up to relatively high temperatures.

## References

- [1] D. Fenske, J. Ohmer, and J. Hachgenei, *Angew. Chem. Int. Ed. Engl.* 24 (1985) 993.
- [2] P. Chini, *Gass. Chim. Ital.* 109 (1979) 225.
- [3] J.J. Steggerda, J.J. Bour, and J.W.A. van der Velden, *Rec. J. Royal. Neth. Chem. Soc.* 101 (1982) 164.
- [4] M.D. Vargas and J.N. Nicholls, *Adv. Inorg. Chem. and Radiochem.*, 30 (1986) 123.
- [5] G. Schmid, R. Pfeil, R. Boese, F. Bander-  
mann, S. Meyer, G.H.M. Calis, and J.W.A.  
van der Velden, *Chem. Ber.* 114 (1981)  
3634.
- [6] G. Schmid and W. Huster, *Z. Naturforsch.*  
41b (1986) 1028.
- [7] M.N. Vargaftic, V.P. Zagorodnikov, I.P.  
Stolyarov, I.I. Moiseev, V.A. Likhobobov,  
D.I. Kochubey, A.L. Chuvilin, V.I.  
Zaikovsky, K.I. Zamaraev, and G.I. Timo-  
feeva, *J.C.S. Chem. Comm.*, (1985) 937.
- [8] W.P. Halperin, *Rev. Mod. Phys.* 58 (1986)  
533.
- [9] B.J. Pronk, H.B. Brom, L.J. de Jongh, G.  
Longoni, and A. Ceriotti, *Sol. St. Commun.*  
59 (1986) 349.
- [10] B.J. Pronk, H.B. Brom, A. Ceriotti, and  
G. Longoni : *Sol. St. Commun.* accepted  
for publication.
- [11] M.P.J. van Staveren, H.B. Brom, L.J. de  
Jongh and G. Schmid: *Sol. St. Commun.*  
60 (1986) 319.
- [12] H.H.A. Smit, R.C. Thiel, L.J. de Jongh, N.  
Klein, and G. Schmid, *Sol. St. Commun.* 65  
(1988) 915.
- [13] E.B. Wilson, J.C. Decius, P.C. Cross,  
"Molecular Vibrations", McGraw-Hill  
Book Company Inc., New York (1955).
- [14] J.J. Burton, *J. Chem. Phys.* 52 (1970) 345.
- [15] C. Kittel, "Introduction to Solid State  
Physics", 5th ed., J. Wiley and Sons, New  
York, 1976.
- [16] H.M. Rosenberg, *Phys. Rev. Lett.* 54  
(1985) 704.
- [17] B. Derrida, R. Orbach, and Kin-Wah Yu,  
*Phys. Rev.* B29 (1984) 6645.
- [18] F. Cariati and L. Naldini, *J.C.S. Dalton  
Trans.* (1972) 2286.
- [19] P.L. Bellon, F. Cariati, M. Manassero, L.  
Naldini, and M. Sansoni *J.C.S., Chem.  
Commun.* (1971) 1423.
- [20] F. Cariati and L. Naldini, *Inorg. Chim.  
Acta* 5 (1971) 172.
- [21] M. McPartin, R. Mason, and L. Malatesta,  
*J.C.S., Chem. Commun.* (1969) 334.
- [22] P.L. Bellon, M. Manassero, and M. Sansoni  
*J.C.S., Dalton Trans.* (1972) 1481.
- [23] L.R. Wallenberg, J.O. Bovin and G.  
Schmid, *Surface Science* 156 (1985) 256.
- [24] F.A. Vollenbroek, J.W.A. van der Velden,  
J.J. Bour, and J.M. Trooster, *Recl. J. Royal  
Neth. Chem. Soc.* 100 (1981) 375.
- [25] F.A. Vollenbroek, P.C.P. Bouten, J.M.  
Trooster, J.P. van den Berg, and J.J. Bour,  
*Inorg. Chem.* 17 (1978) 1345.
- [26] H.D. Bartunik, W. Potsel, R.L. Mössbauer,  
and G. Kaindl, *Z. Physik* 240 (1970) 1.
- [27] F.A. Vollenbroek, J.J. Bour, J.M. Trooster,  
J.W.A. van der Velden, *J.C.S., Chem.  
Comm.* (1978) 907.
- [28] G.K. Shenoy and F.E. Wagner, "Mössbauer  
Isomer Shifts", North-Holland, Amsterdam  
(1978).
- [29] L. Pauling, "The Nature of the Chemical  
Bond", 3rd ed. (Cornell Univ. Press, New  
York, 1963)
- [30] W. Bos, R.P.F. Kanters, C.J. van Halen,  
W.P. Bosman, H. Behm, J.M.M. Smits,  
P.T. Beurskens, J.J. Bour, *J. Organometal-  
lic Chem.* 307 (1986) 385.
- [31] H. Prosser, G. Wortmann, K. Syassen, and  
W.B. Holsapfel, *Z. Physik* B24, (1976) 7.

- [32] J.W.A. van der Velden, PhD. Thesis, Katholieke Universiteit te Nijmegen (1983).
- [33] D.M.P. Mingos, J.C.S., Dalton Trans. (1976) 1163.
- [34] H. Siebert, "Anwendung der Schwingungsspektroskopie in der Anorganische Chemie", Springer-Verlag, Berlin (1966).
- [35] G. Kaindl, K. Leary, and N. Barlett, J. Chem. Phys. 59 (1973), 5050.
- [36] S.L. Rudas, J.P. Ansermet, Po-Kang Wang, and C.P. Slichter, Phys. Rev. Lett. 54 (1985) 71.
- [37] R.V. Parish, Proc. ICAME Melbourne (1987), to be published in Hyperf. Inter.
- [38] P.Gans, "Vibrating molecules", Chapman and Hall Ltd, London (1971).
- [39] M. Regelsberger, R. Wernhardt, M. Rosenberg, J. Phys. E, Sci. Instrum. 19 (1986) 525.
- [40] N.N. Greenwood and E.J.F. Ross, "Index of Vibrational Spectra of Organic and Inorganic Metallic Compounds", Butterworth 1975, London.
- [41] J.A.A.J. Perenboom, P. Wyder, and F. Meyer, Physics Reports 78 (1981) 173.
- [42] M.P.A. Vieggers and J.M. Trooster, Phys. Rev. B15 (1977) 72.
- [43] M. Kostelits and J.L. Domange, Sol. St. Commun. 13 (1973) 241.
- [44] J.M. Dickey and A. Paskin, Phys. Rev. Lett. 21 (1968) 1441.
- [45] P. Roubin, D. Chandesris, G. Rossi, J. Lecante, M.C. Desjonquères, and G. Tréglià, Phys. Rev. Lett. 56, 1272 (1986).
- [46] H. Prosser, F.E. Wagner, G. Wortmann, G.M. Kalvius, and R. Wäppling, Hyperf. Inter. 1 (1975) 25.
- [47] F. Sette, C.T. Chen, J.E. Rowe, and P.H. Citrin, Phys. Rev. Lett. 59 (1987) 311.
- [48] J.S. van Wieringen, Phys. Lett. 26A (1968) 370.
- [49] E. Gmelin, A. Simon, W. Brämer, and R. Villar, J. Phys. Soc. 76 (1982) 6256.
- [50] M.P.A. Vieggers, PhD. Thesis (1976) Katholieke Universiteit te Nijmegen.
- [51] S. Akselrod, M. Pasternak, and S. Bukshpan, Phys. Rev. B11 (1975) 1040.
- [52] N. Nishiguchi and T. Sakuma, Sol. St. Comm. 38 (1981) 1073.
- [53] A. Tamura, K. Higeta, and T. Ichinokawa, J. Phys. C Sol. St. Phys. 15 (1982) 4975.

## Samenvatting

### Mössbauer Studies van Niet-lineaire Excitatie en Goudclusterverbindingen

In het voor u liggende proefschrift wordt het Mössbauer effect toegepast bij het onderzoek naar een tweetal actuele onderwerpen uit de vaste stof fysica. Het Mössbauer effect is een experimentele techniek, gebaseerd op verliesvrije emissie en absorptie van  $\gamma$ -straling. Deze komt vrij bij het verval van de kernen van een radioactief element. We spreken van verliesvrije emissie en absorptie, als de  $\gamma$ -straling precies de energie heeft, die hoort bij het verval van de kern, en dus geen energie verloren is gegaan aan bijvoorbeeld de omgeving van de kern. Als het verval verliesvrij gebeurt, is de energie van de  $\gamma$ -straling in principe zeer nauwkeurig te meten. Om dat mogelijk te maken wordt het experiment als volgt uitgevoerd. Een radioactieve bron wordt met een bepaald snelheidspatroon als functie van de tijd bewogen. De energie van de  $\gamma$ -straling wordt diensgevolge gemoduleerd. Het voor deze energie modulatie verantwoordelijke principe wordt het Doppler effect genoemd. De absorber, die het object van het onderzoek is, wordt blootgesteld aan de  $\gamma$ -straling, die vervolgens in een daarachter opgestelde detector wordt geregistreerd. Het resultaat (vaak pas na ongeveer 24 uur verkregen), bestaat uit een gemeten absorptie als functie van de energie van de  $\gamma$ -straling. Dit wordt het Mössbauer spectrum genoemd. De energie van de  $\gamma$ -straling wordt gewoonlijk uitgedrukt in snelheidseenheden, die corresponderen met de snelheid waarmee de bron beweegt.

De energie, die de absorber verliesvrij opneemt, wordt beïnvloed door de interactie tussen de kern en zijn omgeving, waartoe zowel de electronen van het atoom waarvan de kern een deel uitmaakt, als ook de naburige atomen gerekend moeten worden. We kunnen drie verschillende typen van deze zogenaamde hyperfijninteractie onderscheiden.

- i) De isomere verschuiving, die een zeer gevoelige maat is voor de electronen dichtheid ter plaatse van de kern. Deze resulteert in een verschuiving van de absorptielijnen in het Mössbauer spectrum.
- ii) Het hyperfijnveld, ofwel het magnetische veld ter plaatse van de kern.
- iii) De quadrupoolsplitsing, die een maat is voor de locale variatie van het elektrisch veld ter plaatse van de kern.

De absorber kan, ten gevolge van de laatste twee Mössbauer parameters, verschillende energieën verliesvrij opnemen. De parameters kunnen met behulp van de computer uit het spectrum bepaald worden. Met deze drie grootheden is het Mössbauer effect een machtig hulpmiddel, dat een schat aan informatie kan verschaffen over de lokale omgeving van de Mössbauer kern. Zij wordt dan ook veelvuldig met succes toegepast bij het onderzoek naar chemische en fysische problemen.

In dit proefschrift hebben we het Mössbauer effect toegepast op twee onderwerpen uit de vaste stof fysica, die de laatste jaren sterk in de belangstelling staan.

Het eerste heeft te maken met een vrij nieuwe tak van de fysica, de niet-lineaire

fysica, die pas gedurende de laatste twee decennia beoefend wordt. (We zullen verderop terug komen op deze benaming.) Gedurende deze periode heeft de niet-lineaire fysica bewezen vele verschijnselen te kunnen verhelderen op het gebied van de natuurkunde, maar ook op dat van andere disciplines zoals bijvoorbeeld de biologie en meteorologie. Het is voorts gebleken dat het magnetisme een fysisch verschijnsel is, met behulp waarvan we de nieuwe theorieën, die binnen de niet-lineaire fysica zijn ontwikkeld, zeer goed kunnen toetsen aan de praktijk van het experiment. De magnetische systemen die wij gebruiken voor onze studie zijn niet-geleidende verbindingen die opgebouwd zijn uit ketens van ijzer-atomen, welke laatste de dragers zijn van de magnetische momenten. De magnetische wisselwerking tussen de magnetische momenten in de keten (aangeduid met  $J$ ) is vele malen groter dan die tussen de momenten gesitueerd op verschillende ketens. Een anti-ferromagnetische keten is in de laagst-energetische toestand, de grondtoestand, als alle momenten tegengesteld gericht zijn aan hun burens. Dit is in principe het geval als de temperatuur het absolute nulpunt nadert. Bij eindige temperaturen wordt deze grondtoestand verstoord door thermische bewegingen. Deze verstoringen, die een bepaalde wanorde in het systeem veroorzaken, worden excitaties genoemd. In vroegere theorieën werd verondersteld dat deze verstoringen de relatieve oriëntatie van de momenten slechts weinig veranderden. Daar de wiskundige beschrijving van deze verstoringen is gebaseerd op een bepaalde klasse vergelijkingen, de lineaire differentiaal vergelijkingen, heeft de oorspronkelijke fysica de naam lineaire fysica gekregen.

In een bepaalde klasse van ketensystemen echter konden de waargenomen fysische verschijnselen niet worden verklaard met behulp van de lineaire fysica. Deze ketensystemen worden gekarakteriseerd door een magnetische anisotropie, die de magnetische momenten dwingt parallel aan een bepaalde voorkeurs-as te staan, zodat ze slechts de vrijheid hebben om in twee richtingen hierlangs te staan, zeg op of neer. Het regelmatige patroon van de tegengesteld gerichte, naburige momenten kan nu echter onderbroken worden door twee gelijk gerichte burens. Deze niet-lineaire excitaties zijn wanden die twee domeinen scheiden die zich in de grondtoestand bevinden. Zij zijn oplossingen van niet-lineaire differentiaal vergelijkingen, waaraan zij hun naam ontleenen. De energie die met zo'n niet-lineaire excitatie of kink gemeend is, komt overeen met de hierboven genoemde magnetische wisselwerking,  $J$ .

De interessante eigenschap van een kink of van een vergelijkbare excitatie, het soliton, is dat zijn energie onafhankelijk is van de plaats op de keten. De snelheid die meegegeven wordt bij de creatie zal daarom behouden blijven tijdens de voortbeweging. Bovendien is er de theoretische voorspelling voor solitonen dat zij hun initiële snelheid zelfs niet verliezen als ze op elkaar botsen. Verder worden zij niet verstoord door onzuiverheden of onregelmatigheden in de opbouw van de ketens. Deze theorie staat als de ideale gas benadering bekend. De experimenten, beschreven in dit proefschrift, hebben mede als doel de toepasbaarheid van deze theorie op de praktijk te toetsen. Op grond van deze ideale gas benadering zou namelijk het aantal keren dat een magnetisch moment per tijdseenheid naar de



tegengestelde richting omklapt gelijk zijn aan het produkt van de snelheid en de dichtheid van de kinks.

Het magnetisch moment van het ijzer-atoom bepaalt het magnetisch hyperfijnveld ter plaatse van de kern. Dientengevolge verandert, met het magnetisch moment, ook het hyperfijnveld van richting. Dit heeft z'n invloed op het Mössbauer spectrum, zodat hieruit informatie over de voortbeweging van de kinks is te destilleren. Het Mössbauer effect is gevoelig voor de veranderingen van de richting van het hyperfijnveld, mits de frequentie van deze veranderingen tussen de  $10^5$  en  $10^9$  keren per seconde plaatsvinden. Het is dan ook een welkome aanvulling op de neutronenverstrooiingsexperimenten, die ook zijn toegepast om de ideale gas benadering te toetsen, maar die slechts gevoelig zijn voor veel hogere frequenties (vanaf  $10^{10}$  Hz). Dit betekent dat een ander type fluctuaties zal worden waargenomen.

Ruim vijf jaar geleden startte onze groep een onderzoek naar niet-lineaire excitaties, waarvan het onderhavige werk een onderdeel is. De resultaten van het Mössbauer experiment en de ideale gas benadering vertonen grote discrepanties. Ten eerste is de energie die met de creatie van de excitaties gemoeid is, tweemaal zo hoog als de hierboven genoemde magnetische nabuurinteractie,  $J$ . Ten tweede kan er uit het Mössbauer spectrum opgemaakt worden dat er één gedeelte van de momenten met een lage frequentie en het resterende gedeelte van de momenten met een hoge frequentie fluctueert. Ten derde zijn de waargenomen lage fluctuatiefrequenties vele malen (om en nabij de 100 keer!) lager dan voorspeld door de ideale gas benadering.

Voor de interpretatie van de resultaten is een fenomenologisch model voorgesteld. Hierin is de beweging van de niet-lineaire excitaties beperkt tot een klein segment van de keten (gedurende de zeer korte meettijd,  $\sim 10^{-7}$  seconde). De kinks bewegen met hoge snelheid heen en weer, zodat de momenten die hierdoor beïnvloed worden een hoge fluctuatiefrequentie vertonen. Naast dit snelle fluctuatiemechanisme toont het Mössbauer effect aan dat er nog een geheel ander mechanisme werkzaam is, dat niet voorspeld wordt in de ideale gas benadering. Dit betreft de thermische creatie van niet-lineaire excitaties in paren. Het fenomenologische model is consistent met de resultaten van andere experimentele technieken.

Het tweede fysische probleem, onderzocht in dit proefschrift, heeft te maken met de atomen in de metaalkernen van goudclusterverbindingen. Metaalclusterverbindingen zijn vaste stoffen samengesteld uit grote, in sommige gevallen zeer grote moleculen die bestaan uit kernen omringd door een schil van liganden. De liganden zijn niet-metaal atomen of moleculen die chemisch gebonden zijn aan het oppervlak van de metaalkern. Zij stabiliseren de metaalkern en verhinderen dat deze aaneengroeien tot grotere metaaldeeltjes.

Onlangs hebben chemici grote vorderingen gemaakt in het synthetiseren van metaalclusterverbindingen met een groot aantal atomen in de metaalkern. Onze groep is enkele jaren geleden begonnen met een onderzoek naar de fysische eigenschappen van deze materialen. Deze systemen maken het mogelijk om oppervlakte effecten te bestuderen, daar een groot gedeelte van de metaal-atomen zich aan het oppervlak van de metaalkern bevindt. Ook theorieën die te maken hebben met

het gegeven dat het aantal atomen per cluster eindig (en klein) is, kunnen met behulp van deze nieuwe materialen getoetst worden. Men kan ruwweg stellen dat deze verbindingen eigenschappen hebben die noch met die van moleculaire verbindingen, noch met die van metaalen te vergelijken zijn.

In dit proefschrift worden experimenten beschreven aan goudclusterverbindingen met metaalkernen van 9, 11 en zelfs 55 goud-atomen. Het Mössbauer effect biedt de unieke gelegenheid om de atomen, die verschillende posities innemen in de metaalkern, afzonderlijk te bestuderen. Dit is mogelijk daar de atomen op de verschillende posities hun eigen karakteristieke Mössbauer parameters hebben, en daardoor in de vorm van verschillende subspectra kunnen worden waargenomen.

Een van de opmerkelijke resultaten is dat, in tegenstelling tot de twee kleine goudclusterverbindingen, de verbinding met 55 goud-atomen in de metaalkern Mössbauer parameters heeft, die al nagenoeg gelijk zijn aan die van goudmetaal, althans voor wat betreft de 13 goud-atomen die in het binnenste van de metaalkern zijn gelegen. De sterkte van de absorptie in een Mössbauer spectrum kunnen we relateren aan de sterkte waarmee de Mössbauer atomen gebonden zijn aan hun omgeving. In de goudclusterverbindingen geeft dit de mogelijkheid om de sterkte van deze bindingen lokaal te bestuderen. Hieruit hebben we kunnen concluderen dat ten eerste deze bindingen afhankelijk zijn van de positie die het atoom inneemt in de metaalkern. In het bijzonder blijkt hierbij het aantal goudnaburen van belang. Ten tweede is de binding van het cluster als geheel een bepalende factor. We hebben de sterkte van de absorpties van de verschillende subspectra, en in het bijzonder hun relatieve sterkte, met succes kunnen verklaren met een simpel wiskundig model, waarbij alle mogelijke trillingen in een metaalcluster zijn berekend. Bovendien zijn voor clusters van 9 tot 561 metaal-atomen alle mogelijke trillingen berekend. Een onderlinge vergelijking heeft tot interessante conclusies geleid.

## Curriculum Vitae

Na in 1978 het gymnasium  $\beta$  aan het St. Adelbert College te Wassenaar afgerond te hebben, ben ik natuurkunde gaan studeren aan de Rijksuniversiteit te Leiden. Het kandidaatsexamen wis- en natuurwetenschappen met bijvak scheikunde werd afgelegd in 1981. Tijdens mijn experimentele stage in de werkgroep van Prof. Dr. W.J. Huiskamp raakte ik geïnteresseerd in de vaste stof fysica, in het bijzonder in niet-lineaire excitaties in laag-dimensionale magnetische systemen. Dankbaar heb ik gebruik gemaakt van de mogelijkheid om tijdens het laatste jaar van mijn studie specialistische Mössbauer metingen te doen aan de University of Liverpool, onder leiding van Prof. Dr. C.E. Johnson. Mijn doctoraalstudie in de experimentele natuurkunde met de bijvakken energie en didactiek heb ik in 1984 voltooid.

Vervolgens werd ik aangesteld als wetenschappelijk medewerker door de Stichting Fundamenteel Onderzoek der Materie (FOM). In nauwe samenwerking met Dr. R.C. Thiel en onder leiding van Prof. Dr. L.J. de Jongh heb ik tijdens de afgelopen vier jaar dankbaar van de mij geboden gelegenheid gebruik gemaakt verschillende onderwerpen uit de vaste stof fysica met behulp van het Mössbauer effect te bestuderen. Een in dit proefschrift opgenomen lijst van publicaties mag hiervan getuige zijn. Twee onderwerpen, die van niet-lineaire excitaties in anisotrope antiferromagnetische ketensystemen en van metaalkernatomen in goudclusterverbindingen, werden geselecteerd voor en vormen het hoofdbestanddeel van het voor u liggende proefschrift. Voorts heb ik met plezier meegewerkt aan het ontwerpen en construeren van een cryogene  $^3\text{He}$  circulatie opstelling voor Mössbauermetingen in het temperatuursgebied tot 0.3 K.

## Published Work

1. H.J.M. de Groot, W.J. Huiskamp, L.J. de Jongh, H.H.A. Smit, R.C. Thiel, and J. Reedijk: "The study of non-linear excitations in quasi 1-d magnetic systems by means of Mössbauer linewidths." In: Trends in Mössbauer Spectroscopy, eds. P. Gütlich, and G.M. Kalvius, University Press Mainz (1983).
2. H.H.A. Smit, H.J.M. de Groot, R.C. Thiel, L.J. de Jongh, C.E. Johnson, and M.F. Thomas: "Field-dependent Mössbauer relaxation study of domain walls in the quasi 1-d antiferromagnet  $\text{RbFeCl}_3 \cdot 2\text{H}_2\text{O}$ ." Sol. St. Commun. 53 (1985) 573.
3. H.J.M. de Groot, L.J. de Jongh, M. ElMassalami, R.C. Thiel, and H.H.A. Smit: "Mössbauer relaxation studies of non-linear dynamical excitations in low-dimensional magnets." Hyperfine Interactions 27 (1986) 93.
4. D.G. Rancourt, H.H.A. Smit, and R.C. Thiel: "Metastable compositionally and magnetically modulated state of Fe-Ni invar and the associated super-moment dynamics from Mössbauer spectroscopy." JMMM 66 (1987) 121-152.
5. H.H.A. Smit, R.C. Thiel, and K.H.J. Buschow: " $^{155}\text{Gd}$  Mössbauer effect in  $\text{Gd}_2\text{Co}_{14}\text{B}$ ." Physica 145B (1987) 329-334.
6. K.H.J. Buschow, H.H.A. Smit, and R.C. Thiel: "Crystal field and magnetic anisotropy in ternary R-3d-B compounds." paper S1-4, 5<sup>th</sup> International Symposium on Anisotropy and Coercivity in Rare Earth Transition Metal Alloys, Bad Soden (F.R.G.), Sept. 1987; Proceedings Deutsche Physikalische Gesellschaft e.v., D-5340, Bad Honnef 1, F.R.G.
7. H.H.A. Smit, M.W. Dirken, R.C. Thiel, and L.J. de Jongh: " $^{155}\text{Gd}$  Mössbauer measurements on the ceramic superconductor  $\text{GdBa}_2\text{Cu}_3\text{O}_7$ ." Sol. St. Commun. 64 (1987) 695.
8. H.H.A. Smit, R.C. Thiel, L.J. de Jongh, G. Schmid, and N. Klein: "Physical properties of metal cluster compounds IV: The thermal motion of  $\text{Au}_{55}(\text{PPh}_3)_{12}\text{Cl}_6$  as probed by  $^{197}\text{Au}$  Mössbauer spectroscopy". Sol. St. Commun. 65 (1987) 915.
9. M. ElMassalami, H.H.A. Smit, H.J.M. de Groot, R.C. Thiel, and L.J. de Jongh: "Relaxation phenomena in non-linear systems; a Mössbauer effect spectroscopy and susceptibility study." In: Magnetic Excitations and Fluctuations II, eds. U. Balucani, S.W. Lovesey, M.G. Rasetti, and V. Tognetti, Springer-Verlag 178-185 (1987).
10. H.H.A. Smit, R.C. Thiel, and K.H.J. Buschow: "On the crystal field induced magnetic anisotropy in B substituted  $\text{RCo}_5$  compounds." J. Phys. F. Met. Phys. 18 (1988) 295.
11. M.W. Dirken, R.C. Thiel, H.H.A. Smit, and H.W. Zandbergen: "Some doubts about Fe substitution in  $\text{REBa}_2\text{Cu}_3\text{O}_{7-\delta}$ ." Submitted to Physica C.
12. H.H.A. Smit, P.R. Nugteren, R.C. Thiel, and L.J. de Jongh: "Mössbauer and specific heat studies of the vibrations of metal core atoms in polynuclear gold cluster compounds." Submitted to Physica B.

## Nawoord

Op deze plaats wil ik allen noemen zonder wie dit proefschrift niet tot stand zou zijn gekomen.

Allereerst de leden en ex-leden van de Mössbauergroep, met wie ik terug kan kijken op een aangename samenwerking en een plezierige, soms intensieve, wetenschappelijke interactie. Huub de Groot heeft als een van de eersten mij de mysteries van de Mössbauer techniek bijgebracht, en heeft samen met Mohammed ElMasalami een wezenlijke bijdrage geleverd aan de resultaten besproken in hoofdstuk 4 van dit proefschrift. Mark Dirken, Tycho Haemers en Michel Traa hebben mij bijgestaan tijdens hun experimentele stage als student. De werksfeer in de werkgroep "Vaste Stof Fysica en Materialen" werd door mij als plezierig ervaren. In het bijzonder wil ik Paul Robert Nugteren en Jaap Baak noemen, die zorg gedragen hebben voor de soortelijke warmte metingen, beschreven in hoofdstuk 5.

I would like to acknowledge the stimulating discussions and fruitful collaborations with many groups and scientists, in particular with Dr. R.H. Nussbaum (Portland State University, U.S.A.), Dr. D.H. Jones (University of Liverpool, England), and Prof. Dr. D.G. Rancourt (University of Ottawa, Canada). The samples used for the present investigations were supplied by Dr. J.J. Bour (Universiteit te Nijmegen), Prof. Dr. G. Schmid (Universität Essen, West-Germany), Prof. Dr. Ir. W.J.M. de Jonge (Technische Universiteit te Eindhoven) and by members of the Leiden Materials Science Centre (Werkgroep Fundamenteel Materialen Onderzoek).

De technische ondersteuning was onontbeerlijk voor het realiseren van de experimenten. In het bijzonder wil ik noemen Kees van der Waals, dhr. J. Hemerik, en Casper Smit, die mijn onmogelijke ontwerpen wisten te realiseren, en de electronici Rob Hulstman en Fred Kranenburg. De heren R.J. van Kuyk, J.D. Sprong voorzagen mij van de benodigde hoeveelheden vloeibaar helium. De computer apparatuur, essentieel voor de analyse van de verrichte metingen, viel onder de verantwoordelijkheid van de heren P.L. Blangé en D. van der Moot. De tekeningen waren verzorgd door Peter Benschop en dhr. W.F. Tegelaar. Bij de verwerking van de tekst werd ik bijgestaan door Barry Cats en Ellie van Rijsewijk, die zich in korte tijd een computer programma eigen maakten dat, naar men zegt, alleen door mensen met een i.q. boven de 150 gebruikt kan worden.

Mijn ouders ben ik zeer erkentelijk voor hun stimulerende interesse in mijn werk, hoewel ik de essentie daarvan slechts op zeer gebrekkige wijze kon overbrengen. Annet, ik heb jouw geduld en steun in het bijzonder in de laatste fase van mijn promotietijd zeer op prijs gesteld.

# **Stellingen**

behorende bij het proefschrift van

**H.H.A. Smit**

1. Het is in het algemeen onmogelijk om uit een analyse van een Mössbauer spectrum in termen van verbrede Lorentzianen, quantitative gegevens te bepalen betreffende het relaxatiemechanisme dat de verbreding veroorzaakt.
2. Voor de interpretatie van de dynamica van domeinwanden in Ising-achtige magnetische systemen zou een theoretische berekening van het Mössbauer spectrum, gebaseerd op een "random-walk" beweging van deze wanden, gewenst zijn.
3. Indien het mechanisme van de supergeleiding in het onlangs gevonden drie-dimensionale perovskiet rooster  $Ba_{1-x}K_xBiO_3$  hetzelfde is als in de hoge- $T_c$  koper-oxiden, dan zijn hierdoor de theoretische verklaringen gebaseerd op één- of twee-dimensionale modellen niet meer van toepassing.

L.F. Mattheiss, E.M. Gyorgy en D.W. Johnson Jr., Phys. Rev. B37 (1988) 3745.

4. Bij de in de praktijk gedefinieerde kritische stroomdichtheid van een type-II supergeleider is slechts een minimale fractie van het fluxdradenrooster ontankerd.

D. Dew-Hughes, Phil. Mag. B55 (1987) 459.

5. De onlangs gevonden verfijning van de kristalstructuur van  $TmNi_2$ , maakt een consistente interpretatie mogelijk van de Mössbauer- en soortelijke warmte-metingen in termen van kristalveldniveaus, waarbij de niet-kubische puntsymmetrie van de zeldzame-aardplaatsen een essentiële rol speelt.

P.C.M. Gubbens, A.M. van der Kraan en K.H.J. Buschow, J. Phys. F: Met. Phys. 14 (1984) 2195 & A.F. Deutz, H.B. Brom, H. Beelen, L.J. de Jongh, W.J. Huiskamp en K.H.J. Buschow, Sol. St. Commun. 60 (1986) 917.

6. De uitspraak van Felner over het verschil in de vrije electron concentratie in de verbindingen  $GdFe_2Si_2$  en  $GdAu_2Si_2$  is in tegenspraak met de resultaten van  $^{155}Gd$  Mössbauer experimenten.

I. Felner, J. Phys. Chem. Solids 36 (1975) 1063.

7. Het is tegenstrijdig dat de Heren XVII de Zeeuwse koopman Pieter Macaré, die van 1702 tot 1711 het ambt van independent-fiscaal op Ceylon vervulde, geen enkele steun verleenden bij de plichtsgetrouwe uitoefening van zijn functie.

8. De genetische variatie in de concentratie van alkaloiden in *Senecio jacobaea* Linnaeus wordt verklaard door de aanwezigheid van een aantal luizensoorten (o.a. *Brachycaudus cardi* L.) en de mieren die van deze luizen profiteren (o.a. *Lasius alienis* Först).
9. De handel in futures en opties met als onderliggende waarde een indexcijfer samengesteld uit een aantal beursfondsen, heeft een destabiliserende invloed op de effectenbeurzen.
10. In een groot aantal toonaangevende studies over het ontstaan van de abstracte beeldende kunst in de twintigste eeuw is het belang van de muziek als voorbeeld voor deze kunst onderschat.
11. Een boekje of floppy met spelling- en grammatica-adviezen zou tot de vaste inventaris moeten behoren van iedere kantoorruimte waar een typemachine of tekstverwerker staat.
12. Het veelgehoorde argument dat wordt aangevoerd om onderzoek in dienst van de defensie te rechtvaardigen door te wijzen op vreedzame toepassingen van de hiermee verkregen technologische vernieuwingen is op zijn minst aanvechtbaar.

Leiden, juni 1988.